

AD

Award Number: DAMD17-01-1-0330

TITLE: Image-Guided Surgery of Primary Breast Cancer Using
Ultrasound Phased Arrays

PRINCIPAL INVESTIGATOR: Emad S. Ebbini, Ph.D.

CONTRACTING ORGANIZATION: University of Minnesota
Minneapolis, MN 55455-2070

REPORT DATE: July 2005

TYPE OF REPORT: Final

PREPARED FOR: U.S. Army Medical Research and Materiel Command
Fort Detrick, Maryland 21702-5012

DISTRIBUTION STATEMENT: Approved for public release;
distribution unlimited

The views, opinions and/or findings contained in this report are
those of the author(s) and should not be construed as an official
Department of the Army position, policy or decision unless so
designated by other documentation.

20060503293

REPORT DOCUMENTATION PAGE

*Form Approved
OMB No. 0704-0188*

Public reporting burden for this collection of information is estimated to average 1 hour per response, including the time for reviewing instructions, searching existing data sources, gathering and maintaining the data needed, and completing and reviewing this collection of information. Send comments regarding this burden estimate or any other aspect of this collection of information, including suggestions for reducing this burden to Department of Defense, Washington Headquarters Services, Directorate for Information Operations and Reports (0704-0188), 1215 Jefferson Davis Highway, Suite 1204, Arlington, VA 22202-4302. Respondents should be aware that notwithstanding any other provision of law, no person shall be subject to any penalty for failing to comply with a collection of information if it does not display a currently valid OMB control number. PLEASE DO NOT RETURN YOUR FORM TO THE ABOVE ADDRESS.

1. REPORT DATE 01-07-2005		2. REPORT TYPE Final		3. DATES COVERED 1 Jul 2001 – 30 Jun 2005
4. TITLE AND SUBTITLE Image-Guided Surgery of Primary Breast Cancer Using Ultrasound Phased Arrays				5a. CONTRACT NUMBER
				5b. GRANT NUMBER DAMD17-01-1-0330
6. AUTHOR(S) Emad S. Ebbini, Ph.D.				5c. PROGRAM ELEMENT NUMBER
				5d. PROJECT NUMBER
				5e. TASK NUMBER
7. PERFORMING ORGANIZATION NAME(S) AND ADDRESS(ES) University of Minnesota Minneapolis, MN 55455-2070				8. PERFORMING ORGANIZATION REPORT NUMBER
				10. SPONSOR/MONITOR'S ACRONYM(S)
9. SPONSORING / MONITORING AGENCY NAME(S) AND ADDRESS(ES) U.S. Army Medical Research and Materiel Command Fort Detrick, Maryland 21702-5012				11. SPONSOR/MONITOR'S REPORT NUMBER(S)
				12. DISTRIBUTION / AVAILABILITY STATEMENT Approved for Public Release; Distribution Unlimited
13. SUPPLEMENTARY NOTES Original contains colored plates: ALL DTIC reproductions will be in black and white				
14. ABSTRACT Recent developments of piezocomposite transducer technology have led to the development of new generation of ultrasound phased arrays with imaging and therapeutic capabilities. These dual-mode arrays provide an ideal nonionizing noninvasive tool for the treatment of primary breast cancer. This project investigates the thresholds for tissue damage under a variety of exposure conditions to high-intensity focused ultrasound from dual-mode arrays. In addition, we investigate new imaging techniques for enhanced visualization of thermal lesions in tissue media. These investigations are carried on ex-vivo animal tissue and in-vitro breast tissue and will lead to the design of a new generation of phased array drivers capable of supporting both the imaging and therapeutic requirements of the dual-mode system. We have characterized the therapeutic and imaging capabilities of a 64-element array prototype in a variety of tissues and under a range of normal exposure and over-exposure conditions. In conjunction with this experimental study, we have developed the simulation code for prediction of tissue damage based on the transient bioheat equation (BHT). We have also designed and implemented a prototype data collection system that serves as the basis of a real-time system for image-guided therapy.				
15. SUBJECT TERMS Thermal ablation; Ultrasound Imaging; Noninvasive Surgery; Hyperthermia				
16. SECURITY CLASSIFICATION OF: a. REPORT U		17. LIMITATION OF ABSTRACT b. ABSTRACT U	18. NUMBER OF PAGES c. THIS PAGE U	19a. NAME OF RESPONSIBLE PERSON USAMRMC 19b. TELEPHONE NUMBER (include area code)
		UU	59	

Table of Contents

Cover.....	
SF 298.....	
Table of Contents.....	
Introduction.....	1
Body.....	1
Key Research Accomplishments.....	3
Reportable Outcomes.....	4
Conclusions.....	5
References.....	5
Appendices.....	5

Introduction

High-intensity focus ultrasound (HIFU) is gaining wider acceptance in noninvasive or minimally invasive targeting of abnormal tissues (e.g. cancer) for destruction. Piezocomposite transducer technology, especially for phased arrays, is providing high-quality HIFU applicators with increased bandwidth and reduced parasitic cross coupling between the array elements. In addition to increasing the efficacy of HIFU applicators, these technological enhancements allow for the use of HIFU arrays in imaging the target region before, after, and intermittently during lesion formation. This leads to a unique paradigm of image-guided surgery with HIFU in which the coordinate systems for both therapy and imaging are inherently registered. This project investigates the feasibility of using piezocomposite phased arrays as dual-mode ultrasound array (DMUA) applicators for the noninvasive treatment of primary breast cancers. Both therapeutic and imaging capabilities of the dual-mode arrays are investigated leading to a real-time dual-mode array system to be used in pursuing *in vivo* animal experiments in the future.

During the last four years (original funding period plus one-year, no-cost extension), we have demonstrated the lesion formation and imaging capabilities of the DMUA. This includes an experimental verification of one of the most important advantages of DMUA applicators for noninvasive surgery. Specifically, we have demonstrated the feasibility of image-based feedback for refocusing in the presence of strongly scattering critical targets, e.g. major blood vessels or ribs or bony structures. This work, which was presented at the International Symposium on Biomedical Imaging (ISBI'04) as an invited paper, demonstrates the unique advantage of DMUA applicators over other forms of guidance. We have also received an invitation by Dr. Ernest Fellipa at the Riverside Research Institute to submit a journal paper on the topic in a special commemorative issue for the late Dr. Fredrick Lizzi. This paper is in preparation and will be submitted in January 2006.

In addition, we have developed new nonlinear imaging methods based on the 2nd order Voleterra filter (SoVF) model that led to significant enhancement in the image quality of DMUA systems. We have also, investigated the detection and mapping of HIFU-induced lesions using commercial diagnostic scanners.

Body

This report is structured in accordance with the approved statement of work (SoW). In what follows, we give the tasks and subtasks of the approved SoW with each subtask followed directly by what has been accomplished with respect to it. For the subtasks planned for years 2 and 3 of the grant period, they are given here for completeness, but no comments follow these subtasks.

Task 1. Thresholds for Thermal Ablation of Breast and Fatty Tissue (Months 1 – 12):

- a) *Investigation of the intensity/exposure threshold curve; lesion size and characterization of damage (1 – 3): Completed (Year 1 Report)*
- b) *Imaging of discrete thermal lesions with therapeutic arrays (1 – 3): Completed (Year 1 Report).*
- c) *Long-duration volumetric ablation of porcine fatty tissue (3 – 9): Completed (Year 1 Report).*
- d) *Imaging of volumetric ablations using the therapeutic array and diagnostic scanners (3 – 12): Completed (Year 2 Report).*

Image-Guided Surgery of Primary Breast Cancer Using Ultrasound Phased Arrays

Emad S. Ebbini, PI

Task 2. Treatment Planning and Optimization of Volumetric Ablation with Phased Arrays in Fatty Tissue (Months 6 – 24):

- a) *Thermal modeling based on bioheat equation and Saparato and Dewey thermal dose integral for damage: Discrete lesions (6 – 12):* Completed (Year 1 Report)
- b) *Thermal modeling for multiple lesions with variable levels of proximity and cooling time between shots (12 – 18):* Completed (Year 2 Report).
- c) *Optimization of multiple-focus phased array patterns for simultaneous placement multiple discrete lesions (12 – 24):* Completed. Simulation study results are consistent with our previous publications and expectations stated in Year 2 Report. The current DMUA prototype is capable of producing up to 4 high-quality foci simultaneously. This should help reduce the treatment time for volumetric lesions by a factor of 4 for a conventional raster of focal points is used.

Task 3. Detection and Localization of Cavitation Activity During Thermal Lesion Formation in Breast and Fatty Tissue (Months 1 – 24):

- a) *Detection of subharmonic activity in single-channel and beamformed data (1 – 12):* Completed (Year 1 Report).
- b) *Localization of cavitation from beamforming of multiple receiving channels (12 – 24):* We have the electronics and the systems ready to perform this task. However, due to the malfunction of significant fraction of array elements, we are hesitant to drive the DMUA prototype at high level to produce cavitation in tissue. *Since we have not yet reached an agreement with the manufacturer, we did not receive a new prototype and this goal could not be pursued.* We are confident that we will be able to test this goal once the new DMUA is received, but *this will have to be done under a future research project. We note that our earlier results on overexposure conditions in HIFU lesion formation have shown the feasibility of detection and localization of cavitation. We only need to show if the DMUA can localize the onset of cavitation under normal exposure condition.*
- c) *Localization using time-frequency and related methods (6 – 18):* Completed (Year 2 Report)

Task 4. Image Characterization of Thermal Lesions in Breast and Fatty Tissue (Months 1 – 24)

- a) *Characterization of grayscale images for discrete thermal lesions (1 – 6):* Completed (Year 1 Report).
- b) *Characterization of tissue dependent parameters (1 – 12):* Completed (Year 1 Report: (Expected) negative results).
- c) *Characterization of second harmonic imaging (12 – 24):* Completed (Year 2 Report).
- d) *Correlation of imaging parameters with histologic characterization of tissue ablations (12 – 24):* We have obtained limited *in vitro* and *in vivo* lesion formation data using a 4-MHz single-element transducer (Courtesy of Focus Surgery, Inc., Indianapolis, IN). We plan to use this as preliminary data for an NIH proposal on the subject. We are currently developing new quantitative measurements for lesion detection and characterization.

Task 5. Image-based Adaptive Refocusing of Therapeutic Arrays in Inhomogeneous Fatty Tissue (Months 12 – 24)

- a) *Focusing with reference to natural specular targets (12 – 18):* Completed (Year 2 Report).
- b) *Temperature feedback (12 – 24):* Completed (See Task 6 subtask d).

Image-Guided Surgery of Primary Breast Cancer Using Ultrasound Phased Arrays

Emad S. Ebbini, PI

- c) *Discrete thermal lesions as beacons (12 – 24):* RF data from single-shot lesions in porcine liver were analyzed and all normal lesion data sets clearly showed a strong localized echo from the near boundary of the lesion that can be reliably used for focusing. We believe that we can further refine this idea by creating extremely small lesions amounting to point reflectors. Consequently, the quality of focusing can be significantly improved.

Task 6. Real-time Dual-mode Phased Array System for Volumetric Thermal Ablation of Breast and Fatty Tissue (Months 1 – 36)

- a) Design and fabrication of 64-channel receive system (1 – 12): A 64-channel diplexer circuit allowing the use of each array element in transmit and receive has been fabricated and tested. In addition, 8-to-1 multiplexer boards were designed and fabricated to allow data collection from 8 receiving elements on one analog-to-digital converter (A/D). This will reduce the hardware cost of the system without severely compromising the real-time nature of image data collection. Please see d) below for an example of how this new receiver system was used.
- b) Design and fabrication of transmit/receive control circuitry (1 – 18): Completed (Year 1 Report).
- c) DSP-based real-time beamformer (12 – 30): During the one-year cost extension, we have begun to implement the real-time phased array controller on a Spartan III FPGA (field programmable gate array) from Xilinx, Palo Alto, CA. The new driver offers phase resolution up to 1.8° phase and 0.01 amplitude resolution (compared to 11.5° phase and 0.07 amplitude resolution with the current system).
- d) Experimental testing, calibration, and characterization of imaging system (24 - 36): Real-time data collection from 8 channels to a single A/D has been demonstrated during a 9-second heating experiment. Not only were we able to demonstrate beamforming but we were also able to extract temperature rise from the focus location. The figure below shows the estimated temperature change near the geometric focus of the dual-mode array (at 100 mm) due to the 9-second heating pulse from the same array. The open circles indicate the instants when the data was collected for temperature calculations. As can be seen from the figure, noninvasive temperature estimates were made at 3 and 6 seconds during heating. The heating pulse was interrupted for 100 ms for data collection for each measurement point. This includes the communications time for the controlling computer. If a real-time operating system were used, it would have taken less than 2 milliseconds to collect the imaging data for temperature calculation. The acquisition time can be reduced further if we dedicate more A/Ds on the receiver side, i.e. one per 4 receiving elements instead of 1 per 8.

Key Research Accomplishments

- First demonstration of a DMUA in forming lesions *ex vivo* and imaging the changes in tissue echogenicity from the lesion location and surrounding tissues (Appendix I).
- Demonstrated the nonlinear nature of echoes from lesion location and the advantage of harmonic and nonlinear imaging (based on SoVF) in improving the image contrast of HIFU-induced lesions (Appendix II).

Image-Guided Surgery of Primary Breast Cancer Using Ultrasound Phased Arrays

Emad S. Ebbini, PI

- First one-to-one comparison of imaging performance of a dual-mode array with a diagnostic transducer (Appendix III).
- First demonstration of image-based feedback for refocusing the array in the presence of strongly scattering target (Appendix IV).

Reportable Outcomes

- E.S. Ebbini, J. Coad, and J. Bischof, "Lesion formation and visualization using dual-mode ultrasound phased arrays," Proceedings of the 2001 IEEE Ultrasonics Symposium, Volume: 2, Oct 8-11, 2002, Page(s): 1351 – 1354.
- H. Yao, P. Phupattaranont, and E.S. Ebbini, "Enhanced lesion visualization in image-guided noninvasive surgery with ultrasound phased arrays," Proc. Of 23rd IEEE Int. Conf. on Eng. In Medicine and Biology, pp. 2492 – 2495, 2001.
- C. Steidl, H. Yao, P. Phukpattaranont, and E.S. Ebbini, "Dual-mode ultrasound phased arrays for noninvasive surgery: post-beamforming image compounding algorithms for enhanced visualization of thermal lesions," Biomedical Imaging, 2002. Proceedings. 2002 IEEE International Symposium on , 7-10 July 2002, Page(s): 429 -432.
- H. Yao, P. Phukpattaranont, and E.S. Ebbini, "Nonlinear methods for visualization of HIFU-induced lesions," Proceedings of the 2nd International Symposium on Therapeutic Ultrasound, 29 July – 1 August, Seattle, WA, Editors: Andrew, Crum, and Vaezy, 2002, Page(s): 282 – 289.
- H. Yao, P. Phukpattaranont, and E.S. Ebbini, "Detection and mapping of thermal lesions using dual-mode ultrasound phased arrays," Proceedings of the 2002 IEEE Ultrasonics Symposium, Volume: 2, Oct 8-11, 2002, Page(s): 1435 -1438.
- H. Yao, P. Phukpattaranont, and E.S. Ebbini, "Nonlinear imaging methods for characterization of HIFU-induced lesions," Proceedings of the SPIE vol. 4954, Thermal Treatment of Tissue: Energy Delivery and Assessment II, Editor: T.P. Ryan, 2003, Page(s): 183 – 191.
- P. Phukpattaranont and Ebbini, E.S., "Post-beamforming second-order Volterra filter for pulse-echo ultrasonic imaging," *IEEE Trans. on Ultrasonics, Ferroelectrics, and Frequency Control*, vol. 50(8), pp. 987-1001, Aug. 2003.
- H. Yao and E.S. Ebbini, "Imaging with Large-Aperture Arrays with Heterogeneous Directive Elements," Proc. 2003 IEEE Ultrasonics Symposium, vol., pp. 1243 - 1246.
- H. Yao and E.S. Ebbini, "Real-time Monitoring of the Transients of HIFU-induced Lesions," Proc. 2003 IEEE Ultrasonics Symposium, vol., pp. 1006 - 1009.
- H. Yao and E.S. Ebbini, "Dual-mode Ultrasound Phased Arrays for Imaging and Therapy," Special Session on Advanced Methods in Ultrasound Imaging, ISBI 2004, Arlington, VA, April 2004, vol. 1, pp. 24 – 27, 2004. (*Invited Paper*).
- Invited paper at the 147th Meeting of the Acoustical Society of America in New York, NY, May 24 - 28, 2004 (abstract entitled Monitoring of HIFU-induced Lesions Using Active Imaging Methods by Hui and Ebbini).
- Yao and Ebbini, "Refocusing of Dual-mode arrays in the presence of strongly scattering objects," Proc. 2004 IEEE Ultrasonics Symposium, vol. 1, pp. 239 – 242, 2004.
- Yao and Ebbini, "Noninvasive Localized Ultrasonic Measurement of Tissue Properties," Proc. 2004 IEEE Ultrasonics Symposium, vol. 1, pp. 724 – 727, 2004.
-

Image-Guided Surgery of Primary Breast Cancer Using Ultrasound Phased Arrays

Emad S. Ebbini, PI

- H. Yao, *Active Ultrasonic Imaging Methods for HIFU-induced Lesions*, Ph.D. Dissertation, University of Minnesota, 2006 (defended 2005).

Conclusions

After characterizing and optimizing the imaging capabilities of the DMUA prototype in year 2, we have experimentally demonstrated one of the most important advantages of these arrays in noninvasive surgery. Namely, we have demonstrated the feasibility of using image-based feedback to refocus DMUAs in the presence of strongly scattering targets. We have also begun the investigation of quantitative imaging of HIFU-induced lesions through active imaging methods. Specifically, we are developing techniques for measuring local absorption, perfusion, and elastic properties of HIFU-induced lesions. We are developing these techniques using both diagnostic scanners and our DMUA prototypes.

References

- [Ebbini:91] E. Ebbini and C. Cain, "A spherical-section ultrasound phased array applicator for deep localized hyperthermia," *IEEE Trans. Biomed. Eng.*, vol. 38, pp. 634-643, 1991.
- [Seip:95a] R. Seip and E. Ebbini, "Non-invasive estimation of tissue temperature response to heating fields using diagnostic ultrasound," *IEEE Trans. Biomed. Eng.*, vol. 42, no. 8, pp. 828-839, August 1995.
- [Seip:95b] R. Seip, P. VanBaren, C. Simon, and E. Ebbini, "Non-invasive spatio-temporal temperature change estimation using diagnostic ultrasound," in *IEEE Ultrason. Symp.*, pp.1613-1616, November 1995.
- [Seip:96a] R. Seip, *Feedback for Ultrasound Thermotherapy*, PhD thesis, EECS, University of Michigan, February 1996.
- [Seip:96b] R. Seip, P. VanBaren, C. Cain, and E. Ebbini, "Non-invasive real-time multipoint temperature control for ultrasound phased array treatments," *IEEE Trans. Ultrason., Ferroelec., Freq. Contr.*, vol. 43, no. 6, pp.1063-1073, November 1996.
- [Simon:98c] C. Simon, P. VanBaren, and E. Ebbini, "Two-dimensional temperature estimation using diagnostic ultrasound," *IEEE Trans. Ultrason. Ferroelec., Freq. Contr.*, vol. 45, no. 4, pp. 1088-1099, July 1998.

Appendices

- I. E.S. Ebbini, J. Coad, and J. Bischof, "Lesion formation and visualization using dual-mode ultrasound phased arrays," Proceedings of the 2001 IEEE Ultrasonics Symposium, Volume: 2, Oct 8-11, 2002, Page(s): 1351 – 1354.
- II. P. Phukpattaranont and Ebbini, E.S., "Post-beamforming second-order Volterra filter for pulse-echo ultrasonic imaging," *IEEE Trans. on Ultrasonics, Ferroelectrics, and Frequency Control*, vol. 50(8), pp. 987-1001, Aug. 2003.
- III. Yao and Ebbini, "Imaging with Large-Aperture Arrays with Heterogeneous Directive Elements," Proc. 2003 IEEE Ultrasonics Symposium, vol., pp. 1243 - 1246.
- IV. Yao and Ebbini, "Dual-mode Ultrasound Phased Arrays for Imaging and Therapy," Special Session on Advanced Methods in Ultrasound Imaging, ISBI 2004, Arlington, VA, April 2004.

LESION FORMATION AND VISUALIZATION USING DUAL-MODE ULTRASOUND PHASED ARRAYS

Emad S. Ebbini¹, John C. Bischof², and James E. Coad³

¹Department of Electrical and Computer Engineering

²Department of Biomedical Engineering

³Laboratory Medicine and Pathology, Academic Health Center

University of Minnesota

Minneapolis, MN 55455

Abstract- A 1 MHz spherical-section 64-element linear piezo-composite phased array and a supporting driving and data acquisition system were recently tested for use as a dual-mode HIFU applicator system. In therapeutic mode, the array was shown to be capable of producing focal intensities in excess of 3500 W/cm² at its geometric center (100 mm radius of curvature). Imaging tests of quality assurance tissue-mimicking phantoms as well as computer simulations confirmed that the array has an oval-shaped imaging field of view ($IxFoV$) with nearly 50 dB dynamic range extending from 70 to 120 mm in the axial direction and ± 20 mm in the transverse direction [1]. This is larger than its therapeutic operating field ($ThxOF$), which is defined as the region around the geometric focus where the loss in intensity gain is within 1 dB from the intensity gain at the geometric center. We have tested the array imaging capability in the visualization of the formation of discrete and volumetric lesions in freshly excised porcine liver samples. Experimental results clearly show that the enhancement of the tissue echogenicity at the lesion location is more pronounced in the harmonic images when compared to images at the fundamental. Results also clearly show that the harmonic imaging mode produces more accurate mapping of the lesion size and shape as determined by histologic evaluation.

1. INTRODUCTION

Image guidance has long been recognized as the "enabling technology" for noninvasive or minimally invasive thermal surgery. Highly refined energy application devices have been introduced for many years. However, without reliable imaging techniques for visualization of thermal lesions, noninvasive thermal surgery has failed to find widespread acceptance in the clinic. Recently, image guidance methods based on well established imaging modalities like MRI[8], CT[9], or ultrasound [10, 5] have been proposed. Other

Funded by Grant DAMD 17-01-1-330 from the US Army Medical Research and Materiel Command.

imaging modalities are also being developed and may become available in the foreseeable future [2].

An area unique to ultrasound that could revolutionize the field of image guided surgery is the development of a new generation of dual-mode high-power phased array systems capable of both imaging and therapy [1]. These piezocomposite transducers can produce focal intensity levels needed for ablative and coagulative thermal surgery with high precision. Furthermore, the operating bandwidth of such transducers allows for imaging the treatment region with adequate image quality to delineate important landmarks within and around the target volume. With these capabilities, it is possible to operate these arrays in a "self-registration" mode whereby the array's imaging capabilities are utilized in characterization of the tissue response precisely at the expected lesion location. This is due to the fact that the beamforming is common to both the imaging and therapy modes.

In this paper we present results of lesion formation and visualization using a 64-element 1 MHz array originally designed for therapeutic applications [4].

2. DUAL-MODE PHASED ARRAY SYSTEM FOR NONINVASIVE SURGERY

A variety of nonplanar phased array geometries for therapeutic applications have been investigated thoroughly since the late 1980s [7]. Briefly, optimally designed therapeutic arrays have the following geometrical characteristics:

- Nonplanar with radius of curvature and f -number determined by the depth and volume of the $ThxOF$ (f -numbers typically ~ 1).
- Coarsely sampled with element dimensions $\sim 1 - 3\lambda$ to maintain high efficiency. Maximum element size is limited by the extent of $ThxOF$; element directivity variation within $ThxOF$ is ~ 1 dB.

Unfortunately, these characteristics render the imaging capabilities of therapeutic arrays poor due to their unacceptably high grating lobe levels. However, it is possible to design nonplanar therapeutic arrays with limited *FOV* covering or exceeding the extent of their *ThxOFs*. This limited imaging capability can be quite significant in that it potentially allows:

- Visualizing critical structures in the vicinity of the target point(s), e.g., blood vessels, bone or gas spaces.
- Measuring temperature dependent changes that may allow the assessment of the quality of the therapeutic beam *in situ* at sub-therapeutic (i.e., nondestructive) levels.
- Monitoring the effects of the therapeutic beam during and/or immediately after lesion formation.

We have designed and tested a 64-element 1D array on a spherical surface as a prototype for a dual-mode transducer for noninvasive surgery. In previous publications [1, 5, 6], we have demonstrated the imaging capabilities of this array and its *IxF*oV. In addition, we have shown that it is possible to perform noninvasive temperature imaging using this array [1]. In this report, we demonstrate the feasibility of imaging thermal lesions in freshly excised tissue samples.

2.1. Imaging Characterization

2.1.1. Data collection system

The data system collection for purposes of image formation is shown in Figure 1. The array is connected to a 64-channel pulser/phased array driver capable of driving the array in continuous or pulsed mode with time resolution of 25 nanoseconds. Channel delays from 25 ns to 1 ms can be realized with this driver. In its current form, the receiver channel data is connected to a 23-bit 20 MSample/second digitizer through a 4×64 matrix switch.

2.1.2. Image Formation Model

Figure 1 summarizes the image acquisition and image formation model. A 64-element array optimized for maximum energy delivery at 1 MHz operating frequency is used for lesion formation in sample tissue. Lesions are formed by focusing the array at a point within the target and maintaining high-power output for time intervals on the order of seconds (1 - 5 seconds typical). The power is interrupted for short intervals (milliseconds) to acquire image data by transmitting short (μ s) pulses from all 64-elements and receiving on selected elements using a matrix switch. Once the image data set is collected, RF beamforming is performed to form standard echographic images of the target region. It is well known that these images have very low contrast due to the coherent nature of image acquisition which produces speckle. This renders the lesion detection

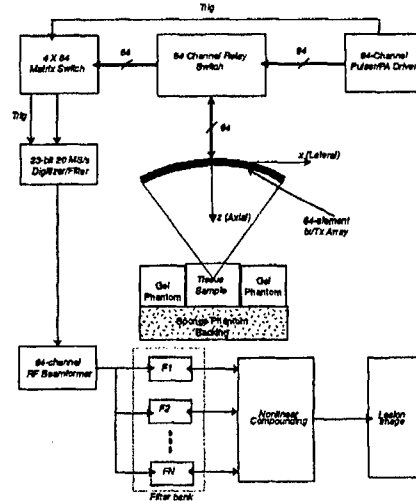


Fig. 1. Experiment setup and image reconstruction algorithm for the 64-element dual-mode array.

very difficult using ultrasound. However, due to the nonlinearity of echoes from freshly formed thermal lesions, (second) harmonic imaging provides significant improvement in contrast for purposes of lesion detection and mapping.

2.1.3. Harmonic Imaging

Due to the double resonance characteristics of the 64-element array described in [1], it is easy to form second harmonic images by post-beamforming filtering of RF data to eliminate the fundamental. Of course, second harmonic imaging requires the full transmit power be used for transmit beams as opposed to the synthetic aperture approach in which each array element is driven separately as a transmitter. Therefore, for harmonic imaging, we have used the 64-channel driver to form full transmit beams directly for each reception. The images obtained using this technique are referred to as single-transmit images. These images are equivalent to full data sets along the transmit focus direction, but are otherwise compromised. While this may seem like an unacceptable degradation, it does have distinct advantages in image-guided surgery. When the transmit imaging beam has the same structure as the therapeutic beam, single-transmit images allow for the visualization of any critical structures near or along the line of sight of the target point. This can be used to modify the focusing and steering parameters of the therapeutic beam to avoid or target these critical structures. It is also useful in isolating specular reflectors, e.g., large blood vessels, that may be useful in characterizing the quality of the therapeutic beam in the vicinity of the target. As we show below, this mode is extremely useful in visualization of discrete thermal lesions when used in both the

fundamental and in the second harmonic modes.

2.2. Therapeutic Characterization

The 64-element piezocomposite array described above was extensively tested as a high-power therapeutic applicator. Discrete and volumetric thermal lesions were formed *in vitro* bovine muscle [4]. More recently, we have performed a series of experiments for forming discrete and volumetric lesions in porcine liver using the setup shown in Figure 1. To illustrate one of the unique capabilities of phased arrays in forming lesions of various shapes, Figure 2 shows two cigar-shaped lesions formed in porcine liver simultaneously using a double-focus pattern with focal intensity of 660 W/cm^2 at each focus applied for 4 seconds. It has been determined that this array is capable of producing focal intensity levels of over 3500 W/cm^2 in well-degassed water. This level of focal intensity is sufficient to produce a full range of known therapeutic effects of ultrasound.

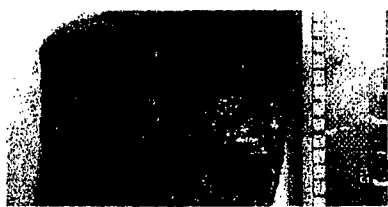


Fig. 2. Two cigar-shaped lesions formed in porcine liver sample after 4-second exposure to a double-focus beam pattern produced by the 64-element therapeutic array.

3. HISTOLOGIC EVALUATION

The liver was cut with approximate square cross section of $4.5 \times 4.5 \text{ cm}^2$ so they fit snugly within the sample holder without being squeezed. Samples were brought in containers in saline buffer within an hour of sacrificing the animal. Histological measurements were made for identified lesion and comparisons with gross measurements were made. Cross sectional cuts into the samples were made in planes parallel to the face of the array (i.e., at fixed axial distance) to insure finding each lesions that is formed. The following zones of damage were identified:

- At the center of each lesion, cells undergo vital enzyme protein denaturation. For higher dose levels, ablation and evidence of water vaporization can be observed in this central zone as well.
- An outer ring of pyknotic nuclei with thickness between $0.1 - 0.5 \text{ mm}$ is variably present for all lesion.
- An inner ring with nuclei in this zone show a transition between pyknotic nuclei of the outer ring and the

central zone cells that have undergone vital enzyme protein denaturation.

A variety of exposure levels and durations varying from under exposure (low probability of lesion formation) to over exposure (strong cavitation and distorted lesion formation) were examined at histological cross sections 2 mm apart starting 5 mm into the tissue sample covering the full extent of the lesion. The far end of the lesion was always a point and it occurred at the geometric center of the array. The near end and the maximum lateral cross section of the lesion depend on the exposure level. Normal exposure levels produced expected cigar-shaped lesions of length proportional to intensity. Over exposures, on the other hand, produced inverted-cone lesions with the near end extending to the front surface of the sample in some cases (surface burns).

4. LESION VISUALIZATION

Figure 3 shows 25-dB gray scale images obtained using the single-transmit imaging mode (transmit focus at 0 lateral and 100 axial) obtained before (left) and after (right) single lesion formation (4 seconds at 850 W/cm^2). The top pair was formed at the fundamental and the bottom pair was formed at the second harmonic. For each pair, the before and after images were normalized with respect to the maximum in the image after.

The images acquired after lesion formation both show increased echogenicity at the lesion location starting at 92 mm. This is consistent with the histologic evaluation of the sample. The images also suggest that the extent of the lesion is 8 mm, also in accordance with histologic evaluation. It should be mentioned, however, that the boundaries of the lesion are much easier to detect in the second harmonic image.

Figure 4 shows 25-dB gray scale images obtained using the single-transmit imaging mode (transmit focus at 0 lateral and 100 axial) obtained before (left) and after (right) single lesion formation (4 seconds at 1200 W/cm^2). This is only a 20% change in dose delivered to the focus compared to the previous case. Here the images acquired after lesion formation suggest a lesion of 10 mm length starting at 90 mm, both in accordance with histological evaluation. As in the previous case, the second harmonic images show significant increase in echogenicity at the lesion location compared to the fundamental.

5. CONCLUSIONS

The first experiment represent a fairly homogeneous target tissue while the second has a pair of blood vessels at the target location as can be seen from the images taken before lesion formation. While both the fundamental and harmonic images show enhanced lesion contrast in both cases,

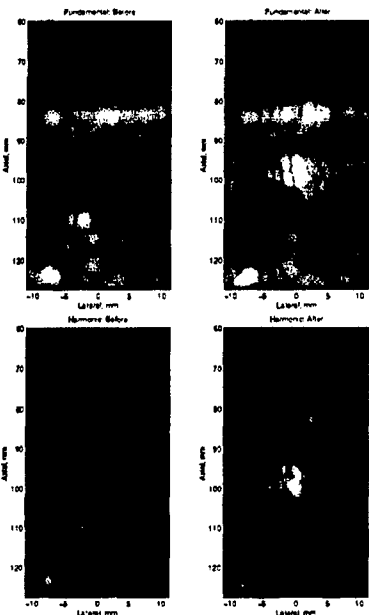


Fig. 3. Fundamental (top) and second harmonic (bottom) images before (left) and after lesion formation using a single focus (4 seconds at 850 W/cm^2).

the harmonic images show a net increase in contrast by 22 dB in the second case. On the other hand, the net increase in contrast at the fundamental is about 7 dB. In addition, the spatial definition of the lesion in the harmonic images is superior to the fundamental.

The results shown, in addition to numerous similar experiments, suggest that the second harmonic single-transmit images can be used to detect even small changes in the starting point of formed lesions. This applies to a variety of exposure conditions, including *over exposure*. The results of these experiments also show that the lesion images are in good agreement with histological examinations, including lesion shapes. These results will be reported in an upcoming publication.

6. REFERENCES

- [1] C. Simon, J. Shen, T. Hall, and E. Ebbini, "Combined ultrasound image guidance and therapy using a therapeutic phased array," *SPIE Medical Imaging 1998*, vol. 3341, pp. San Diego, Feb. 1998.
- [2] K.Paulsen, M.Moskowitz, T.Ryan, S.Mitchell, and P.Hoops, "Initial *in vivo* experience with EIT as a thermal estimator during hyperthermia," *Int. J. Hyperthermia*, vol. 12, no. 5, pp. 573-591, Sept. 1996.
- [3] P.Meaney, K.Paulsen, A.Hartov, and R.Crane, "Microwave imaging for tissue assessment: Initial evaluation in multitar-
- [4] P. VanBaren, C. Simon, R. Seip, T. Solf, C. Cain, and E. Ebbini, "Image-guided phased array system for ultrasound thermotherapy," *IEEE Ultrason. Symp.*, pp. 1269-1272, Nov. 1996.
- [5] E. Ebbini, P. VanBaren, and C. Simon, "Image-guided non-invasive surgery with ultrasound phased arrays," *SPIE Bios: Surgical Applications of Energy*, 1998.
- [6] P. Phukpattarnont, H. Yao, and E. Ebbini, "Enhanced Lesion Visualization in Image-Guided Noninvasive Surgery with Ultrasound Phased Arrays," *IEEE Engineering in Medicine and Biology*, Istanbul, Turkey, 2001.
- [7] E. Ebbini, *Deep Localized Hyperthermia with Ultrasound Phased Arrays Using the Psudoinverse Pattern Synthesis Method*. Ph.D. Dissertation, University of Illinois, 1990.
- [8] K.Hynynen, "Review of ultrasound therapy," *1997 IEEE Ultrasonics Symposium*, vol. 2, pp. 1305-1313, 1997.
- [9] J. Jenne, M. Bahner, J. Spoo, P. Huber, R. Rastert, I. Simiantonakis, W. Lorenz, and J. Debus, "CT on-line monitoring of HIFU therapy," *IEEE Ultrason. Symp.*, 1997.
- [10] N. Sanghvi *et al.*, "Noninvasive surgery of prostate tissue by high-intensity focused ultrasound," *IEEE Trans. UFFC*, vol. 43, no. 6, pp. 1099-1110, Nov. 1996.

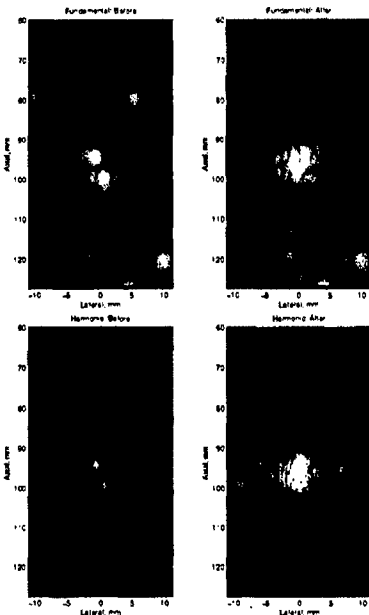


Fig. 4. Fundamental (top) and second harmonic (bottom) images before (left) and after lesion formation using a single focus (4 seconds at 1200 W/cm^2).

get tissue-equivalent phantoms," *IEEE Trans. Biomed Eng.*, vol. 43, no. 9, pp. 878-890, Sept. 1996.

APPENDIX II

Post-Beamforming Second-Order Volterra Filter for Pulse-Echo Ultrasonic Imaging

Pornchai Phukpattaranont and Emad S. Ebbini, *Member, IEEE*

Abstract—We present a new algorithm for deriving a second-order Volterra filter (SVF) capable of separating linear and quadratic components from echo signals. Images based on the quadratic components are shown to provide contrast enhancement between tissue and ultrasound contrast agents (UCAs) without loss in spatial resolution. It is also shown that the quadratic images preserve the low scattering regions due to their high dynamic range when compared with standard B-mode or harmonic images. A robust algorithm for deriving the filter has been developed and tested on real-time imaging data from contrast and tissue-mimicking media. Illustrative examples from image targets containing contrast agent and tissue-mimicking media are presented and discussed. Quantitative assessment of the contrast enhancement is performed on both the RF data and the envelope-detected log-compressed image data. It is shown that the quadratic images offer levels of enhancement comparable or exceeding those from harmonic filters while maintaining the visibility of low scattering regions of the image.

I. INTRODUCTION

INCREASING interest in extending the capabilities of ultrasound imaging by utilizing ultrasound contrast agents (UCAs) has heightened the need for more suitable imaging techniques. In standard B-mode imaging, UCAs increase the echogenicity from perfused tissues [1]. This results in improved endocardial border detection in left ventricular opacification, which leads to a better analysis of wall motion abnormalities [2]. Nevertheless, in the myocardium where the ratio of blood volume to tissue is quite low (approximately 10% [3]), the backscatter from the small number of microbubbles in vessels can be dominated by echoes from surrounding tissue. In this occurrence, standard B-mode imaging offers inferior UCA detectability in the presence of tissue, stated as agent-to-tissue ratio [4]. In order to increase the sensitivity of UCA detections, various new imaging techniques [5], [6] have been developed by employing some specific acoustic signatures of UCAs, such as nonlinear and transient scattering.

Imaging techniques based on nonlinear oscillations have been designed for separating and enhancing nonlinear UCA echoes from a specified region of interest within the imaging field, including second harmonic (SH) B-mode

imaging and pulse inversion (PI) Doppler imaging [7]. The SH imaging employs a fundamental frequency transmit pulse and produces images from the second harmonic component of received echoes by using a second harmonic bandpass filter (BPF) to remove the fundamental frequency. In order to increase UCA detection sensitivity in the limited transducer bandwidth condition, spectral overlap between fundamental and second harmonic parts need to be minimized by transmitting narrow-band pulses resulting in an inherent tradeoff between contrast and spatial resolution.

In PI imaging, a sequence of two inverted acoustic pulses with appropriate delay is transmitted into tissue. Images are produced by summing the corresponding two backscattered signals. In the absence of tissue motion, the resulting sum can be shown to contain only even harmonics of the nonlinear echoes [7]. The PI imaging overcomes the tradeoff between contrast and spatial resolution because it utilizes the entire bandwidth of the backscattered signals [7]. As a result, superior spatial resolution can be achieved when compared with SH imaging. Moreover, it has been shown that PI imaging can be operated in a continuous imaging mode with low mechanical indices (MIs) [8]. The PI imaging is sensitive to tissue motion because it is a multiple pulse technique; therefore, PI detection is combined with Doppler detection leading to a new technique called PI Doppler. The PI Doppler utilizes the advantages from both detection schemes and circumvents the tissue motion problem [7]. Nevertheless, an inherent multipulse technique of PI imaging results in the reduction of imaging frame rates.

In order to detect backscattered signals due to UCAs in pulse-echo ultrasound imaging with single transmit pulse per line and overcome the tradeoff between contrast and spatial resolution, we have developed a new imaging technique based on the Volterra filter [9]. The Volterra filter is a dynamic filter that operates in parallel on the linear, quadratic, cubic, etc., signal components to produce its output. It has a discrete convolutional form with finite memory that is commonly used in nonlinear digital signal processing (DSP) applications [10]. While the Volterra filter output is nonlinear in terms of the input data, it is linear in terms of its coefficients. As a result, linear processing can be applied to identify Volterra kernels (i.e., filter coefficients). The identification of Volterra kernels has been demonstrated in several applications [10], [11]. For example, the linear and quadratic Volterra kernels identified by an adaptive filtering algorithm based on recursive least-squares approach of a second-order Volterra model

Manuscript received October 23, 2002; accepted March 21, 2003. This work is funded in part by a grant from Esaote, S.p.A., Genoa, Italy and by Grant DAMD 17-01-1-330 from the U.S. Army Medical Research and Materiel Command.

The authors are with the Electrical and Computer Engineering Department, University of Minnesota, MN (e-mail: emad@ece.umn.edu).

are applied to separate the linear and quadratic responses of a tension leg platform [12].

In this paper, we present postbeamforming nonlinear filter based on the second-order Volterra filter (SVF). The filter is capable of separating linear and quadratic components from UCA-backscattered signals. Filter coefficients can be identified by forming a system of linear equations from a beamformed RF data segment in the UCA or tissue region and obtained by solving a minimum-norm least-squares (MNLS) problem. It is shown that the system identification approach to a nonlinear ultrasonic imaging is robust and can be applied to form nonlinear images throughout the imaging field, i.e., not confined to the region where the filter coefficients were derived. Images produced from quadratic output of the SVF model exhibit excellent contrast enhancement without loss in spatial resolution. In addition, quadratic images have increased dynamic range compared to standard B-mode and harmonic images allowing the preservation of image features along with contrast improvement.

II. THEORY

For simplicity and without loss of generality, we illustrate the nonlinear postbeamforming algorithm using the SVF model. The algorithm described in this section for deriving the filter coefficients of the SVF extends to higher order in a straightforward manner. Initial experience with this model indicate that it is largely sufficient for tissue response. Furthermore, the SVF is computationally feasible for real-time application with today's technology, which makes it more attractive from the implementation point of view.

A. Second-Order Volterra Model

Results from [9] have shown the validity of a SVF as a model for pulse-echo ultrasound pulse-echo data from tissue mimicking media. An input-output system identification approach was used to estimate the coefficients of the linear and quadratic components of the SVF in the frequency domain. However, while the system identification study was necessary to establish the applicability of SVF to ultrasound pulse-echo data, it is not useful for imaging purposes as it requires access to both the input and the echo data from distinct scatterers in the tissue-mimicking media. An appropriate approach for imaging operates on the beamformed RF data to separate the linear and quadratic components regardless of the input. This signal separation approach allows us to extract the linear and quadratic signal components from the beamformed data to form linear and/or quadratic images separately or compounded. In this paper, we emphasize the quadratic images obtained from the SVF model based on a linear and quadratic prediction model of beamformer output described in the remainder of this section.

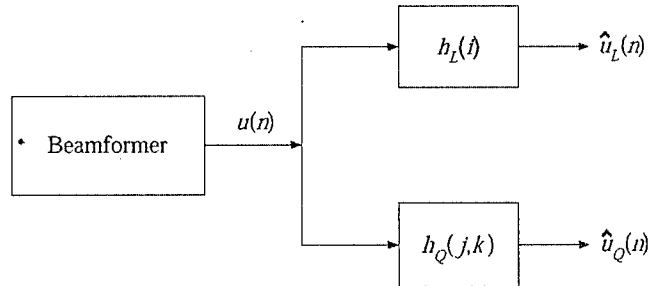


Fig. 1. Separation of beamformed RF data into linear and quadratic components using the SVF.

1. Signal Separation Model: Fig. 1 shows a simple block diagram of the imaging system based on SVF. The SVF operates on the beamformer output to produce the linear and quadratic components, $\hat{u}_L(n)$ and $\hat{u}_Q(n)$, respectively. Estimates of the total beamformer output can be obtained from these components simply by adding them

$$\hat{u}(n) = \hat{u}_L(n) + \hat{u}_Q(n), \quad (1)$$

where $\hat{u}(n)$, $\hat{u}_L(n)$, and $\hat{u}_Q(n)$ are the total, linear, and quadratic estimations, respectively. The separation of the linear and quadratic components can be achieved once the coefficients of the kernels, $h_L(i)$ (linear), and $h_Q(j, k)$ (quadratic) are found. In the following subsection, we describe a MNLS approach for determining these coefficients.

2. The MNLS Estimation of SVF Coefficients: The response of a quadratically nonlinear system with memory, $\hat{u}(n+1)$ can be predicted by a (discrete) second-order Volterra model operating on the m past samples as follows

$$\begin{aligned} \hat{u}(n+1) = & \sum_{i=0}^{m-1} u(n-i)h_L(i) \\ & + \sum_{j=0}^{m-1} \sum_{k=j}^{m-1} u(n-j)u(n-k)h_Q(j, k), \end{aligned} \quad (2)$$

where $h_L(i)$ is linear filter coefficients, and $h_Q(j, k)$ represents quadratic filter coefficients. Note that while $\hat{u}(n+1)$ is nonlinear with respect to the beamformed data, it is linear with respect to the coefficients of the linear and quadratic kernels of the SVF. Recognizing this fact, one can rewrite (2) in vector form

$$\hat{u}(n+1) = \mathbf{u}^T(n)\mathbf{h}, \quad (3)$$

where the data vector, $\mathbf{u}(n)$, is defined at sample n as

$$\mathbf{u}(n) = [u(n), u(n-1), u(n-2), \dots, u(n-m+1), u^2(n), u(n)u(n-1), \dots, u^2(n-m+1)]^T,$$

and the filter coefficient vector, \mathbf{h} , can be expressed as

$$\begin{aligned} \mathbf{h} = & [h_L(0), h_L(1), h_L(2), \dots, h_L(m-1), \\ & h_Q(0,0), h_Q(0,1), \dots, h_Q(m-1, m-1)]^T, \end{aligned}$$

where m is the system order and superscript T denotes the transpose. The total number of independent filter coefficients, N , is equal to $(m^2 + 3m)/2$ assuming a symmetrical quadratic kernel (i.e., $h_Q(j, k) = h_Q(k, j)$). Similarly, $\hat{u}(n+2), \hat{u}(n+3), \dots, \hat{u}(n+M)$ can be represented in the form of (3) and expressed in the matrix form

$$\mathbf{f} = \mathbf{G}\mathbf{h}, \quad (4)$$

where the vector \mathbf{f} and the matrix \mathbf{G} are defined as

$$\mathbf{f} = [u(n+1), u(n+2), \dots, u(n+M)]^T$$

and

$$\mathbf{G} = [\mathbf{u}(n), \mathbf{u}(n+1), \dots, \mathbf{u}(n+M-1)]^T,$$

where M is the number of linear equations (observations). The linear and quadratic filter coefficients can be estimated by seeking an appropriate solution of (4). Well-known solutions to (4) are the least squares (LS) solution for the overdetermined case (more constraints than unknowns) and the minimum norm (MN) solution in the underdetermined case (less constraints than unknowns). A MNLS solution can be obtained by

$$\mathbf{h}_{\text{MNLS}} = \mathbf{G}^\dagger \mathbf{f}, \quad (5)$$

where \mathbf{G}^\dagger is a generalized inverse [13]. This solution applies to both the overdetermined and underdetermined cases as it accounts for the effective rank of the matrix \mathbf{G} . In general, \mathbf{G} could be rank deficient, i.e., has rank $r \leq \min\{M, N\}$. When this is the case, there are infinite number of solutions to (4) that produce the same LS error, $\|\mathbf{f} - \mathbf{G}\mathbf{h}_{\text{LS}}\|^2$. The MNLS is the unique solution to (4) with minimum norm, i.e., $\|\mathbf{h}_{\text{MNLS}}\|^2 < \|\mathbf{h}_{\text{LS}}\|^2 \forall \mathbf{h}_{\text{LS}}$. The singular value decomposition (SVD) of \mathbf{G} is given by

$$\begin{aligned} \mathbf{G} &= \mathbf{U}\Sigma\mathbf{V}^T \\ &= \sum_{i=1}^r \sigma_i \mathbf{u}_i \mathbf{v}_i^T, \end{aligned} \quad (6)$$

and

$$\begin{aligned} \mathbf{G}^\dagger &= \mathbf{V}\Sigma^\dagger\mathbf{U}^T \\ &= \sum_{i=1}^r \frac{1}{\sigma_i} \mathbf{v}_i \mathbf{u}_i^T, \end{aligned} \quad (7)$$

where Σ is a $M \times N$ diagonal matrix with singular values $\sigma_1 \geq \sigma_2 \geq \dots \geq \sigma_r > \sigma_{r+1} = \dots = \sigma_p = 0$ ($p = \min\{M, N\}$). The matrices \mathbf{U} ($M \times M$) and \mathbf{V} ($N \times N$) are formed from the columns $\{\mathbf{u}_i\}_{i=1}^M$ and $\{\mathbf{v}_i\}_{i=1}^N$, which are the orthogonal eigenvectors of $\mathbf{G}\mathbf{G}^T$ and $\mathbf{G}^T\mathbf{G}$, respectively [13]. Using (7), the MNLS solution to (5) is then given by

$$\mathbf{h}_{\text{MNLS}} = \sum_{i=1}^r \frac{\mathbf{u}_i^T \mathbf{f}}{\sigma_i} \mathbf{v}_i. \quad (8)$$

Note that, if \mathbf{G} is full rank, the MNLS is equivalent to the LS solution in the overdetermined case and to the MN solution in the underdetermined case. For example, for $M < N$ (underdetermined), $\mathbf{h}_{\text{MNLS}} = \mathbf{h}_{\text{MN}} = \mathbf{G}^T(\mathbf{G}\mathbf{G}^T)^{-1}\mathbf{f}$.

B. Regularization

The SVD of \mathbf{G} forms a basis for regularization by appropriate selection of singular modes that enhance the reconstructed image in some sense. There are a number of approaches for regularization of (8), including single parameter and rank reduction regularization [14]. The latter, sometimes referred to as the truncated singular value decomposition (TSVD), produces a solution by truncating the number of singular modes of \mathbf{G} with the smallest singular values below a certain threshold. The k th order TSVD solution is given by

$$\mathbf{h}_k = \sum_{i=1}^k \frac{\mathbf{u}_i^T \mathbf{f}}{\sigma_i} \mathbf{v}_i, \quad (9)$$

where the truncation parameter $k \leq r$, also known as the rank of the approximation, is the number of singular modes used to compute the estimate.

The regularization is guided by the mean square error criterion, approximated by

$$\hat{E}(k) = 10 \log_{10} \left(\frac{\|\mathbf{f} - \mathbf{G}\mathbf{h}_k\|^2}{M} \right), \quad (10)$$

where $\|\cdot\|^2$ is the l_2 norm.

In the context of the linear and quadratic prediction approach taken in this paper, the MSE decreases monotonically with k . A criterion for choosing an appropriate value of k is needed. In the context of contrast-agent imaging, an obvious criterion is the contrast-to-tissue ratio (CTR)

$$\text{CTR} = 10 \log_{10} \left(\frac{\bar{P}_C}{\bar{P}_T} \right), \quad (11)$$

where \bar{P}_C is the average power of signals in a UCA region, and \bar{P}_T is the average power of signals in a tissue region. The average power of signals in a given region, \bar{P} , can be expressed as

$$\bar{P} = \frac{1}{IJ} \left(\sum_{i=1}^I \sum_{j=1}^J x_{ij}^2 \right), \quad (12)$$

where x_{ij} is the signal in that region. Note that the CTR used in this algorithm is determined from quadratic components of the SVF model. The CTR provides a meaningful stopping criterion for TSVD since $\hat{E}(k)$ is monotonically decreasing or nonincreasing with k .

One may use a variety of methods to obtain a regularized solution to the set of equations involving the Volterra kernels. Examples are linear or nonlinear programming in cases when certain constraints on the filter coefficients are known to apply (e.g., positivity) or penalized maximum likelihood when known statistical properties of the data can be incorporated. A powerful approach seeks a solution to a constrained optimization problem of the form

$$\min_{\mathbf{h}_Q} R^2 \quad \text{subject to} \quad \mathbf{G}\mathbf{h} = \mathbf{f}, \quad (13)$$

where R^2 is an appropriately chosen quadratic ratio to be minimized (e.g., inverse of CTR). For example, R^2 can be chosen to reflect the inverse of the CTR before log compression. In general, it can be any quantity that depends on the solution \mathbf{h}_Q that is to be minimized. This leads to a modified form of the TSVD given here

$$\mathbf{h}_k = \sum_{i=1}^k \frac{\sigma_i}{\sigma_i^2 + \gamma R_i^2} \mathbf{u}_i^T \mathbf{f} \mathbf{v}_i, \quad (14)$$

where γ is an appropriately chosen threshold, and R_i^2 is quadratic ratio resulting from the quadratic kernel obtained from the i th singular mode. Regardless of the regularization procedure, the fundamental result here is the use of the linear/quadratic prediction to obtain a set of independent equations that can be solved robustly to obtain the Volterra filter kernels.

C. Quadratic Images

Quadratic images are obtained from quadratic components of the second-order Volterra model. The coefficients of the SVF are derived from the beamformed RF data taken from a representative region on a standard B-mode image. Details of the algorithm to produce the quadratic image are as follows.

From the standard B-mode image, a UCA region and a tissue region are defined for the CTR computation. The definition of the CTR reference regions depends on the imaging target are described in Section III-C. In general, we try to find regions at the same depth and with the same beam angle with respect to the axis of the imaging array. Furthermore, whenever possible, we chose multiple overlapping subregions to obtain multiple CTR values at different depths.

Once the CTR reference regions are defined, a segment of RF data from an axial line is selected to form a system of linear equations according to (4). This segment can be selected from the tissue or the UCA region as long as the appropriate regularization of the MNLS solution is sought. For example, when TSVD is used for regularization, CTRs of quadratic signals calculated from various orders of TSVD solutions are collected. With a defined range of system orders, a CTR plane as a function of truncation parameters and system orders is determined. Filter coefficients for the quadratic imaging generation are obtained from a truncation parameter and a system order that give the highest CTR value in the CTR plane. Of course, the TSVD approach can be used to obtain the coefficients of the quadratic kernel, $h_Q(i, j)$, for a predetermined filter order m . This may be necessary from the implementation point of view, when the size of the kernel is to be kept at manageable level. The results presented in this paper are obtained with low-order filter to emphasize the practicality of the Volterra filter approach.

The quadratic image is produced by applying the quadratic filter coefficients to the beamformed RF data

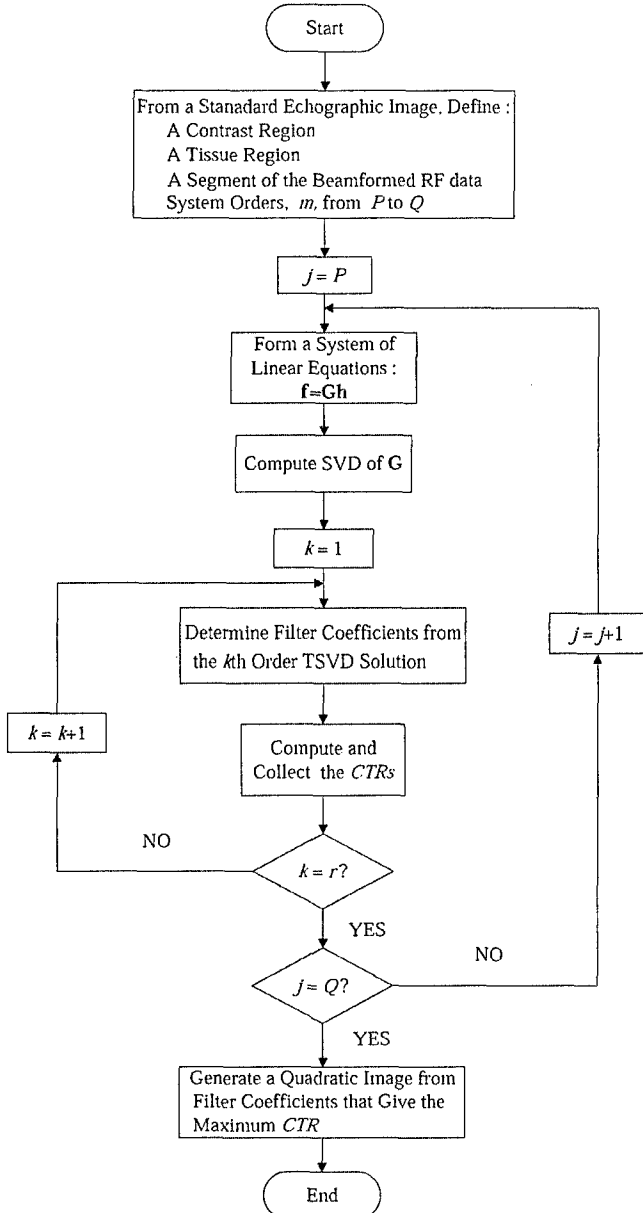


Fig. 2. A flowchart of the algorithm for quadratic image generation.

throughout the standard B-mode image to estimate the quadratic component

$$\hat{u}_Q(n+1) = \sum_{j=0}^{m-1} \sum_{k=j}^{m-1} u(n-j)u(n-k)\hat{h}_Q(j, k), \quad (15)$$

where $\hat{h}_Q(j, k)$ is the estimated quadratic kernel (extracted from \mathbf{h}_{MNLS}). A flowchart of this algorithm is shown in Fig. 2.

D. Harmonic Imaging

Second harmonic imaging is based on filtering the RF data with a zero-phase linear BPF centered at twice the fundamental with restricted bandwidth to minimize the

overlap between the fundamental and the second harmonic. The approach is appropriate for native harmonic imaging. However, when imaging UCA, the echo data from the UCA regions tends to have wider bandwidth when compared with echoes from tissue regions. Therefore, to obtain the highest possible contrast with a linear harmonic filter, we varied both the center frequency and the bandwidth of the filter and computed a CTR plane as a function of these parameters. This approach produced superior results compared to standard SH imaging. Harmonic imaging results shown in Section IV are obtained with the optimal linear BPF designed using the Parks-McClellan algorithm [18]. All linear filters used in this paper were implemented in a zero-phase realization ($y(n) = h(n) * h(-n) * x(n)$ or $Y(f) = |H(f)|^2 X(f)$). The order of the filter was chosen to achieve 50 dB stopband attenuation and 0.5 passband ripple.

III. MATERIALS AND METHODS

Imaging results shown below demonstrate the contrast enhancement achieved by the postbeamforming SVF in the context of contrast-agent imaging in tissue-mimicking media. Two imaging targets with two imaging probes are used to demonstrate generality and robustness of the approach.

A. Contrast Agent

The contrast agent, BR14 (Bracco Research S.A., Geneva, Switzerland), was used. The BR14 is a new experimental agent that consists of high molecular weight gas bubbles encapsulated by a flexible phospholipid shell. A 0.125 mL sample of BR14, prepared with 5 mL of 0.9% saline, was diluted in 500 mL of 0.9% saline leading to a 1:4000 dilution. In addition to BR14, cellulose particles (Sigma Cell Type 20, Sigma Chemical Co., St. Louis, MO) were used as linear scatterers in the flow channel target described below.

B. Imaging Targets

Images of two targets from two experimental setups were used to evaluate the performance of the quadratic imaging technique. The first experimental setup is shown in Fig. 3. The target is the L-shaped tissue-mimicking phantom in a beaker containing a dilution of BR14. The BR14 was constantly stirred by a magnetic stirrer. A MEGAS scanner (ESAOTE S.p.A., Genova, Italy) equipped with a 2-MHz phased array probe was used for image acquisition. The RF data acquisition was performed with 15-bit resolution at 40-MHz sampling frequency and without time gain control (TGC). This experiment allowed us to compare echoes from three different locations: the L-shaped tissue-mimicking phantom, the BR14, and the echo-free region visible in the scan. The significance of the latter is that any signal components observed in this region

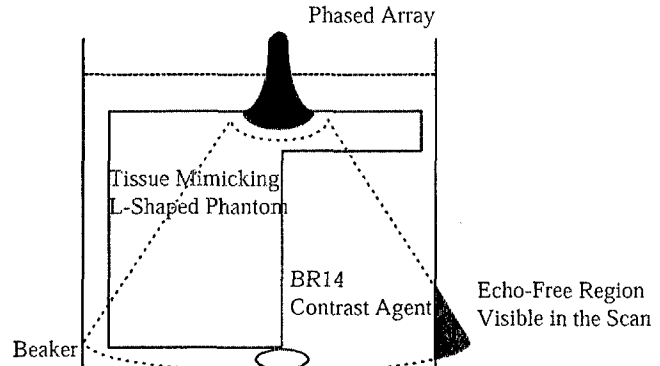


Fig. 3. Schematic for the imaging setup for the L-shaped phantom surrounded by the UCA.

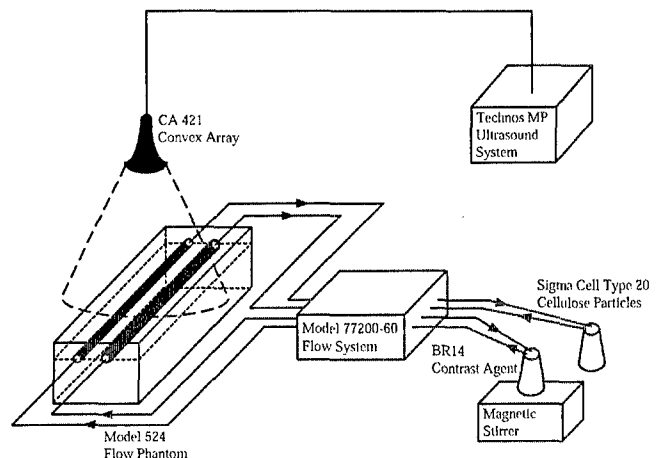


Fig. 4. The imaging setup for the flow phantom.

are largely artifacts from beamforming and/or reverberation. It should be noted, however, that there may be a small backscatter component present due to the beam reflections at the beaker, but this is hard to quantify in the presence of the contrast agent. Despite this limitation, it is interesting to compare the nature of the image pixels in this region from the three imaging methods.

The second experimental setup, shown in Fig. 4, was used in obtaining images of a flow phantom (Model 524; ATS Laboratories, Inc., Bridgeport, CT) containing four flow channels with diameters 2, 4, 6, and 8 mm embedded in rubber-based tissue mimicking material. The flow phantom was connected to a flow system with a roller pump (Model 77200-60; Cole-Parmer Instrument Co., Vernon Hills, IL). Subsequently, the diluted BR14 and cellulose particles were circulated. In addition, the diluted BR14 was constantly stirred in a beaker using a magnetic hot plate stirrer (EW-84303-20; Corning Inc., Corning, NY).

This experiment was designed to compare linear backscattered signals from cellulose in the 8-mm diameter flow channel with nonlinear backscattered signals from BR14 in the 6-mm diameter flow channel. The RF data were recorded and saved for later processing by the Tech-

nos MP ultrasound system (ESAOTE S.p.A., Genova, Italy) with a convex array probe (CA421; ESAOTE S.p.A., Genova, Italy) located perpendicularly to both the UCA and the cellulose flow channels. The RF data were acquired with 16-bit resolution at 20-MHz sampling frequency and without TGC. A 3-cycle pulse at 3.13 MHz was transmitted to produce standard B-mode images.

C. Quantitative Analysis

After the RF data corresponding to standard B-mode images were collected from experimental setups described above, quadratic images were obtained using the algorithm described in Section II-C. For comparison, harmonic images were produced by filtering the standard B-mode image with bandpass filters with center frequencies and fractional bandwidths chosen to maximize the CTR (defined by (11)) as described in Section II-D.

1. CTR Computations: The CTR was used for comparison between the image data in the RF domain before scan conversion as described in (11). Size and location of reference regions for each target are as follows. For the L-shape phantom, 45-mm axial segments of 20 adjacent A-lines on the tissue side and the same number on the contrast side were used. This phantom provided an excellent opportunity to compute CTR at multiple regions in the contrast and tissue regions with the same depth and the same beam angle from the axis of the imaging array. The calculation region extends by 45 mm in the axial direction (from 50 mm to 95 mm) and comprises 20 adjacent A-lines of RF data before scan conversion. The CTR values are calculated from cells with 3.8-mm axial extent with 10 connected A-lines and 50% overlap in both directions. For the flow phantom, one contrast region is in UCA flow channel and the tissue region located between two flow channels with the same axial extent (3 mm in this case). Twenty A-line segments from the each region were used.

2. Contrast Ratio: As can be seen from results given below, the dynamic range (in decibels) of images from quadratic components is approximately twice the dynamic range of standard B-mode and SH images. In order to account for image perception on standard 8-bit display, all images are represented with their full dynamic range mapped to 256 gray levels. That is,

$$I = \left(\frac{A - A_{\min}}{A_{\max} - A_{\min}} \right) \times 255, \quad (16)$$

where A is the log magnitude pixel values, given by

$$A = 20 \log_{10} \left\{ \left| \left[\frac{\mathcal{H}(x)}{x_{\text{ref}}} \right] \right| \right\}, \quad (17)$$

where $\mathcal{H}(x)$ denotes the Hilbert transform of data vector, x , and $x_{\text{ref}}(> 0)$ is some constant (typically maximum amplitude). The data vector is the digitized RF for standard

B-mode and the output of the harmonic or the quadratic filter for the harmonic and quadratic images, respectively.

A_{\min} and A_{\max} are minimum and maximum values, respectively. Both A_{\min} and A_{\max} are carefully computed so that histograms of images cover 256 gray levels without saturation. This was achieved by finding the average of the minima (maxima) of all image lines after median filtering. This was done to ensure that the display range is not set by extreme values of A_{\min} or A_{\max} .

From gray-level images, the contrast ratio (CR) [15] used as the contrast measurement between any two regions is given by

$$\text{CR} = \frac{|I_1 - I_2|}{\sqrt{\sigma_1^2 + \sigma_2^2}}, \quad (18)$$

where I_1 and I_2 are the average of gray levels, and σ_1 and σ_2 are the corresponding standard deviations in the first region and the second region, respectively.

3. Histogram and Receiver Operating Characteristic Analysis: In the imaging results shown below, we evaluate the CTR and CR based on regions in the image representative of the UCA and tissue regions with the same number of pixels and at the same depth. When the number of pixels in these regions is sufficiently high to produce meaningful statistics, histograms of the pixel data are produced to demonstrate these statistics. In addition, receiver operating characteristics (ROC) analysis [16] is performed as a simple method for classification of the different regions. In addition, when additional regions can be identified (e.g., low-scattering regions) in any image, the CR between tissue and such regions is also evaluated. Please note that the ROC curves are included in this paper to further quantify the degree of overlap between different histograms from tissue, contrast, and low-scattering regions.

D. Resolution Measurements

We used correlation lengths calculated from the 2D autocorrelation of echoes in tissue regions as described in [17] to measure spatial resolution. Intensity images are scan converted and uniform speckle regions were identified to compute the average speckle correlation cell size

$$S_C = \int_{-X}^X \int_{-Y}^Y \frac{C_I(x, y)}{C_I(0, 0)} dx dy, \quad (19)$$

where $C_I(x, y)$ is the 2D correlation function of the intensity autocovariance function, and X and Y are taken to be sufficiently large to allow the magnitude of the autocovariance to drop to negligible levels. The vertical and horizontal correlation cell sizes, representing the axial and lateral resolution, respectively, were used to compare spatial resolution for the three imaging techniques.

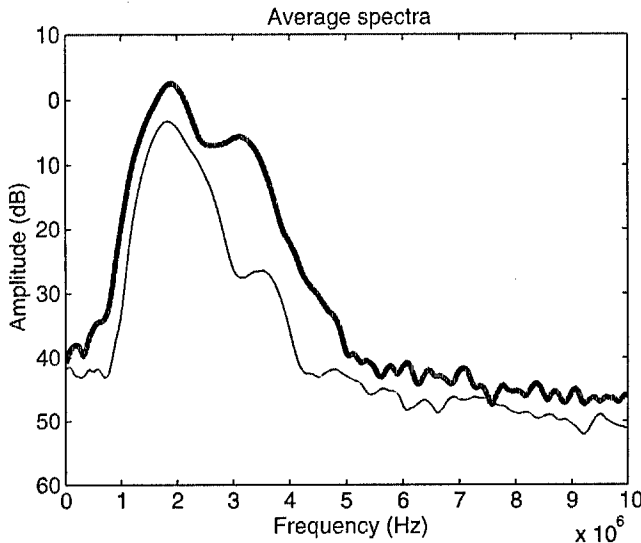


Fig. 5. Average spectra from the contrast (thick) and tissue (thin) regions of the L-shaped phantom.

IV. RESULTS

A. L-Shaped Phantom

Fig. 5 shows the average spectra of typical echoes from the contrast and tissue regions of the L-shaped phantom. The average spectra were calculated by averaging windowed periodogram of every echo line in regions described in Section III-C.1. These spectra suggest that echoes from the contrast region have broader bandwidth compared to the echoes from tissue-like region. As mentioned in Section II-D, this suggests that the best linear filter for contrast enhancement may not be the standard SH filter. Rather, a general BPF with center frequency and relative bandwidth designed to maximize the CTR may be sought. Based on this approach, we have designed a zero-phase BPF with center frequency of 3.2 MHz and relative bandwidth of 30% to demonstrate the performance of linear postbeamforming harmonic imaging. The quadratic filter was derived from echoes from the tissue region according to the algorithm described in Section II-C (with $P = Q = 10$ in Fig. 2). Panels (a), (b), and (c) of Fig. 6 show images obtained using standard B-mode, linear BPF, and quadratic imaging methods, respectively. Due to differences in dynamic ranges for the three methods, each image is displayed with its full dynamic range as can be seen from the decibel-level scale bars shown in accordance with (16). Fig. 6(d) shows four rectangular regions used for characterization of the imaging results. Regions A_1 and A_2 are representative of tissue and contrast echoes, respectively. Regions B_1 and B_2 are representative of tissue and echo-free region, respectively. These regions are used for CTR calculations as well as evaluating histograms of the reconstructed images. Due to the structure of the target, regions B_1 and B_2 could not be placed at the same depth in the image. Nevertheless, region B_1 is representative of tissue re-

sponse and provides a valid baseline for comparison of contrast with the echo-free region, B_2 . The standard B-mode image (Fig. 6(a)) was obtained from the digitized RF echo data and displayed with a dynamic range of 60 dB. The structure of the L-shaped phantom can be recognized with low contrast between the UCA and the tissue-mimicking regions. The strong specular reflection at the top of the UCA region is due to a boundary layer formed by the agent at the interface with the tissue-mimicking medium. A careful examination of the image reveals a higher level of contrast between the two regions at close range. A CTR value of 6.65 dB was computed based on echo signals from regions A_2 and A_1 (Fig. 6(d)).

The linear harmonic BPF image shown in Fig. 6(b) was produced by filtering the RF data with bandpass filter centered around the second harmonic (3.2 MHz) with a fractional bandwidth of 30%. The center frequency and the fractional bandwidth of the harmonic filter were chosen to optimize the CTR value for regions A_1 and A_2 in Fig. 6(d). The CTR value for the harmonic image (18.2 dB) is consistent with the perceived enhancement clearly visible in the image. One can also observe the loss of the specular reflections at the top right and bottom left of the harmonic image. This is typical since these echoes have significant low frequency components. As expected, the speckle in the tissue region appears finer than that of the standard B-mode.

The quadratic image obtained using the algorithm described in Section II-C is shown in Fig. 6(c). The CTR for this image is 21.3 dB indicating contrast enhancement over both standard B-mode and harmonic images. One important feature of the quadratic image is the increased dynamic range compared with B-mode and harmonic images. This increased dynamic range results in contrast enhancement without loss in image features, such as specular reflections, which may be of diagnostic value in some cases.

Another interesting comparison among the three image results shown in Fig. 6(a)–(c) is the echo-free region visible at the right edge of the scan. One can see that contrast between tissue and this region in the quadratic image is superior to that from the B-mode image, whereas this contrast in the harmonic image is the lowest. This result is significant because echo signals from this region are largely artifacts (due to beamforming and/or reverberations). Quantitative measures of this contrast enhancement between the tissue and echo-free regions are given below.

To further illustrate the imaging results given in Fig. 6, vertical and horizontal lines through images are plotted in Fig. 7. Axial lines from the three imaging techniques through the UCA region are shown in Fig. 7(a). One can see that the specular reflector is all but eliminated in the harmonic image, while it remains visible for the other two methods. Further, the axial line from the quadratic image shows no apparent loss in the axial resolution at the specular reflection location. Lateral lines at the 90-mm depth from the three imaging techniques are shown in Fig. 7(b). These lateral lines pass through the UCA, tissue, and the

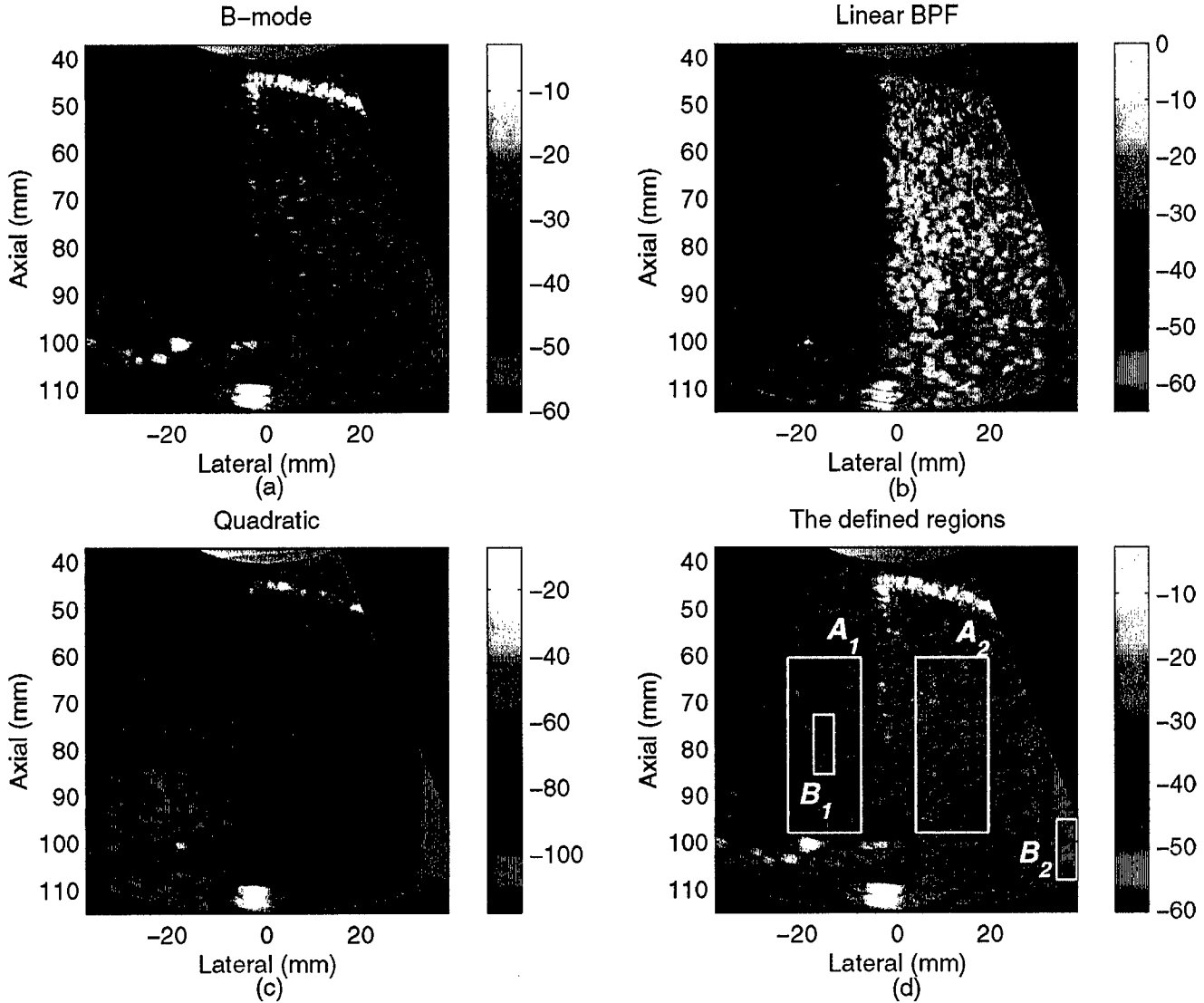


Fig. 6. Images of the beaker containing the tissue-mimicking L-shaped phantom surrounded by the UCA from three imaging techniques. (a) Standard B-mode. (b) Linear harmonic BPF. (c) Quadratic. (d) Boxes indicate regions for CTR and histogram calculations.

echo-free regions. One can see the contrast enhancement from the lateral line of the harmonic image compared with the lateral line of the standard B-mode image. Most significantly, however, one can see that the quadratic image provides the maximum separation between the three regions without apparent loss of lateral resolution. This was confirmed by computing the correlation cell size in the scan-converted intensity images according to (19) [17] from the three imaging methods in the tissue region (59 to 73 mm axial and -20 to -14 mm lateral in Fig. 6). These values are reported in Table I.

B. Flow Channel Phantom

Fig. 8 shows the average spectra of typical echoes from the contrast and tissue regions of the flow phantom described in Section III-B. The average spectra are calculated by averaging windowed periodogram of every echo

line in regions described in Section III-C.1. As with the L-shaped phantom result, the echoes from the UCA region exhibit broader bandwidth than those from tissue region. The standard B-mode image of the flow phantom consisting of the UCA and cellulose in flow channels was acquired using the experimental setup described in Section III-B. The image is shown in Fig. 9(a). One can see the backscattered enhancement due to the UCA in the 6-mm flow channel (55- to 61-mm axial and -6 to 0 mm lateral) compared with the surrounding tissue with CTR 9.8 dB. The CTR was calculated based on echo signals from the 6-mm flow channel excluding the specular reflectors (Box C₁) and echoes from tissue at the same depth (Box C₂). On the other hand, the echoes from the cellulose in the 8-mm flow channel (53 to 61 mm axial and 17 to 25 mm lateral) are weaker than those from the surrounding tissue. A linear scatterer-to-tissue ratio (LTR) was calculated based on echo signals from the 8-mm flow channel

TABLE I

CR, CTR, AND CORRELATION CELL SIZE VALUES FOR THE L-SHAPED IMAGING TARGET. THE CTR VALUES ARE GIVEN AS MEAN IN DECIBELS WITH STANDARD DEVIATION IN PARENTHESES.

Imaging method	UCA/T-Mimic	T-Mimic/E-F	CTR	S_z	S_x
B-mode	0.94	1.51	6.65 (1.3)	1.2	2.3
SH	2.56	1.12	18.2 (1.6)	1.0	1.6
Quadratic	2.16	1.66	21.3 (1.9)	0.42	0.8

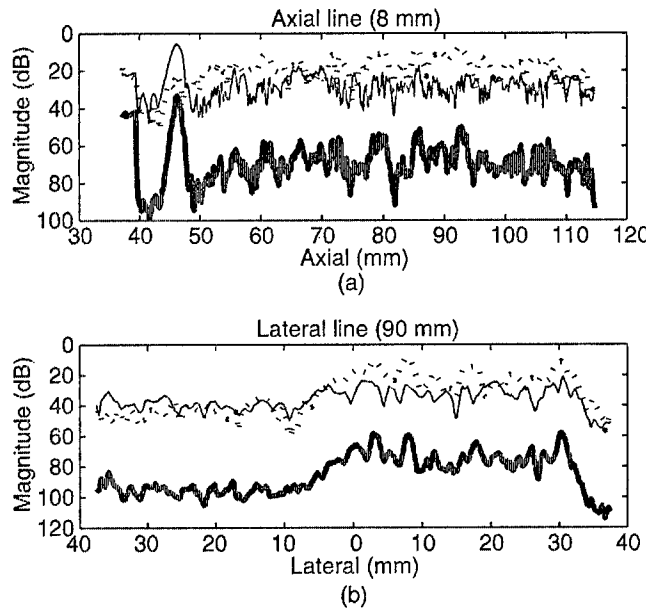


Fig. 7. Lines through images in Fig. 6 from three imaging techniques. Thin: B-mode. Dash: Harmonic. Thick: Quadratic. (Top) Axial lines through the UCA region. (Bottom) Lateral lines (at depth 90 mm) through the tissue-mimicking, UCA, and echo-free regions.

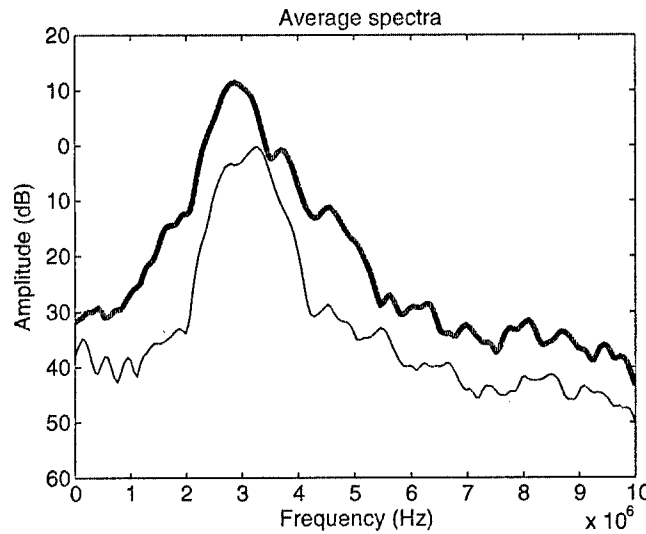


Fig. 8. Average spectra from the contrast (thick) and tissue (thin) regions of the flow phantom.

(Box C_3) and echoes from tissue at the same depth (Box C_2). The LTR was -8.8 dB, calculated based on (11) for 8-mm channel.

The harmonic image shown in Fig. 9(b) was produced by filtering the RF data with bandpass filter centered around 4.8 MHz with a fractional bandwidth of 30%. The center frequency and the fractional bandwidth of the harmonic filter were chosen to optimize the CTR value using the method described in Section II-D for the UCA and tissue regions shown in Fig. 9(d). The CTR value for the harmonic image is 15 dB, which is consistent with the perceived enhancement clearly visible in the displayed image. It is interesting to note the loss of the specular reflections from the contrast flow channel but not from the linear scatterer channel. It is also interesting to note that the speckle in the tissue region is finer than that of the standard B-mode. This indicates that the optimization of the harmonic filter resulted in a larger fractional bandwidth than that of the fundamental component. The LTR for the harmonic component is now -7.6 dB. That is, the harmonic image does not preserve the low-scattering region as it improves the contrast between the UCA and tissue regions.

Fig. 9(c) shows the quadratic image obtained using the algorithm described in Section II-C (with $P = Q = 12$ in Fig. 2). Compared with the standard B-mode, the enhanced visualization of the UCA in the small flow channel surrounded by the tissue can be seen. This enhanced visualization is also consistent with the higher CTR (22.2 dB). In addition, one can see the reduction in the echogenicity of the cellulose in the 8-mm flow channel. This is also reflected in the value of LTR (-15.4 dB) computed for this channel. This result demonstrates the ability of the quadratic filter to separate the tissue from both the UCA and the low-scattering cellulose region simultaneously. We can also see the preservation of specular reflections from both the UCA and cellulose flow channels. This can be seen more quantitatively in Fig. 10, which shows the decibel values for axial and lateral lines through images in Fig. 9. Axial lines through the center of the cellulose and the UCA flow channels are shown in Fig. 10(a) and Fig. 10(b), respectively. Lateral lines through the center of both the cellulose and the UCA flow channels are shown in Fig. 10(c). One can see the contrast enhancement in different media (i.e., the UCA, the cellulose, and the tissue) from the quadratic image without loss in spatial resolution. In particular, for the B-mode image, the signal from the contrast channel is 13 dB above the tissue level and 30 dB above the cellulose channel. On the other hand, for the quadratic

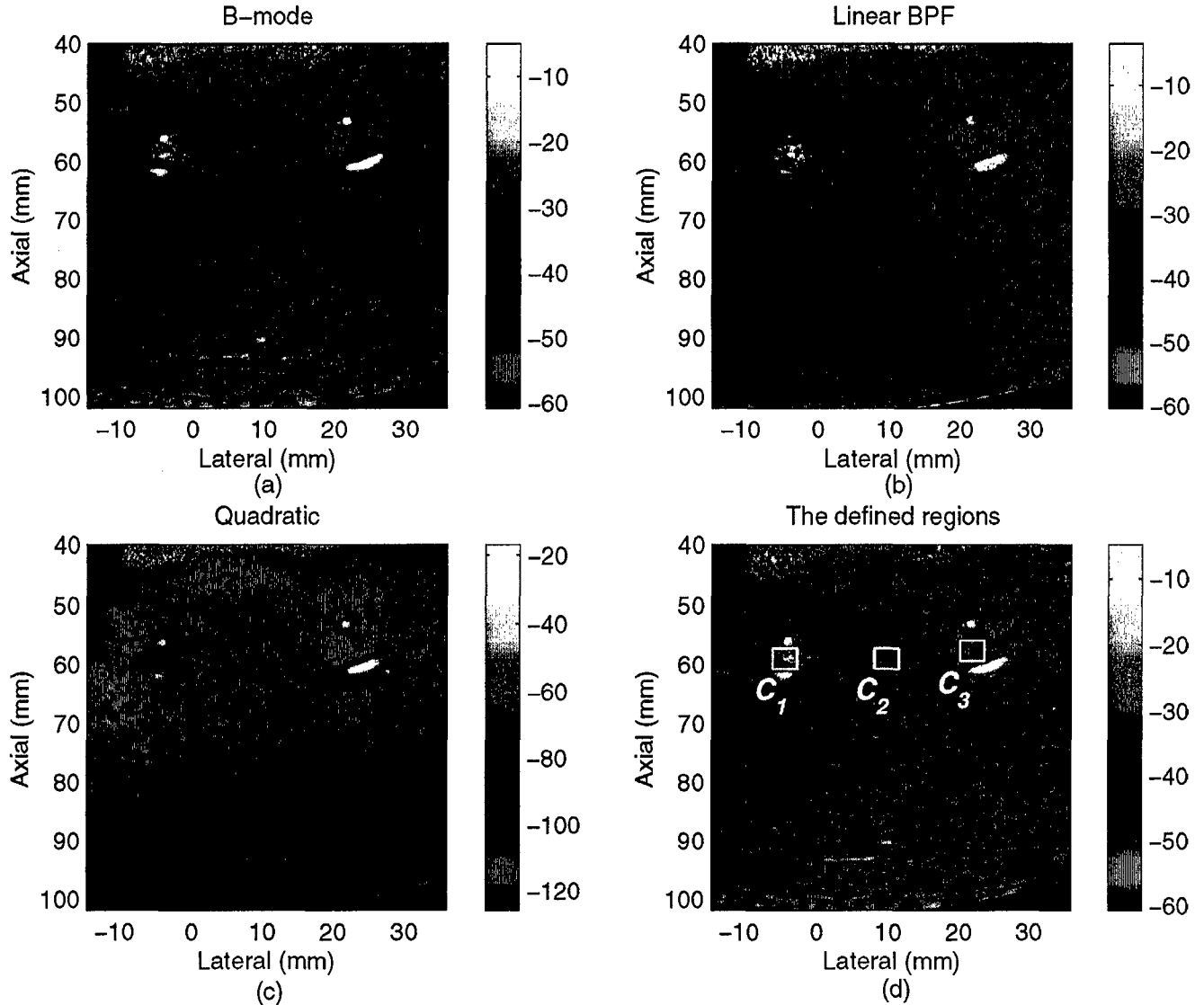


Fig. 9. Images of the flow phantom using (a) Standard B-mode. (b) Harmonic. (c) Quadratic. (d) Boxes C_1 , C_2 , and C_3 indicate regions for CTR and CR calculations. Note the hyperechoic region from the UCA in the 6-mm flow channel (55 mm to 61 mm axial and -6 mm to 0 lateral) and the hypoechoic region from the cellulose (53 mm to 61 mm axial and 17 mm to 25 mm lateral).

image, the signal from the contrast channel is 30 dB higher than tissue and 67 dB higher than the cellulose channel. Finally, examination of the strong specular reflections along the axial lines shown in Fig. 10 suggests that the quadratic filter preserves the resolution of the system. This was confirmed by computing the correlation cell size in the scan-converted intensity images according to (19) [17] from the three imaging methods in the tissue region (52 to 65 mm axial and 4 to 17 mm lateral in Fig. 9). These values are reported in Table II.

C. Classification Results

To give the reader a quantitative idea of the ability of the three different imaging methods to separate the different regions in the imaging targets, we use histograms from representative areas of these regions. For example,

for the tissue-mimicking L-shaped phantom surrounded by the UCA in the beaker, regions from different media are defined in Fig. 6(d) as follows: the region A1 and A2 (the tissue and UCA regions, respectively) and the region B1 and B2 (the tissue and echo-free regions, respectively). After images from three different imaging techniques are scan converted and represented with 256 levels of gray covering their full dynamic range, the histogram of each region is determined and shown in Fig. 11. Histograms from regions A1 and A2 are shown in Fig. 11 (left-hand side). One can see the degree of overlap between the histograms is highest for the standard B-mode image. On the other hand, the corresponding histograms are well separated for the harmonic and quadratic images. This is consistent with the increased level of contrast perceived from direct visualization of the images in Fig. 6. Histograms produced from regions B1 and B2 are shown in

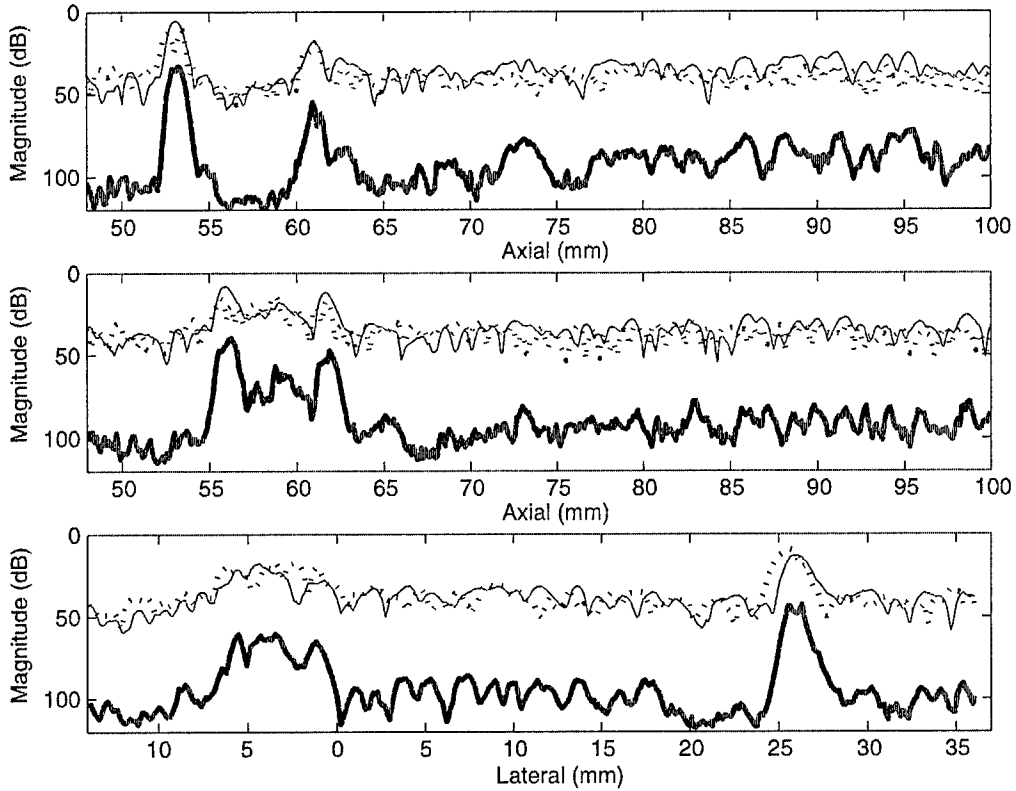


Fig. 10. Lines through the standard B-mode (thin), harmonic (dashed), and the quadratic (thick) from images shown in Fig. 9. (Top) Axial lines through the center of the cellulose flow channel. (Middle) Axial lines through the center of the UCA flow channel. (Bottom) Lateral lines through the center of both two flow channels.

TABLE II
CR, CTR, AND CORRELATION CELL SIZE VALUES FOR THE FLOW CHANNEL TARGET. THE CTR VALUES ARE GIVEN IN DECIBELS.

Imaging method	UCA/Tissue	Tissue/Cellulose	CTR	S_z	S_x
B-mode	1.57	1.35	9.8	1.0	1.2
SH	2.12	1.21	15.0	0.6	0.9
Quadratic	2.46	1.65	22.2	0.9	1.1

Fig. 11 (right-hand side). Gray-level histograms of regions B1 and B2 produced from harmonic image has higher degree of overlap than those from the standard B-mode and the quadratic images. This is further quantified by ROC curves [16] obtained from histograms of region A1 (Tissue) and A2 (UCA) and region B1 (tissue) and B2 (echo-free) are shown in Fig. 12(a) and Fig. 12(b), respectively. As can be seen in Fig. 12(a), the A_z values between region A1 and A2 from the standard B-mode, harmonic and quadratic images are 0.8269, 0.9936, and 0.9876, respectively. These values demonstrate improved classification performance between region A1 and region A2 from harmonic and quadratic images over the standard B-mode image. However, as shown in Fig. 12(b), the A_z value of the quadratic image (0.9535) presents the best classification performance of tissue and echo-free regions among three imaging techniques, while the classification performance from the harmonic image ($A_z = 0.8724$) is inferior to that

from the standard B-mode image ($A_z = 0.9302$). These measurements show that the quadratic image provides improved separation of the UCA from the tissue mimic comparable with SH performance. At the same time, significant improvement in separation between tissue mimic and echo-free regions is achievable in the quadratic image over both the standard B-mode and SH images.

Contrast ratios determined from corresponding gray scale images in Fig. 6 are shown in Table I. For contrast comparison between the UCA and tissue regions, CRs obtained from regions A1 and A2 demonstrate the contrast enhancement of the harmonic (2.56) and the quadratic (2.16) images over the standard B-mode image (0.94). On the other hand, one can see that the CR between tissue and echo-free regions of the harmonic image (1.12) is inferior to that of the standard B-mode image (1.51). However, the quadratic image gives the maximal CR (1.66). These CR values agree with both the visualization of images shown

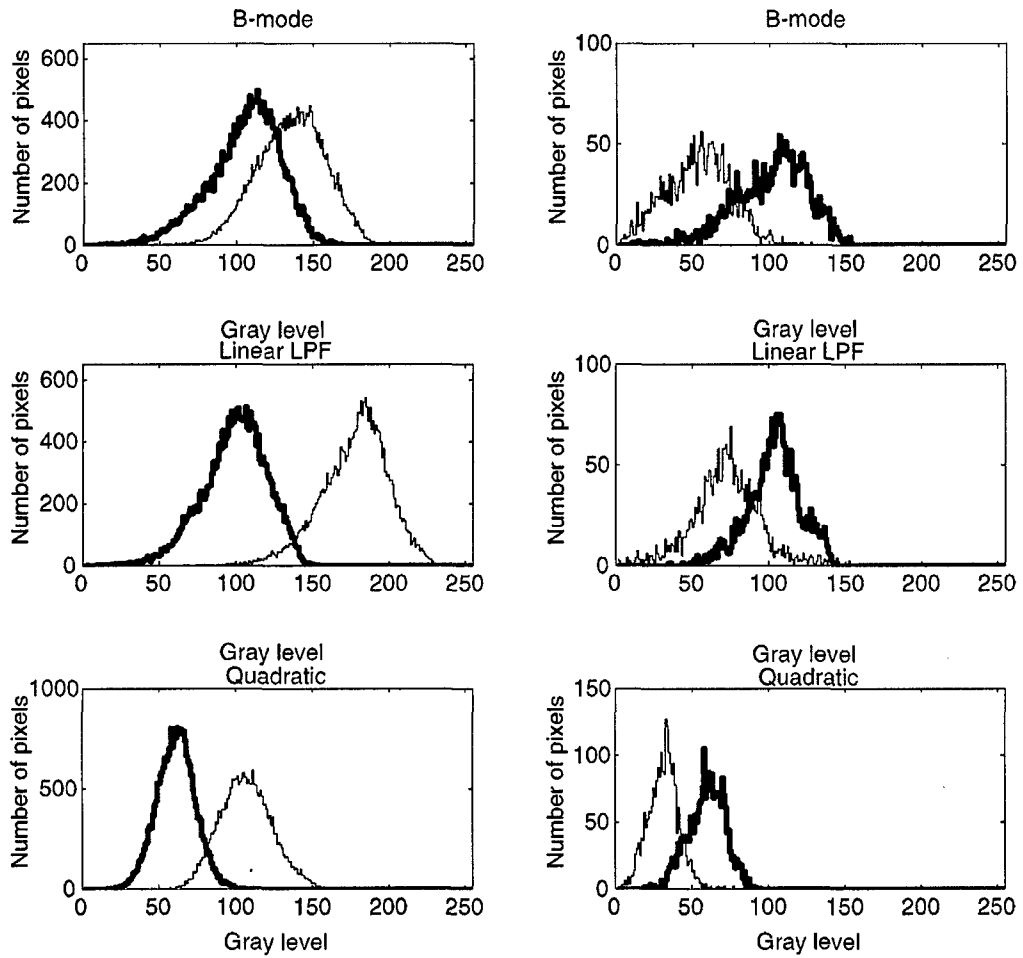


Fig. 11. Gray-level histograms produced from images shown in Fig. 6. Top: B-mode. Middle: Harmonic. Bottom: Quadratic. Histograms on the left-hand side are produced from region A1 and A2. Thick: Region A1 (Tissue). Thin: Region A2 (Contrast). Histograms on the right-hand side are produced from region B1 and B2. Thick: Region B1 (Tissue). Thin: Region B2 (Air).

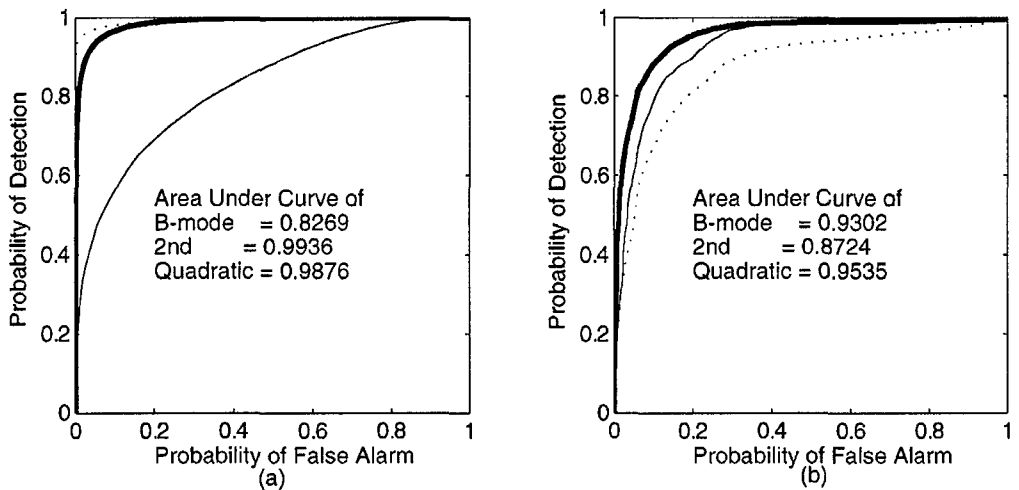


Fig. 12. The ROC curves produced from gray-level histograms in Fig. 11 of three imaging techniques. Thin: B-mode. Dash: Harmonic. Thick: Quadratic. The ROC curve obtained from the UCA and tissue regions is shown on the left-hand side. The ROC curve obtained from the echo-free and tissue regions is shown on the right-hand side.

in Fig. 6 and the degree of overlap between the histograms shown in Fig. 11. These results have demonstrated that the quadratic image provides the perceived contrast enhancement not only between the UCA and tissue regions but also between the tissue and the echo-free regions. We note here that similar analysis was performed for the flow channel data and that the results are in full agreement with the results shown in this section. The CR, CTR, and correlation cell size values for both the L-shaped and flow phantoms are summarized in Tables I and II.

Similarly, images of the UCA and cellulose flow channels in the flow phantom as shown in Fig. 9 are scaled into 8-bit gray-level images. Gray-level histograms between the UCA and tissue regions and between the cellulose and tissue regions are produced and the corresponding ROC curves are determined. Although the number of data from each region is quite small for meaningful statistical analysis, results from both CRs and A_z show tendency that the quadratic image enhances the contrast and provides better classification performance compared with the standard B-mode image. Table II gives the CR values resulting from the flow channel experiment.

V. DISCUSSION

We have introduced a nonlinear postbeamforming filtering algorithm for ultrasonic pulse-echo imaging based on the Volterra filter model. The main goal of this paper was to introduce the mathematical basis for deriving the filter coefficients from standard beamformed RF data obtained by commercial scanners. In addition, we have presented imaging results from two laboratory contrast targets to illustrate the nature of the gray scale images obtained with the quadratic component compared with standard echo signals and harmonic images. Images from the quadratic components were obtained by applying a single filter derived from echoes from the contrast region. We have decided to do this to demonstrate that the method is quite robust in the sense that the derived filter is applied throughout the image to produce images free of artificial inhomogeneity. This is a desirable method from the implementation point of view, especially for real-time implementation.

For a fair comparison, all images presented in this paper were normalized to their full dynamic range and displayed using 256 levels of gray. Classification results based on histogram characterization of contrast and tissue regions show that the quadratic images produce nearly twofold increase in CR values (compared with standard echo images) without loss of image features (compared to harmonic images). Classifying the tissue and echo-free regions demonstrated the improved performance with respect to harmonic imaging. This is probably due the vulnerability of harmonic images to noise and beamforming artifacts, especially when the sidelobes of the transmit beam are in contrast regions.

Even though we have focused on the comparison between gray-scale images, there are some interesting prop-

erties of the quadratic signal components that may reveal important information on the nature of the objects producing the echo signals. For example, the frequency component at f in the quadratic signal component is a result of all frequency components f_1 and f_2 from the echo signal such that $f_1 + f_2 = f$, weighted by $H_Q(f_1, f_2)$. This frequency coupling results in quadratic signal components with high SNR values due to rejection of additive noise. An interesting question is whether the quadratic components are more directly related to the composition of the echoes in terms of coherent and diffuse scattering. This may be quite significant in improving the robustness of motion tracking and displacement estimation algorithms.

In this paper, the filter is designed based on nonlinear echoes from the tissue-like medium. However, the filter does not distinguish between nonlinearities from UCA and those from tissue. The contrast enhancement is mainly due to the higher level of quadratic component (relative to the RF signal level) in the contrast regions. For example, in the L-shaped phantom, on average, the quadratic signal is 30 dB and 50 dB below the RF in the contrast and tissue regions, respectively. It is interesting to note that, for this target, the quadratic component from the magnetic bead at the bottom of the image is only 3 dB below the RF signal. This suggests that the quadratic filter does not completely reject quadratic echoes from specular reflectors, even though it may still discriminate against them. Therefore, for applications in which the quadratic components from the contrast agents are weak or comparable to tissue components, a method for separating the two types of nonlinearity is needed. There are several possible approaches to the filter design problem so that better separation between nonlinear echoes from UCA and tissue:

- Adaptive implementation of the SVF based on fast recursive LS approach [12]. This will allow for the optimization of filter coefficients based on the local level of nonlinearity.
- Higher order filters (e.g., cubic) that may be more sensitive to UCA nonlinearity than tissue nonlinearity. This is due to the observation that, under normal imaging conditions, tissue nonlinearity is at most quadratic.
- Synthesis of pulse sequences to excite contrast microbubbles to maximize their nonlinear response. This is motivated by the recent trend in contrast-agent imaging, which calls for the use of super low values of MI. The identified quadratic kernel of the SVF can be used for the design of these waveforms.

We have chosen to compare quadratic images with images obtained using linear harmonic filters rather than second harmonic filters. This was based on the observation that the spectra of echoes from contrast regions are typically broader than those from tissue regions as can be seen from Figs. 5 and 8. The application of a strict SH filter based on the bandwidth from tissue component typically produce inferior results when UCA regions are present in the imaging field. To illustrate this point, Fig. 13 shows

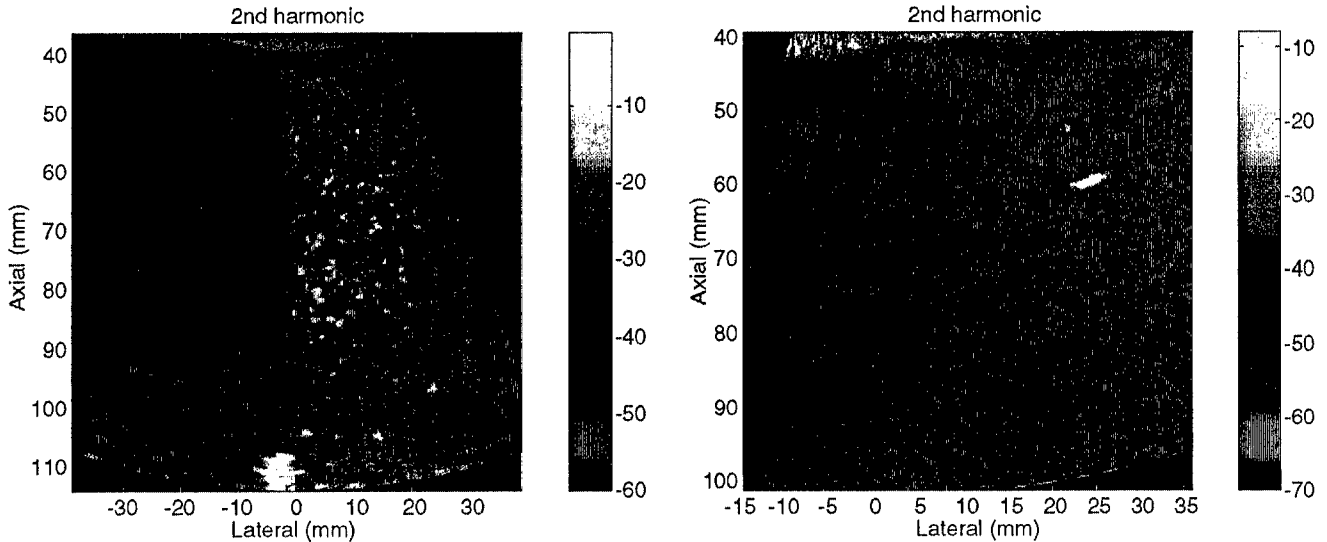


Fig. 13. LHS: The image of L-shaped phantom produced using BPF centered at 4 MHz with fractional bandwidth 25%. RHS: The image of flow channel phantom produced using BPF centered at 6 MHz with fractional bandwidth 25%.

SH images of both the L-shaped and flow phantoms based on the spectra from tissue regions. These images are visibly inferior to those obtained using the linear harmonic approach described in Section II-D. We note that quantitative analysis of these images confirms the inferiority of the SH images shown.

The filters used for extracting the quadratic components for the two data sets were of orders 10 and 12 for the L-shaped phantom and the flow-channel phantom, respectively. In deriving the filters, we have assumed that $h_Q(j, k) = h_Q(k, j)$, which implies that the filters can be implemented with 65 and 90 independent coefficients, respectively. On the other hand, the linear bandpass filter had 77 coefficients. This number is effectively doubled by the zero-phase implementation described in Section II-D. While it is not our objective to compare the computational efficiency of the quadratic filters with the linear filter, we note that the requirements of the quadratic filters will not present a severe problem for real-time implementation on modern ultrasound scanners. We also note that efficient software and hardware implementations of the Volterra filter have been extensively studied in recent literature [19].

Finally, even though the two imaging targets in this paper contain UCA regions, quadratic images can be used in "native quadratic" form, in much the same way as SH images. The enhancement of the contrast between the tissue mimic and the low scattering regions in both targets offer an illustration of the nature of quadratic images in native mode. We are currently investigating speckle reduction in quadratic images (some speckle reduction can be observed in the tissue mimic in quadratic images from both phantoms). This is the subject of a future report.

VI. CONCLUSIONS

A nonlinear postbeamforming filter based on the Volterra model was introduced in this paper. The

quadratic component from the SVF signal separation model was shown to produce images with high contrast and high dynamic range without loss of axial or lateral resolution. This was confirmed by estimating the correlation cell size based on [17] for the quadratic images and comparing with those for B-mode and Harmonic images (Tables I and II). The improvement in contrast was confirmed by quantitative measures, both on the RF data and the log-compressed image data after scan conversion. Furthermore, the quadratic images were also shown to preserve the low-scattering targets while improving the UCA to tissue contrast. This was demonstrated by the computed CR values (Tables I and II) and the A_z values from the ROC curves shown in Fig. 12.

ACKNOWLEDGMENTS

We are indebted to Prof. Franco Bertora from Esaote for his help and support on all aspects of this research. We are also grateful for Dr. Paolo Pellegratti from Esaote for help with data acquisition and valuable suggestions. The RF data for the L-shaped phantom was provided by Dr. Marcel Arditi from Bracco Research. We are also thankful for Hui Yao for helping with the flow channel experimental setup.

REFERENCES

- [1] J. Ophir and K. J. Parker, "Contrast agent in diagnostic ultrasound," *Ultrasound Med. Biol.*, vol. 15, no. 4, pp. 319–333, Nov. 1989.
- [2] J. D. Kasprzak, B. Paolinck, F. J. Ten Cate, W. B. Vletter, N. de Jong, D. Poldermans, A. Elhendy, A. Bouakaz, and J. R. Roelandt, "Comparison of native and contrast-enhanced harmonic echocardiography for visualization of left ventricular endocardial border," *Amer. J. Cardiol.*, vol. 83, no. 2, pp. 211–217, 1999.

- [3] S. Kaul and R. Jayaweera, "Coronary and myocardium blood volumes: Noninvasive tools to assess the coronary microcirculation," *Circulation*, vol. 96, pp. 719-724, Aug. 1997.
- [4] P. J. A. Frinking, E. Cespedes, J. Kirkhorn, H. Torp, and N. de Jong, "A new contrast ultrasound imaging approach based on the combination of multiple imaging pulses and a separate release burst," *IEEE Trans. Ultrason., Ferroelect., Freq. Contr.*, vol. 48, no. 3, pp. 643-651, May 2001.
- [5] P. J. A. Frinking, A. Bouakaz, J. Kirkhorn, F. J. Ten Cate, and N. de Jong, "Ultrasound contrast imaging: Current and new potential methods," *Ultrasound Med. Biol.*, vol. 26, no. 6, pp. 965-975, 2000.
- [6] N. de Jong, P. J. A. Frinking, A. Bouakaz, and F. J. Ten Cate, "Detection procedures of ultrasound contrast agents," *Ultrasonics*, vol. 38, pp. 87-92, Mar. 2000.
- [7] D. H. Simpson, C. T. Chin, and P. N. Burns, "Pulse inversion Doppler: A new method for detecting nonlinear echoes from microbubble contrast agent," *IEEE Trans. Ultrason., Ferroelect., Freq. Contr.*, vol. 46, no. 2, pp. 372-382, Mar. 1999.
- [8] D. H. Simpson and C. T. Chin, "Perfusion imaging with pulse inversion Doppler and microbubble contrast agents: In vivo studies of the myocardium," in *Proc. IEEE Ultrason. Symp.*, 1998, vol. 2, pp. 1784-1786.
- [9] H. Yao, P. Phukpattaranont, and E. S. Ebbini, "Post-beamforming second-order Volterra filter for nonlinear pulse-echo imaging," in *Proc. Int. Conf. Acoust. Speech Signal Processing*, vol. 2, 2002, pp. 1133-1136.
- [10] K. I. Kim and E. J. Powers, "A digital method of modeling quadratically nonlinear systems with a general random input," *IEEE Trans. Acoust. Speech Signal Processing*, vol. ASSP-36, no. 11, pp. 1758-1769, Nov. 1988.
- [11] T. Koh and E. J. Powers, "Second-order Volterra filtering and its application to nonlinear system identification," *IEEE Trans. Acoust. Speech Signal Processing*, vol. ASSP-33, no. 6, pp. 1445-1455, Dec. 1985.
- [12] K. Kim, S. B. Kim, E. J. Powers, R. W. Miksad, and F. J. Fischer, "Adaptive second-order Volterra filtering and its application to second-order drift phenomena," *IEEE J. Oceanic Eng.*, vol. 19, no. 2, pp. 183-192, Apr. 1994.
- [13] G. H. Golub and C. F. Van Loan, *Matrix Computations*. 2nd ed. Baltimore, MD: Johns Hopkins Univ. Press, 1989, pp. 70-85.
- [14] J. Shen and E. S. Ebbini, "A new coded excitation ultrasound imaging system: Part I—Basic principles," *IEEE Trans. Ultrason., Ferroelect., Freq. Contr.*, vol. 43, no. 2, pp. 919-928, 1996.
- [15] W. K. Pratt, *Digital Image Processing*. 3rd ed. New York: Wiley, 2001, pp. 29-39.
- [16] C. E. Metz, "ROC methodology in radiologic imaging," *Investigative Radiol.*, vol. 21, no. 9, pp. 720-733, 1986.
- [17] R. F. Wagner, M. F. Insana, and S. W. Smith, "Fundamental correlation lengths of coherent speckle in medical ultrasonic images," *IEEE Trans. Ultrason., Ferroelect., Freq. Contr.*, vol. 35, no. 1, pp. 34-44, Jan. 1988.
- [18] S. K. Mitra, *Digital Signal Processing: A Computer-Based Approach*. 2nd ed. New York: McGraw-Hill, 2001, pp. 423-498.
- [19] V. J. Mathews and G. Sicuranza, *Polynomial Signal Processing*. New York: Wiley, 2000, pp. 380-410.



Pornchai Phukpattaranont was born in Songkla, Thailand, in 1970. He received his B. Eng. and M. Eng. degrees in Electrical Engineering from Prince of Songkla University in 1993 and 1997, respectively. His M. Eng. thesis was on the sequential electrical stimulator for dysphagia patients. He is currently working toward his Ph.D. degree in Electrical and Computer Engineering at the University of Minnesota. His research interests are ultrasound contrast imaging and ultrasound signal processing.



Emad S. Ebbini (S'84-M'85-S'86-M'89) received his B.Sc. in EE/communications in 1985 from the University of Jordan and the M.S. and Ph.D. degrees in EE from the University of Illinois at Urbana-Champaign in 1990. From 1990 until 1998, he was on the faculty of the EECS department at the University of Michigan, Ann Arbor. Since 1998, he has been with the ECE department at the University of Minnesota. In 1993, he received the NSF Young Investigator Award for his work on new ultrasound phased arrays for imaging and therapy. He was a member of AdCom for the IEEE Ultrasonics, Ferroelectrics, and Frequency Control between 1994 and 1997. In 1996, he was a guest editor for a special issue on therapeutic ultrasound in the *IEEE Transactions on Ultrasonics, Ferroelectrics, and Frequency Control*. He was an associate editor for the same transactions from 1997-2002. He is a member of the standing technical program committee for the IEEE Ultrasonics Symposium and a member of the Board of the International Society for Therapeutic Ultrasound. His research interests are in signal and array processing with applications to biomedical ultrasonics.

APPENDIX III

DETECTION AND MAPPING OF THERMAL LESIONS USING DUAL-MODE ULTRASOUND PHASED ARRAYS

Hui Yao, Pornchai Phukpattaranont, and Emad S. Ebbini

Department of Electrical and Computer Engineering
University of Minnesota
Minneapolis, MN 55455

ABSTRACT

It has long been recognized that thermal lesions formed using high-intensity focused ultrasound (HIFU) exhibit nonlinear behavior that can be detected in pulse-echo ultrasound. Second harmonic imaging of freshly formed thermal lesions have consistently shown significant enhancement in their visualization confirming this nonlinear behavior. In this paper, we describe a post-beamforming nonlinear filtering algorithm based on second-order Volterra filter (SVF) model that separates the linear and quadratic components of the echo signal leading to significant enhancement of lesion visualization. Images from *ex vivo* tissue samples are shown to demonstrate the level of contrast enhancement achieved with the SVF-based quadratic filter compared with standard echo and 2nd harmonic imaging results.

1. INTRODUCTION

Since early 2001, we have used a dual-mode array described in [1] to form HIFU-induced thermal lesions in freshly excised degassed tissue under a variety of *normal exposure* and *over exposure conditions*. Single-transmit focus images were collected for over 100 lesions before and after lesion formation. These images have consistently shown 5 - 7 dB enhancement in the echogenicity from the lesion location in the standard echographic images. These results were much more consistent than the reported "flashes" on the B-scan images when diagnostic ultrasound systems are used to monitor HIFU lesion formation. Motivated by the excellent investigation by P. P. Lele reported in [2], we hypothesized that this change in echogenicity is due to stable microbubbles that can occur even at low insonation levels. Lele found that subharmonic emission due to microbubbles showed a monotonic increase with intensity from 150 mW/cm² to 1500 W/cm² without a distinct threshold for emission (measurements done *in vitro* and *in vivo* at 2.7 and 1.8 MHz). The consistency of the increase in echogenicity

at the lesion may be explained by the fact that the microbubbles may already be resonant at the imaging frequency (same as the therapeutic HIFU beam when the dual-mode array is used), perhaps a result of rectified diffusion.

The standard echographic images at the fundamental, however, offer limited contrast enhancement due to the speckle phenomenon. Therefore, they could not provide a reliable method for mapping the boundaries of HIFU-induced lesions. This lead us to try to exploit the nonlinear nature of the microbubbles to enhance the visualization and mapping of thermal lesions. The idea was that, if microbubbles are indeed present at the lesion location, they will generate nonlinear echoes that may be better suited for mapping. We have initially investigated second harmonic (SH) imaging as a means of enhancing the lesion contrast for improving the visualization of these images. SH images of thermal lesions have shown increase in the contrast on the order of 22 - 25 dB, but with decreased dynamic range of the resulting images [1]. A post-beamforming nonlinear compounding algorithm was shown to improve the contrast in lesion echogenicity to 30 - 35 dB without loss in dynamic range [3]. This was achieved by compounding the fundamental and the SH images using spatial compounding functions based on the receive beamforming characteristics of the dual-mode array at the fundamental and the SH frequencies. In this paper, we describe a post-beamforming filtering algorithm for separating the linear and quadratic components of the beamformed data based on the SVF. This approach is superior to all of the algorithms based on SH imaging. It greatly enhances lesion to tissue contrast without any loss in spatial resolution. In addition, it enhances the dynamic range of the image thus greatly improving both detecting and mapping of HIFU-induced lesions, even for volumetric lesions.

2. IMAGE FORMATION

Figure 1 summarizes the image acquisition and image formation model. A 64-element array optimized for maximum energy delivery at 1 MHz (Imasonic, Besançon, France)

Funded by Grant DAMD 17-01-1-330 from the US Army Medical Research and Materiel Command and Esaote, S.p.A., Genoa, Italy.

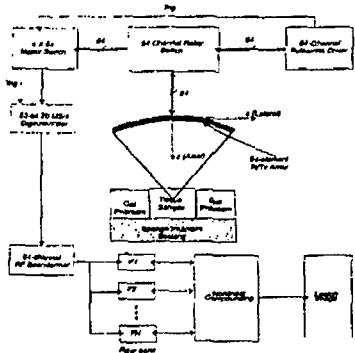


Fig. 1. Imaging Setup

is used for lesion formation in sample tissue. Lesions are formed by focusing the array at a point within the target and maintaining high-power output for time intervals on the order of seconds (1-5 seconds typical). The power is interrupted for short intervals (milliseconds) to acquire image data by transmitting short (μ s) pulse from all 64-elements and receiving on selected elements using a matrix switch. Once the image data set is collected, RF beamforming is performed to form standard echographic images of the target region. Figure 1 also shows a general post-beamforming filter bank for analysis of beamformed data. For example, the filter bank could be designed to perform harmonic decomposition of beamformed data (e.g., fundamental and 2nd harmonic imaging). Alternatively, the filter bank can be designed to separate the linear and quadratic (nonlinear) components based on the 2nd order Volterra model described below.

3. SECOND-ORDER VOLTERRA MODEL

Results from [4] have shown the validity of a second-order Volterra filer as a model for pulse-echo ultrasound imaging data from tissue mimicking media. In this section, the decomposition of received echo, i.e., output sequences only, into linear and quadratic components by using least-squares approach of second-order Volterra model will be considered and the detail of algorithm implementation to pulse-echo ultrasound imaging will be stated.

3.1. Signal Separation Model

The algorithm described in this section is adapted from [5]. The response of a quadratically nonlinear system, $y(n+1)$, can be predicted by a second-order Volterra model of past

m values as follows:

$$y(n+1) = y_L(n+1) + y_Q(n+1) \\ \sum_{i=0}^{m-1} y(n-i)h_L(i) \\ + \sum_{j=0}^{m-1} \sum_{k=j}^{m-1} y(n-j)y(n-k)h_Q(j,k) + \varepsilon(n), \quad (1)$$

where $h_L(i)$ is linear filter coefficients, $h_Q(j, k)$ represents quadratic filter coefficients and $\varepsilon(n)$ is a modelling error and/or a measurement noise which is assumed to be an independent, identically distributed (i.i.d) random variable with zero mean. That is, if the model coefficients are known, the echo signal can be decomposed into linear and quadratic components. The latter can be expected to better represent the quadratic response of the system than, say, the second harmonic component. The model coefficients can be obtained by setting the linear and quadratic prediction problem in Equation 1 to form a set of linear equations. Recognizing that the output is linear in terms of the (unknown) model coefficients, one obtains a matrix equation of the form:

$$\mathbf{f} = \mathbf{G}\mathbf{h} + \boldsymbol{\epsilon}, \quad (2)$$

where the vector \mathbf{f} , the matrix \mathbf{G} and the error vector ϵ are

$$\begin{aligned}\mathbf{f} &= [y(n+1), y(n+2), \dots, y(n+L)]^T \\ \mathbf{G} &= [\mathbf{y}(n), \mathbf{y}(n+1), \dots, \mathbf{y}(n+L-1)]^T \\ \boldsymbol{\epsilon} &= [\boldsymbol{\epsilon}(n), \boldsymbol{\epsilon}(n+1), \dots, \boldsymbol{\epsilon}(n+L-1)]^T.\end{aligned}$$

where the data vector, y , is given by:

$$\mathbf{y}(n) = [y(n), y(n-1), y(n-2), \dots, y(n-m+1), \\ y^2(n), y(n)y(n-1), \dots, y^2(n-m+1)]^T$$

and the filter coefficient vector, \mathbf{h} , is given by:

$$\mathbf{h} = [h_L(0), h_L(1), h_L(2), \dots, h_L(m-1), \\ h_Q(0,0), h_Q(0,1), \dots, h_Q(m-1, m-1)]^T.$$

The details of the solution for the coefficients of the SVF model can be found in [6]. Briefly, a minimum-norm least-squares solution of (2) is obtained using *truncated singular value decomposition*, *TSVD*. To assess the performance of the signal separation model in enhancing the lesion visualization, we compute the contrast-to-tissue ratio:

$$CTR = 10 \log_{10} \left(\frac{\|y_{QC}\|_2^2}{\|y_{QT}\|_2^2} \right) \quad (3)$$

where $\|\mathbf{y}_{QC}\|_2$ and $\|\mathbf{y}_{QT}\|_2$ are the l_2 norms of the quadratic components from the lesion and normal tissue regions, respectively. These regions are easily identified under various imaging conditions. For instance, for the application described in this paper, the contrast region is the expected location of the thermal lesion (often visible on the standard echographic image).

3.2. Implementation

The coefficients of the linear and quadratic components of the SVF model are obtained from the beamformed RF data. The implementation steps are as follows:

1. Using the standard echographic image, select a beamformed RF data segment from the expected lesion location.
2. Form the linear systems of equations according to (2).
3. Define contrast region (within the lesion) and normal tissue region for the computation of the mean-square error MSE and CTR .
4. Solve systems of linear equations by using TSVD regularization method.
5. Apply second-order Volterra filter to the beamformed RF data throughout the pulse-echo ultrasound image.
6. The quadratic component from the SVF can be displayed as a separate image or appropriately compounded with the linear component.

4. RESULTS AND DISCUSSION

The experimental setup shown in Figure 1 was used in obtaining images of *ex vivo* tissue samples before and after thermal lesion formation with a dual-mode 64-element ultrasound phased array operating at 1 MHz. The standard echographic images were formed by single transmit beams [1] along the main axis of the array and dynamic receive focusing at each pixel in the image. Results shown in [1] confirmed that echoes from the lesion location exhibited increased levels of second harmonic generation even at normal exposure conditions. Figure 2 shows the RF data along central axis of the dual-mode array before and after lesion formation at normal exposure level (850 W/cm^2 for 4 seconds). The figure also shows spectrograms of the RF data (showing the frequency content of the RF echoes in the axial direction). The results show that the echoes before lesion formation are centered at 1 MHz with no evidence of 2nd harmonic component in the tissue region (from 80 to 120 mm). On the other hand, the spectrogram of the RF data from the same direction after lesion formation shows a strong 2nd harmonic component at the lesion location (90 - 100 mm). Figure 3 shows the RF data along central axis of the dual-mode array before and after lesion formation at normal exposure level (2150 W/cm^2 for 3 seconds). The spectrograms show that the echoes before lesion formation are centered at 1 MHz with small 2nd harmonic component in the tissue region (at 100 mm). The spectrogram of the RF data from the same direction after lesion formation shows a strong 2nd harmonic component starting at 82 mm. This is consistent with the shape of the lesion determined by histological evaluation [1] (tear-drop cross section with the tip near the geometric center and the base near the front of the sample). It is interesting to note that, in addition to the

increased 2nd harmonic generation, the echoes from the lesion appear to have wider bandwidth compared to echoes from the same location before lesion formation. This is reminiscent of the behavior of ultrasound contrast agents (UCAs). It provides indirect evidence that bubble oscillation occurs during and after lesion formation and lingers for tens of seconds (*in vitro* depending on lesion size).

In [1] we have shown images of single shot HIFU lesions at the fundamental and SH frequencies of the dual-mode transducer. Both imaging modes produced satisfactory images of the lesion in these cases, with the SH images providing higher contrast of lesion echogenicity. However, both of these methods suffer when imaging extended lesions. One such example is shown in Figure 4 before (left) and after lesion formation at the fundamental (top pair), SH (middle pair) and using the quadratic component from the SVF (bottom pair). One can easily observe the increase in echogenicity at the lesion location (90 - 100 mm along the axis of the array) for all three modes. However, one can see that the dynamic range of the fundamental image is limited by the speckle pattern from tissue surrounding the lesion while the SH image is limited by the beamforming artifacts. The lesion echogenicity in this case is nearly 17 dB above the normal tissue echogenicity in standard echographic image (typical contrast is more like 5 - 7 dB). The SH images improve the lesion contrast to approximately 25 dB compared to normal tissue (22 - 25 dB typical), but beamforming artifacts compromise the definition of the lesion boundaries in the lateral direction.

Using a beamformed echo data segment along the main axis of the array, the coefficients of linear and quadratic components of the SVF were estimated as described in Section 3.2. The quadratic components of the beamformed RF data were filtered out at all pixel locations. The images before and after lesion formation are shown in Figure 4 at 40 dB dynamic range. One can see quite clearly that the grating lobe components visible in the 2nd harmonic images are effectively eliminated in the quadratic component images obtained through the SVF. In addition, the speckle components conspicuous in the standard echo images is greatly reduced. This level of enhancement is typical and has been observed consistently in over 100 experiments similar to the one described in this paper. The reader can appreciate that the lesion boundaries are well defined in both the axial and lateral directions. With the significant increase in dynamic range, one can see that both detection and mapping of thermal lesions is significantly facilitated by the use of the quadratic filter based on the SVF model.

5. CONCLUSIONS

Experimental results from *ex vivo* tissue samples provide the strongest evidence yet that thermal lesions exhibit non-linear behavior as a propagation medium. Using the SVF

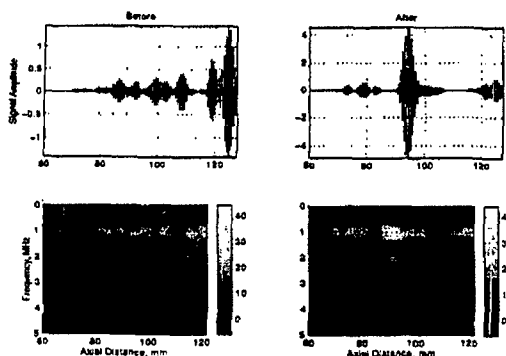


Fig. 2. RF data and spectrograms before(left) and after (right) *normal exposure*.

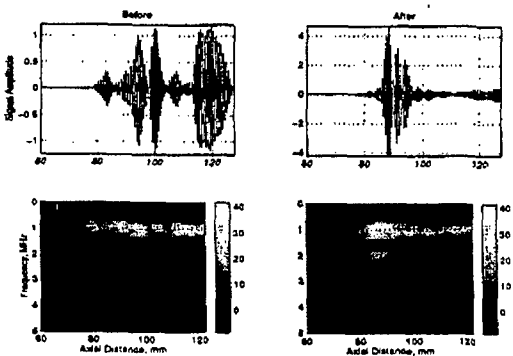


Fig. 3. RF data and spectrograms before (left) and after (right) *over exposure*.

model, we have separated the linear and quadratic components in the beamformed RF echo data and formed images from the quadratic component images show significant enhancement in lesion visualization due to:

1. They directly exploit the nonlinear nature of freshly formed thermal lesion (possibly due to formation of microbubbles).
2. Quadratic component combines both low frequency (close to dc) and harmonic frequency in forming nonlinear echoes. This simultaneously reduces speckle and beamforming artifacts without loss in spatial resolution.
3. The quadratic kernel of the SVF rejects the additive white Gaussian noise components which significantly improves the SNR of the imaging system and enhances the visualization of low echogenicity regions in the image.

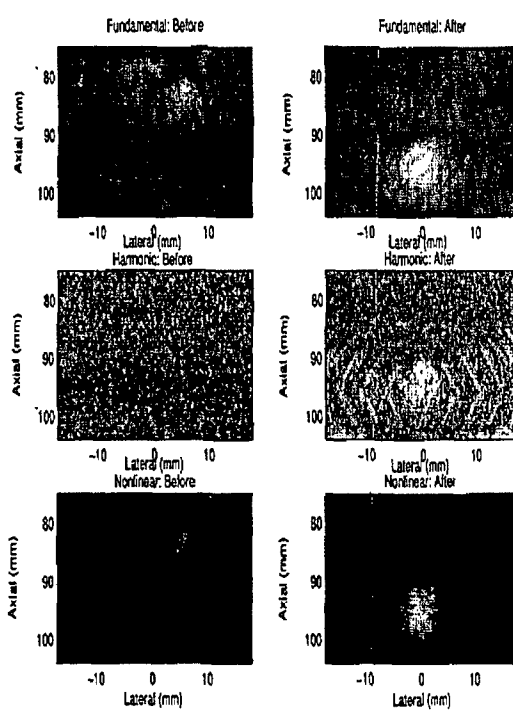


Fig. 4. Images before (left) and after (right) formation of lesion. Top: standard echo. Middle: second harmonic. Bottom: Quadratic.

6. REFERENCES

- [1] E. Ebbini, J. Bischof, and J. Coad, "Lesion formation and visualization using dual-mode ultrasound phased array," in *2001 Ultrasonics Symposium*, 2001, vol. 2, pp. 1351-1354.
- [2] M. H. Repacholi, M. Grandolfo, and A. Rindi, Eds., *Effects of ultrasound on solid mammalian tissue and tumors in vivo*, Plenum, London, 1987.
- [3] C. Steidl, H. Yao, P. Phukpattaranont, and E. Ebbini, "Dual-mode ultrasound phased arrays for noninvasive surgery post-beamforming image compounding algorithms for enhanced visualization of thermal lesions," in *2002 Int. Symposium on Biomedical Imaging*, 2002, pp. 429-432.
- [4] H. Yao, P. Phukpattaranont, and E. S. Ebbini, "Post-beamforming second-order Volterra filter for nonlinear pulse-echo imaging," in *ICASSP*, 2002, vol. 2, pp. 1133-1136.
- [5] K. Kim, S. B. Kim, E. J. Powers, R. W. Miksad, and F. J. Fischer, "Adaptive second-order Volterra filtering and its application to second-order drift phenomena," *IEEE J. Oceanic Eng.*, vol. 19, no. 2, pp. 183-192, Apr. 1994.
- [6] P. Phukpattaranont and E. Ebbini, "Post-beamforming Volterra filter for contrast agent imaging," in *2002 Ultrasonics Symposium*, 2002, vol. 2.

APPENDIX IV

DUAL-MODE ULTRASOUND PHASED ARRAYS FOR IMAGING AND THERAPY

Hui Yao and Emad S. Ebbini
Department of Electrical and Computer Engineering
University of Minnesota, Minneapolis, MN 55455

Abstract — We have recently demonstrated the imaging capabilities of a prototype 64-element 1 MHz concave array with 100 mm radius of curvature. This array was optimized for therapeutic applications using high-intensity focused ultrasound (HIFU). We have shown that this dual-mode ultrasound array (DMUA) has a therapeutic operating field (*ThxOF*) that extends by ± 3 cm and ± 2 cm around its geometric center in the axial and lateral directions, respectively. We have also shown that appropriate apodization and accounting for element directivity along with conventional synthetic aperture beamforming produce a 50 dB imaging field of view (*IxF*OV) larger than the *ThxOF*. In addition, the spatial registration of imaging targets is as accurate as commercially available scanners. In this paper, we present results from an image-based refocusing algorithm whereby images formed by the DMUA are used to identify a refocusing target and a set of critical points where the incident power is to be minimized. The algorithm is validated experimentally in tissue mimicking phantom with strongly scattering ribs placed between the DMUA and the target. These results demonstrate what is potentially the most powerful advantage of the use of DMUAs in image-guided surgery. Namely, the inherent registration between the imaging and therapeutic coordinate systems. This allows for direct definition of targets and any surrounding critical structures to be avoided to minimize the collateral damage. With these capabilities, DMUAs may provide a most powerful paradigm for image-guided surgery.

I. INTRODUCTION

Recently, non-invasive and minimally invasive thermal surgeries have become widely accepted in clinics and hospitals worldwide. Reliable imaging techniques for aiming, monitoring and visualization can help clinics gradually accept non-invasive and minimally invasive thermal surgeries. Image guidance methods based on MRI [1], CT [2] and ultrasound [3] have been recently proposed.

Most of the image guidance systems, including some ultrasound systems, have separate image guidance sub-system and therapeutic sub-system. The advent of piezocomposite transducer technology has made it feasible to design and fabricate dual-mode arrays capable of high-power therapeutic delivery while having a wide enough bandwidth for pulse-echo operation. One such DMUA has been described and introduced in our previous reports (e.g. [3]). The *ThxOF* for this prototype was experimentally shown to match the theoretically predicted profile based on array and element directivity analysis [3]. Furthermore, the *IxF*OV was also

shown to extend beyond the *ThxOF* for this prototype [4].

The main advantage of this approach is the inherent registration between the therapeutic and imaging coordinate systems. Once the real-time imaging capability is available for DMUAs, one can envision a treatment paradigm in which the HIFU beam is guided in real-time based on imaging of the treatment field by the same transducer. The doctor only needs to locate the target on the image and the system automatically generates the amplitude and phase distribution to focus the HIFU pulse at the desired target. In addition, it is possible to define additional points in the treatment field where the incident power is to be minimized to reduce or eliminate collateral damage, e.g. to nearby bone structures. In this paper, we present the first experimental verification of an image-based refocusing algorithm employing images from the DMUA prototype to identify the refocusing target as well as a number of critical structures to be avoided. One obvious application of this capability is targeting tumors in the liver that are partially obstructed by the ribcage [5]. This capability is unique to DMUAs due to the inherent registration between the imaging and therapeutic coordinate systems.

II. THEORY

A. Synthetic Aperture (SA) Imaging

Images were obtained using a full synthetic aperture technique [6]. The image pixel at coordinates (x_p, z_p) was therefore computed by [3]:

$$I(x_p, z_p) = \sum_{i=1}^{64} \sum_{j=1}^{64} A_i \cdot B_j \cdot s_{i,j}[(R_{ip} + R_{jp})/c], \quad (1)$$

where i is the transmit element index, j is the receive element index, A_i is the transmit apodization weight at element i , B_j is the receive apodization weight at element j , R_{ip} and R_{jp} are the distance from the transmit and receive element, respectively, from the image pixel, c is the speed of sound in the medium being imaged, and $s_{i,j}(t)$ is the echo acquired where transmitting with element i and receiving with element j . Specialized image reconstruction programs were written to evaluate the intensity at (x_p, z_p) .

B. Single-Transmit Focus (STF) Imaging

The synthetic aperture imaging algorithm described above can be used to produce higher quality conventional images

than can be expected from a given array. However, due to the fact that transmit beams are synthesized by superposition of single-element transmit patterns, the nonlinear interactions of the real-time transmit beams cannot be accounted for using the imaging algorithms. Therefore, we have modified our 64-channel phased array driver to allow for pulsed transmission on all 64 channels simultaneously. This allowed us to use the full power of the transmit beams and, therefore, observe their nonlinear interactions with the tissue media. The image formation process due to a single transmit focused beam is a modified version of Eq. (1) as follows:

$$I(x_p, z_p) = \sum_{j=1}^{64} B_j \cdot s_j[(R_0 + R_{jp})/c], \quad (2)$$

where $s_j(t)$ is the received waveform at element j due to the transmitted beam and R_0 is a fixed distance determined by the focal depth of the transmit beam. All other quantities in Eq.(2) are the same as their counterparts in Eq. (1).

C. Special Considerations

In conventional phased-array beamforming, grating-lobe levels are determined by the array pattern as well as the element directivity. Both of these factors are important in DMUAs as the array elements typically have high directivity.

1) *Array Gain Compensation (GC) Algorithm:* The intensity gain is defined as the peak field intensity in W/cm^2 divided by the average W/cm^2 output from the array at a set of field locations. In order to correctly calculate the contrast ratio of the image in a speckle region, gain compensation is required. Since the array is dynamically focused on both transmit and receive, 2-way compensation is utilized.

2) *Element Directivity (ED) Algorithm:* Accounting for element directivity in the beamforming algorithm reduces the grating lobes and, consequently, improves the dynamic range. Furthermore, accounting for element directivity affects the SNR of the resulting image. The element directivity weight function is:

$$D(\theta_{pe}) = \frac{\sin[kw \sin(\theta_{pe})/2]}{kw \sin(\theta_{pe})/2} \quad (3)$$

where $k = \frac{2\pi}{\lambda}$, λ is the wavelength, w is the element width, θ_{pe} is the angle between the axis of the radiating (receiving) element and the vector from the element center to the pixel.

D. Refocusing in the Presence of Obstacles

Assume we have an N -element array with arbitrary, but known, geometry radiating into a homogeneous half space. The objective is to maximize the array intensity gain at a target point \vec{r}_T while minimizing the incident power at a set of critical points, $\vec{r}_C(i)$, $i = 1, 2, \dots, M_C$. This is an optimization problem that can be solved using Lagrange multipliers or a regularized minimum-norm least squares solution as follows [5]:

- Let the raw vector $\mathbf{h} = [h_1(\vec{r}_T), h_2(\vec{r}_T), \dots, h_N(\vec{r}_T)]$ be the array directivity vector at \vec{r}_T (note that $h_k(\vec{r}_T)$ is the directivity of the k th element at \vec{r}_T).
- Form the matrix \mathbf{H}_C from the raw vectors $\mathbf{h}_i = [h_1(\vec{r}_C(i)), h_2(\vec{r}_C(i)), \dots, h_N(\vec{r}_C(i))]$.
- Form the weighting matrix, $\mathbf{W}_C = (\mathbf{H}_C \mathbf{H}_C^* + \gamma \mathbf{I})^{-1}$ where \mathbf{I} is the identity matrix and γ is an appropriately chosen regularization parameter.
- The optimal complex array driving vector is given by $\mathbf{u} = \mathbf{W}_C \mathbf{h}_T^{*t} (\mathbf{h}_T \mathbf{W}_C \mathbf{h}_T^{*t})^{-1}$.

Both the target and the critical points can be derived from images formed by the DMUA in synthetic aperture or in single-transmit focus modes. This is probably the most powerful feature of the use of the DMUA in image-guided applications.

III. EXPERIMENT SETUP

Figure 1 (left) shows the image acquisition model. A 64-element concave linear phased array is used for the image acquisition. The array can be connected to a 64-channel driver that can operate in CW therapeutic mode or pulsed imaging mode. It can also be connected to a standard pulser receiver through a matrix switch. Synthetic aperture images were obtained with the latter approach while single transmit images were obtained with the 64-channel transmitter. Figure 1 (right) shows a schematic of the DMUA with an imaging target containing three strongly scattering ribs on top of a tissue-mimicking phantom containing a strong scatterer near the geometric center of the DMUA. The target is a thermocouple wire 0.1 mm in diameter and the ribs are plastic bars with diameter of 8 mm. They are positioned in a plane just over 40 mm from the vertex of the DMUA with approximate spacing of 20 mm between them.

A modified Technos MPX system from ESAOTE, Genoa, Italy is used to acquire images for comparison with images of the same target from the DMUA. The system is modified to allow the upload of high-quality beamformed RF data from the Technos system to computer. A CA 421 convex abdominal probe is used to acquire images from the same target as the DMUA.

IV. RESULTS

A. Synthetic Aperture Imaging

Two examples of SA imaging with the DMUA are shown to demonstrate its imaging capability. The first is the result of a 3D contrast target in a quality assurance phantom and the second is a tissue mimicking phantom with rib obstacles used in the refocusing experiments described below.

1) *3D Contrast Phantom:* Figure 2 shows grayscale images (50 dB) of an egg-shaped 3D contrast object within the CIRS Model 55 3D contrast phantom. The image on the left was obtained using the DMUA while the one on the right was obtained using the Technos with the CA421 convex probe. The contrast ratio (CR) for the egg-shaped con-

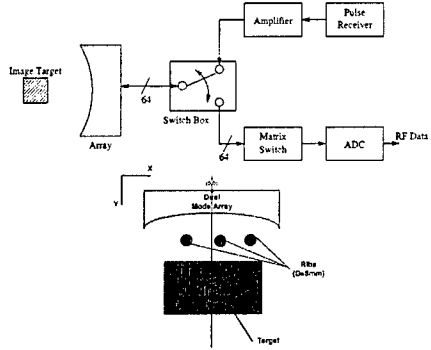


Figure 1: Dual-mode system for lesion and image formation and imaging target with obstacles used in refocusing experiments.

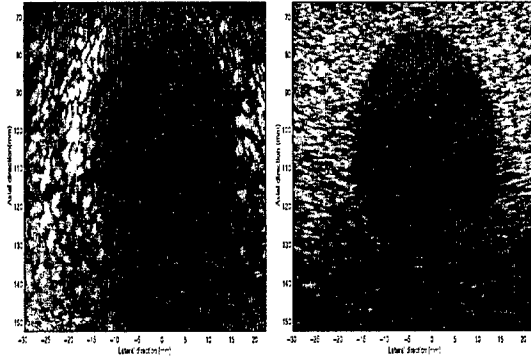


Figure 2: Images (50 dB) from the CIRS Model 55 3D contrast phantom. Left: DMUA w/ GC; Right: Technos.

contrast target was computed as follows:

$$CR = 10 * \log_{10} \left(\frac{\sum_{i=1}^{N_r} I_t(i)}{\sum_{i=1}^{N_r} I_c(i)} \right), \quad (4)$$

where $I_c(i)$ [$I_t(i)$] is the average intensity in a $3 \times 3 \text{ mm}^2$ region inside [outside] the contrast target and N_r is the number of regions. The CR value determined from image of DMUA (with gain compensation) and the image from the CA 421 probe are 8.35 dB and 9.12 dB, respectively. These values are quite consistent with the manufacturer specified contrast of 9 ± 0.5 dB. It should be mentioned that, without compensating for intensity gain and element directivity for the DMUA, the contrast ratio would have been 3.3 dB instead of 8.35 dB. It is also interesting to note that the distal edge of the egg-shaped object marks the far end of the 50 dB I_x -FOV of the DMUA. One can visually observe the loss of contrast in that region. Spatial and contrast resolution results for various beamforming conditions are shown in [4].

2) *Tissue-Mimicking Phantom with Obstacles*: Figure 3 shows a grayscale image (50 dB) of the phantom shown in

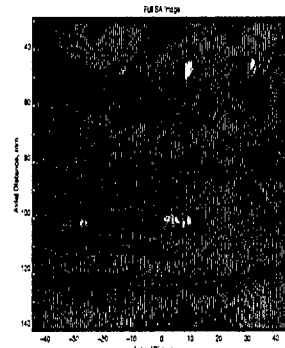


Figure 3: Grayscale image of the tissue-mimicking phantom with ribs shown in Figure 1t acquired using the DMUA in synthetic aperture mode (50 dB).

Figure 1. The image was obtained using the full synthetic aperture technique described in Section II-A. The result is consistent with the schematic with good spatial resolution as well as contrast. In addition to the target and the ribs, the front and back of the tissue-mimicking phantom can be easily discerned (at 80 and 120 mm, respectively). Even though the ribs may be outside the 50 dB I_x FOV of the DMUA, they are sufficiently strong to stand out giving strong specular reflections. Furthermore, the ribs are all spatially registered correctly without distortion.

B. Single-Send Focus Imaging

Single-send focus imaging can be extremely useful in conjunction with DMUAs in image-guided surgery. By imaging the target tissue using the delay and magnitude profile of the therapeutic beam, it is possible to visualize any strongly scattering structures directly affected by this beam. Figure 4 shows the STF image obtained using a transmit focus at 0 lateral and 100 mm axial (geometric focus). The image is displayed with 40 dB dynamic range and shows that two of the three ribs are visible in addition to the target near the geometric center. This result implies that the transmit focus, when used in therapeutic mode, may cause excessive heating at one or two of the ribs visible on the image.

While the STF image clearly has lower contrast than the full SA image shown in Figure 3, it still shows the target and two of the ribs with good spatial registration. Therefore, it is still useful for identifying targets and potential obstacles as described in the next subsection.

C. Refocusing in the Presence of Obstacles

The image shown in Figure 4 was used to identify the coordinates of the visible ribs as well as define a target point for refocusing within the tissue mimicking phantom. The 40 dB grayscale images shown in Figure 5 show the results of refocusing without (left) and with (right) taking the rib location into consideration. Both of these images were obtained

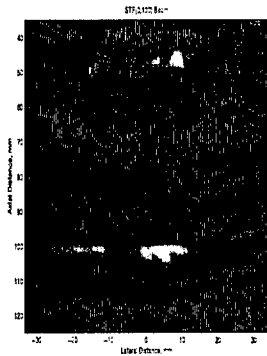


Figure 4: STF image (40 dB) of the target shown in Figure 3. Strong echoes from the three ribs are evident while the needle is less visible.

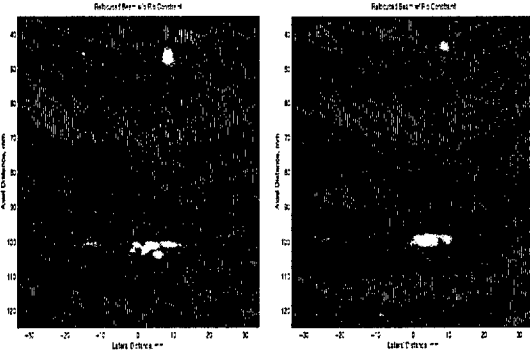


Figure 5: STF images (40 dB) using refocusing without (left) and with (right) taking the critical points are the ribs into consideration.

with a transmit beam focused at the defined target location at 5 mm lateral and 100 mm axial. However, the image on the left was obtained using the algorithm described in Section II-D. One can clearly see the increased visibility of the target compared to the visibility of the ribs. This is due to the reduction of incident power at the ribs as predicted by the weighting algorithm described in Section II-D.

V. DISCUSSION AND CONCLUSIONS

Characterization of the image quality from the DMUA demonstrates the feasibility of using this array in image-guided surgical applications. The spatial and contrast resolutions of this array, while not sufficient for high-quality diagnostic applications, are consistent with the bandwidth and geometry of the array. Furthermore, the speckle components of the beamformed data is suitable for relevant signal processing algorithms such as displacement tracking and temperature estimation.

This paper has also presented the first experimental verification of the feasibility of using image-based refocusing for targeting tissue structures while avoiding critical obstacles

such as the ribs. This may be important if HIFU arrays are to be used for targeting, for example, liver tumors that may be partially obstructed by the rib cage. This result is not to be understood as a form of aberration correction since the refocusing algorithm assumes knowledge of the array directivity at the refocusing target and the critical points. Nonetheless, since these same assumptions are used in beamforming the image in the first place, the algorithm is quite robust against distortions due to inaccuracies in the speed of sound and other tissue properties. The only requirement is that the SA or the STF image used in refocusing provides a recognizable map of the treatment region.

The image quality currently available for DMUAs with image formation techniques described herein may not be sufficient to justify identifying more complex lower scattering critical structures. Furthermore, we are not suggesting that targets such as tumors can be recognized on images provided using the DMUA. However, continued improvement of piezocomposite transducer technologies, especially improved bandwidths of high-power arrays, may bring about sufficient improvement in the image quality to make that possible. In any event, the current image quality may allow for recognizing landmarks on the image that, with the help of more refined imaging systems, can be used in the targeting of tumors and less recognizable tissue structures as they appear on DMUA images.

ACKNOWLEDGMENTS

Funded by Grant DAMD17-01-1-0330 US Army Medical Research and Materiel Command.

VI. REFERENCES

- [1] J. Poorter, C. Wagter, Y. Deene, C. Thomsen, and F. Stahlberg, "Noninvasive MRI thermometry with the proton resonance frequency (PRF) method: In vivo results in human muscle," *Magn. Reson. Med.*, vol. 33, pp. 74–81, 1995.
- [2] P. Mcaney, K. Paulsen, A. Hartov, and R. Crane, "Initial *in vivo* experience with EIT as a thermal estimator during hyperthermia," *Ultrasound Med. Biol.*, vol. 12, pp. 573–591, 1996.
- [3] H. Yao, P. Phukpattaranont, and E.S. Ebbini, "Enhanced lesion visualization in image-guided noninvasive surgery with ultrasound phased arrays," in *Proc. of the 23rd Annual Int. Conf. of the IEEE*, 2001, vol. 3, pp. 2492–2495.
- [4] H. Yao and E.S. Ebbini, "Imaging with large-aperture arrays with heterogeneous directive elements," in *Proc. of the IEEE Ultrasonics Symposium*, 2003, vol. 2, pp. 1243 – 1246.
- [5] Y.Y. Botros, E.S. Ebbini, and J.L. Volakis, "Two-step hybrid virtual array-ray (var) technique for focusing through the rib cage," *Ultrasonics, Ferroelectrics and Frequency Control, IEEE Trans.*, vol. 45, pp. 989 – 1000, 1998.
- [6] K. Thomenius, "Evolution of ultrasound beamformers," in *1996 IEEE Ultrasonics Symposium*, 1996, pp. 1615–1622.

POST-BEAMFORMING SECOND-ORDER VOLTERRA FILTER FOR NONLINEAR PULSE-ECHO IMAGING

Hui Yao, Pornchai Phukpattaranont and Emad S. Ebbini

Department of Electrical and Computer Engineering
University of Minnesota
Minneapolis, MN 55455

ABSTRACT

In this paper, we demonstrate that a second-order Volterra filter (SVF) can adequately model pulse-echo imaging data acquired from tissue media. Furthermore, we demonstrate that the coefficients of both the linear impulse response and the second-order kernel can be robustly estimated from imaging data using pseudorandom binary input sequences. The validation of the SVF as an appropriate model for ultrasonic imaging will allow for more intelligent use of post-beamforming signal processing for enhancing image contrast and producing quantitative imaging.

1. INTRODUCTION

Modern ultrasonic imaging is moving rapidly towards new paradigms employing post-beamforming filtering combined with nonlinear imaging modes [9, 1]. Native tissue-harmonic (NH) and contrast-agent (CA) imaging are currently the leading applications being investigated in many laboratories around the world [4, 1, 5]. Figure 1 represents a general scheme of a modern ultrasound data acquisition and reconstruction employing post-beamforming filter bank for signal separation and compounding. Once the image data set is collected, RF beamforming is performed to form standard echographic images of the target region. Post-beamforming filterbank is used to separate signal components of beamformed RF data based on space-time processing of echoes from different directions [8] or appropriate nonlinear filtering depending on a known or identified model of the nonlinear system. As an example of the latter, nonlinear imaging used in practice on medical scanners send transmit pulses centered at a frequency f_0 and detects signal components at $2f_0$ to produce images with improved contrast with or without contrast agents. Until very recently, this was the approach taken for both NH and CA imaging. A better understanding of the nature of nonlinearity as well as the availability of advanced VLSI for signal processing have been the driving forces behind the development of more sophisticated approaches to

Funded in part by Grant DAMD 17-01-1-330 from the US Army Medical Research and Materiel Command and by Esaote S.p.A., Genoa, Italy.

post-beamforming signal processing.

In this paper, we demonstrate the applicability of the SVF to the ultrasound pulse-echo imaging problem. Furthermore, we demonstrate that the SVF coefficients can be robustly estimated from pulse-echo data, even in the presence of strong speckle noise.

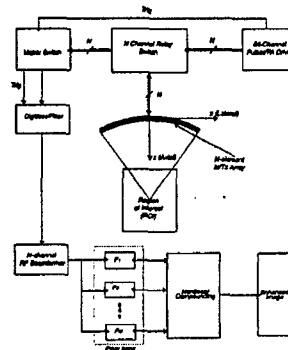


Fig. 1. Image Acquisition and Reconstruction Algorithm

2. IMAGE FORMATION MODEL

Synthetic Aperture Imaging [6]: The image pixel at coordinates (x_p, z_p) is computed by (Fig. 2):

$$I(x_p, z_p) = \sum_{i=1}^N \sum_{j=1}^N A_i \cdot B_j \cdot s_{i,j} [(R_{ip} + R_{jp}) / c], \quad (1)$$

where i is the transmit element index, j is the receive element index, A_i is the transmit apodization weight at element i , B_j is the receive apodization weight at element j , R_{ip} and R_{jp} are the distances from the transmit and receive elements, respectively, from the image pixel, c is the speed of sound in the medium being imaged, and $s_{i,j}(t)$ is the echo acquired when transmitting with element i and receiving with element j .

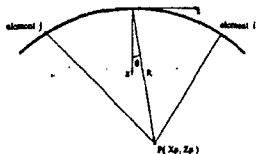


Fig. 2. Coordinate system used in the synthetic aperture imaging system.

Post Beamforming Filtering: Since beamforming is performed in the RF domain, all the frequency components in the received echo signals are retained. This is important since the echo signals can be expected to contain a mix of harmonics (and possibly subharmonics) depending on the nonlinearity of the tissue medium being imaged. This is especially true for the single-transmit imaging mode where the transmit power is sufficiently high to produce harmonic components in nonlinear tissue media. Postbeamforming filtering can be used to isolate specific harmonic components and/or enhance axial resolution if the SNR of the system is sufficiently high. Algorithms for postbeamforming filterbank image reconstruction for pulse-echo ultrasound can be found in [9].

2.1. Filter Bank Design

2.1.1. Linear Imaging Model for Coded-Excitation

We begin with an overview of the proposed coded-excitation imaging modality [8, 9]. We assume that the scatterers in the region of interest (ROI) are located on a uniform sector (r, ϕ) grid. A discretized model for the receive signal, denoted as $f(k)$, can be written as

$$f(k) = \sum_{i=1}^{N_\phi} \sum_{j=1}^{N_r} s_i(j) g_i(k-j) + n(k), \quad (2)$$

where N_r is the grid size determined by the range interval size and the sampling rate, $n(k)$ is the noise, $g_i(k-j)$ is the system impulse response created by a unit strength scatterer located on the at the j -th range grid position along the angle ϕ_i , and $s_i(j)$ is the actual scatterer strength at that location.

Let $G_i = [g_{i,1}, g_{i,2}, \dots, g_{i,N_r}]$ and $g_{i,j}$ be the vector version of $g_i(k-j)$. Then Equation 2 can be rewritten as

$$f = Gs + n, \quad (3)$$

where f , s and n are the vector versions of $f(k)$, $s(k)$ and $n(k)$, respectively. The imaging operator G , defined as

$$G = [G_1, G_2, \dots, G_{N_\phi}], \quad (4)$$

is a (typically, underdetermined) matrix operator consisting of N_ϕ linear convolution matrices. Thus, a unique minimum-

norm least square estimate (denoted by \hat{s} below) of the scatterer vector s can be expressed as

$$\hat{s} = G^{*t} (GG^{*t})^\dagger f, \quad (5)$$

where $*^t$ denotes the Hermitian transpose of a matrix. This is the familiar minimum-norm least-square solution to the image reconstruction problem. We have shown previously [9] that, under realistic assumptions, a singular value decomposition of the pseudoinverse can be obtained using the discrete Fourier transform (DFT). It is important to note here that, while the solution given in (5) is based on a superposition, it can be generalized to the nonlinear case when the appropriate model is used. The following section describes a commonly used nonlinear wave propagation model used for this purpose.

2.1.2. Nonlinear Model

The Khokhlov-Zabolotskaya-Kuznetsov (KZK) equation has been validated analytically and experimentally as an appropriate model for finite-amplitude (nonlinear) wave propagation in soft (water or tissue) media. It is typically solved numerically in normalized form in terms of the pressure, P , and the coordinates, (\tilde{x}, t) . For example, for a circularly symmetric source with radius, a and radius of curvature, d , the following normalized variables are defined in cylindrical coordinates:

$$P = p/p_0, \quad \sigma = z/d, \quad \rho = r/a, \quad \tau = \omega_0 t'$$

where p_0 is the hydrostatic pressure and ω_0 is the center frequency of the excitation signal. The normalized KZK equation takes the form:

$$\frac{\partial P}{\partial \sigma} = \frac{1}{4G} \int_{-\infty}^{\tau} \left(\frac{\partial^2 P}{\partial \rho^2} + \frac{1}{\rho} \frac{\partial P}{\partial \rho} \right) d\tau' + A \frac{\partial^2 P}{\partial \tau^2} + NP \frac{\partial P}{\partial \tau}. \quad (6)$$

In this equation, the following parameter are defined:

$$G = \frac{z_0}{d} = \frac{\omega_0 a^2}{2c_0 d}, \quad A = \alpha_0 d = \frac{\delta \omega_0^2 d}{2c_0^3}, \quad N = \frac{d}{z} = \frac{d \beta \omega_0 p_0}{\rho_0 c_0^3}$$

where G is a focusing gain, A is an absorption term, and N is the nonlinearity parameter of the medium. A complete description of the KZK is beyond the scope of this paper. For our purposes, however, it suffices to say that this was solved numerically and validated experimentally in different media. We use this equation to test the validity of the SVF model for nonlinear ultrasonic wave propagation and the system identification algorithm used to extract the SVF coefficients.

2.1.3. The Volterra Filter

Nonlinear processes can be modelled by general p -th order Volterra system [7]. Due to nature of the problem and computational complexity, we consider only the second-order

Volterra filter. The output of a SVF can be given by :

$$y(n) = h_0 + \sum_{k=0}^{N-1} h(k)x(n-k) + \sum_{i,j=0}^{N-1} q(i,j)x(n-i)x(n-j) \quad (7)$$

where $h(k)$ represents linear impulse response and $q(m, n)$ is quadratic kernel. The quadratic kernel is assumed to be symmetric, i.e., $q(i, j) = q(j, i)$ and h_0 is assumed to be zero. A parallel realization of the SVF is shown in Fig. 3. The identification problem in this paper is to find linear im-

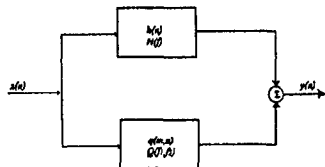


Fig. 3. Parallel realization of a second-order Volterra filter.

pulse response, $h(n)$ and quadratic kernel, $q(i, j)$ when input and output are known. Furthermore, we restrict the input to a class of pseudorandom binary sequences (e.g., Barker codes or maximal length sequences) that are readily available in many ultrasound and RADAR imaging systems.

2.1.4. Identification of Quadratic Nonlinear Systems

Identification of quadratic nonlinear system algorithm in this section is based on a digital method of modelling quadratically nonlinear systems with general random input discussed in [2]. Equation 7 can be represented in the frequency domain in term of the DFT of $y(n)$:

$$Y(f_k) = H(f_k)X(f_k) + \sum_{\substack{i,j=-\frac{M}{2}-1 \\ i+j=k}}^{\frac{M}{2}} Q(f_i, f_j)X(f_i)X(f_j) \quad (8)$$

where linear transfer function, $H(f_k)$, and quadratic transfer function, $Q(f_i, f_j)$, are unknown. M is the length of input sequence divided by two. Kim and Powers [2] proposed a general DFT-based solution for the system identification problem using higher-order spectra. We skip the details of the algorithm, but state that (8) can be written in matrix form:

$$Y(k) = \mathbf{x}^t \mathbf{h}, \quad (9)$$

where the DFT index, k , denotes the frequency f_k and the vector \mathbf{h} contains the coefficients $H(k)$ and all $Q(i, j) : i + j = k$. To solve the variable \mathbf{h} , both sides of (9) are multiplied from the left by \mathbf{x}^* and the expectation operator is applied resulting in,

$$E[\mathbf{x}^* Y(k)] = E[\mathbf{x}^* \mathbf{x}^t] \mathbf{h}. \quad (10)$$

Equation (10) is linear system of equations, which can be solved uniquely if $\{E[\mathbf{x}^* \mathbf{x}^t]\}^{-1}$ exists. The vector \mathbf{h} is given by:

$$\mathbf{h} = \{E[\mathbf{x}^* \mathbf{x}^t]\}^{-1} E[\mathbf{x}^* Y(k)] \quad (11)$$

To solve for every coefficient in the linear transfer function and quadratic transfer function, (11) is solved repeatedly for $k = 0, \dots, M$. For quadratic transfer function, the unknown variables are solved along diagonal lines $i + j = k$ in the 2D frequency plane. In addition, the symmetry properties of $q(m, n)$ are exploited to obtain a computationally efficient solution. Equation 11 was solved for the case of binary pseudorandom input sequences. The original algorithm calls for a full set of $M/2$ independent input sequences to insure a stable inverse. However, we have tested the use of a regularized solution to (11) using the pseudoinverse with a minimum set of training sequences. Robust estimates of the SVF coefficients were obtained using a small set of training sequences. This is important for a variety of imaging scenarios. For instance, high frame-rate imaging where we cannot afford to send tens of training sequences. Another example is imaging microbubble contrast agents where the time-invariance of the system holds for a few milliseconds requiring system identification to be completed using a few transmissions.

3. RESULTS AND DISCUSSION

Simulations: Figure 4 shows the result of simulating the propagation of a 3-cycle sinusoidal pulse using the KZK equation (solid lines) in time and frequency domain. The result show a classical nonlinear distortion of a narrowband pulse where the negative pressure peaks begin to distort to produce sharper negative to positive transition. If the pulse is allowed to propagate sufficiently long, the distortion produces a sawtooth waveform and eventually leads to a shock wave.

The SVF coefficients were obtained using the system identification algorithm described in Section 2.1.4 with 64-chip maximal length sequences. The predicted outputs from the SVF (dashed-dotted), the linear impulse response (dotted), and the quadratic kernel (dashed) are also shown for comparison. It can be seen that the linear impulse response predicts the linear output in the fundamental energy band (around 3 MHz). On the other hand, the quadratic kernel captures energy primarily from the 2nd harmonic and low frequency bands corresponding to second order nonlinearity. It should be noted that the quadratic kernel does not capture the 3rd harmonic band clearly present in the KZK output. This is a potential limitation of the SVF approach when the system to be identified is highly nonlinear. The simulation shown here, however, is an extreme case where the nonlinearity is higher than can be expected in practice.

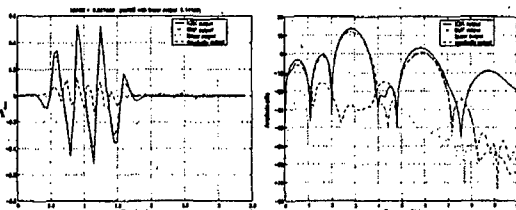


Fig. 4. Propagation of a 3-cycle sinusoidal pulse using the KZK model.

Experiment: Figure 5 shows the received signal from a 3-cycle sinusoidal pulse into a tissue mimicking phantom used for quality assurance testing of medical imaging scanners. The strong reflection at 6 cm is due to a wire resolution target positioned within a speckle region to simulate reflections from human liver. We used 64-chip maximal length sequences for identifying the SVF coefficients near the wire target. For clarity, we show the spectra of the predicted outputs (at the target location) due to the SVF (dashed-dotted), linear response (dotted), and the quadratic kernel (dashed). One can see that the linear filter captures the energy in the fundamental band while the second order kernel captures the energy at the low frequency and in the 2nd harmonic band. The significance of this result is that it was obtained based on training in the presence of strong speckle noise due to random scatterers surrounding the target (as is the case in practical medical imaging applications). Examples

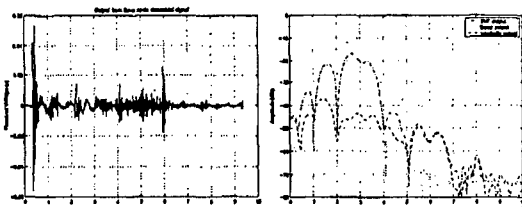


Fig. 5. Experimental pulse-echo data recorded from a 3-cycle transmission pulse into a tissue mimicking phantom.

of narrowband excitation pulses shown in this section were chosen to highlight the properties of the first and second order terms of the SVF in signal separation. It is important to note, however, that we have also investigated these properties for broadband excitation pulses, e.g., 13-chip Barker code. The results of the broadband case are similar except for the fact that the second order term captures significant nonlinear components in the fundamental band. This is represents a significant advantage of our approach over conventional nonlinear imaging based on detection of only second harmonic energy.

4. CONCLUSIONS

We have demonstrated the validity of a second order Volterra system as a model for pulse-echo ultrasonic imaging data from tissue mimicking media. In addition, a robust method for identification of the SVF coefficients have been demonstrated in the presence of speckle noise, an important result for medical ultrasound.

With the recent advances in VLSI signal processing architectures, adaptive imaging algorithms based on system identification tools are becoming increasingly attractive. The results presented in this paper demonstrate the feasibility of this approach to the emerging class of nonlinear imaging systems that will undoubtedly shape the future of medical ultrasonic imaging.

5. REFERENCES

- [1] S. Wilson M. Averkiou D. Skyba J. Power, T. R. Porter and M. Bruce. "Ultrasound contrast imaging research". *Medica Mundi*, 44(2), 2000.
- [2] K. I. Kim and E. J. Powers. "A digital method of modeling quadratically nonlinear systems with a general random input". *IEEE Trans. Acoust., Speech, Signal Processing*, 36(11):1758-1769, Nov. 1988.
- [3] T. Koh and E. J. Powers. "Second-order volterra filtering and its application to nonlinear system identification". *IEEE Trans. Acoust., Speech, Signal Processing*, ASSP-33(6):1445-1455, Dec. 1985.
- [4] S. R. Wilson P. N. Burns and D. H. Simpson. "Pulse inversion imaging of liver blood flow: Improved method for characterizing focal masses with microbubble contrast". *Invest Radiol*, 35(1):58-71, 2000.
- [5] C. T. Lancee J.R.T.C. Roelandt N. de Jong, F. J. Ten Cate and N. Born. "Principles and developments in ultrasound contrast agents". *Ultrasonics*, 29:324-330, Jul. 1991.
- [6] K. Thomenius, "Evolution of ultrasound beamformers," *IEEE Ultrason. Symp.*, pp. 1615-1622, Nov. 1996.
- [7] M. Schetzen. *The Volterra and Wiener Theories on Nonlinear Systems*. Krieger Publishing Company, Malabar, FL, updated edition, 1989.
- [8] J. Shen and E. S. Ebbini. "On the design of a transversal filter bank for parallel processing multiple image lines in real-time acoustic imaging". In *ICASSP*, volume 6, pages 3109-3112, 1996.
- [9] J. Shen and E. S. Ebbini. "Filter-based coded-excitation system for high-speed ultrasonic imaging". *IEEE Trans. Medical Imaging*, 17(6):923-934, December 1998.

ENHANCED LESION VISUALIZATION IN IMAGE-GUIDED NONINVASIVE SURGERY WITH ULTRASOUND PHASED ARRAYS

Hui Yao, Pornchai Phukpattaranont and Emad S. Ebbini

Department of Electrical and Computer Engineering
University of Minnesota
Minneapolis, MN 55455

Abstract- We describe dual-mode ultrasound phased arrays for noninvasive image-guided surgical applications. In particular, we address the problem of real-time visualization of thermal lesion formation in the target (e.g., tumor) tissue using the therapeutic arrays. Post beamforming filter bank image reconstruction with nonlinear compounding is utilized to improve the lesion contrast in the (typically) very low-contrast ultrasound images. It is shown that the new image reconstruction algorithm leads to measurable improvement in lesion contrast on the order of 6 - 15 dB. This leads to significant improvement in lesion detectability and size estimation by standard segmentation techniques for speckle imagery. Experimental results strongly suggest that 2nd Harmonic imaging could play an important role in the enhancement of real-time lesion visualization.

1. INTRODUCTION

Image guidance has long been recognized as the "enabling technology" for noninvasive thermal surgery. Highly refined energy application devices have been developed and for years. However, without reliable imaging techniques for visualization of thermal lesions, noninvasive thermal surgery has failed to find widespread acceptance in the clinic. Recently, image guidance methods based on well established imaging modalities like MRI[3], CT[5], or ultrasound [4, 8] have been proposed. Other imaging modalities are also being developed and may become available in the foreseeable future[6, 7].

An area unique to ultrasound that could revolutionize the field of image guided surgery is the development of a new generation of dual-mode high-power phased array systems capable of both imaging and therapy [8, 9]. These piezocomposite transducers can produce focal intensity levels needed for ablative and coagulative thermal surgery with high precision. Furthermore, the operating bandwidth of such transducers allows for imaging the treatment region

Funded by Grant DAMD 17-01-1-330 from the US Army Medical Research and Materiel Command.

with adequate image quality to delineate important landmarks within and around the target volume. With these capabilities, it is possible to operate these arrays in a "self-registration" mode whereby the imaging capabilities of the array are utilized in characterization of the tissue response precisely at the expected lesion location. This is due to the fact that the beamforming is common to both the imaging and therapy modes. The main challenge to this approach is the low-contrast nature of speckle-ridden ultrasound images. This paper addresses a new post beamforming filter bank image reconstruction algorithm with nonlinear spatially weighted compounding algorithm to mitigate this problem. The design of this algorithm is motivated by the nonlinear nature of ultrasound propagation in tissue and the fact that thermal lesions are known to have increased level of harmonic generation. Experimental results demonstrate the potential of the new algorithm in both enhancing the lesion contrast and size/shape analysis.

2. IMAGE FORMATION MODEL

Figure 1 summarizes the image acquisition and image formation model. A 64-element array optimized for maximum energy delivery at 1 MHz operating frequency is used for lesion formation in sample tissue. Lesions are formed by focusing the array at a point within the target and maintaining high-power output for time intervals on the order of seconds (1 - 5 seconds typical). The power is interrupted for short intervals (milliseconds) to acquire image data by transmitting short (μ s) pulses from all 64-elements and receiving on selected elements using a matrix switch. Once the image data set is collected, RF beamforming is performed to form standard echographic images of the target region. It is well known that these images have very low contrast due to the coherent nature of image acquisition which produces speckle. This renders the lesion detection very difficult using ultrasound.

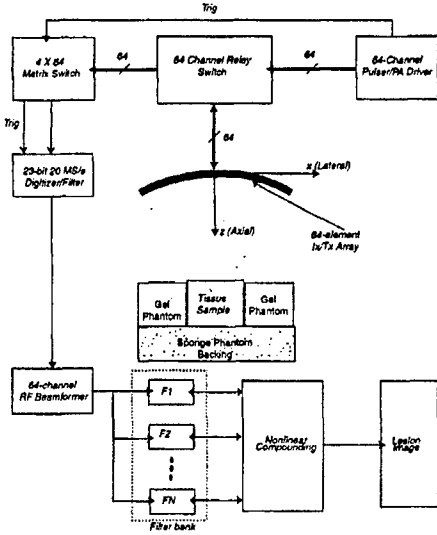


Fig. 1. Image Acquisition and Image Reconstruction Algorithm

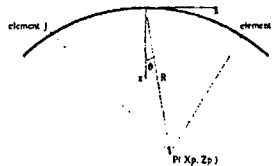


Fig. 2. Coordinate system used in the synthetic aperture imaging system.

2.1. Synthetic aperture imaging

Images were obtained using a full synthetic aperture technique [10]. The image pixel at coordinates (x_p, z_p) was therefore computed by (Fig. 2):

$$I(x_p, z_p) = \sum_{i=1}^{64} \sum_{j=1}^{64} A_i \cdot B_j \cdot s_{i,j} [(R_{ip} + R_{jp}) / c], \quad (1)$$

where i is the transmit element index, j is the receive element index, A_i is the transmit apodization weight at element i , B_j is the receive apodization weight at element j , R_{ip} and R_{jp} are the distances from the transmit and receive elements, respectively, from the image pixel, c is the speed of sound in the medium being imaged, and $s_{i,j}(t)$ is the echo acquired when transmitting with element i and receiving with element j . Specialized image reconstruction programs were written to evaluate the intensity at (x_p, z_p) in either $(r, \sin \theta)$ or Cartesian coordinates.

2.2. Single-Transmit Imaging

The synthetic aperture imaging algorithm described above can be used to produce the highest quality conventional images that can be expected from a given array. However, due to the fact that transmit beams are synthesized by superposition of single-element transmit patterns, the nonlinear interactions of the real-time transmit beams cannot be accounted for using this imaging algorithm. Therefore, we have modified our 64-channel phased array driver to allow for pulsed transmission on all 64 channels simultaneously. This allowed us to use the full power of the transmit beams and, therefore, observe their nonlinear interactions with the tissue media. The image formation process due to a single-transmit focused beam is a modified version of Eq. (1) as follows:

$$I(x_p, z_p) = \sum_{j=1}^{64} B_j \cdot s_j [(R_0 + R_{jp}) / c], \quad (2)$$

where $s_j(t)$ is the received waveform at element j due to the transmitted beam and R_0 is a fixed distance determined by the focal depth of the transmit beam. All other quantities in Eq. (2) are the same as their counterparts in Eq. (1). It should be noted that beamforming is performed in the RF domain using true delays, i.e., no baseband conversion is done. This retains all the frequency components in the beamformed data for postbeamforming operations described below.

2.3. Post Beamforming Filtering

Since beamforming is performed in the RF domain, all the frequency components in the received echo signals are retained. This is important since the echo signals can be expected to contain a mix of harmonics (and possibly subharmonics) depending on the nonlinearity of the tissue medium being imaged. This is especially true for the single-transmit imaging mode where the transmit power is sufficiently high to produce harmonic components in nonlinear tissue media. Postbeamforming filtering can be used to isolate specific harmonic components and/or enhance axial resolution if the SNR of the system is sufficiently high. Algorithms for postbeamforming filterbank image reconstruction for pulse-echo ultrasound can be found in [11]. For the purposes of this paper, the filter bank is formed of bandpass filters with center frequencies at a set of preselected harmonics (or subharmonics).

2.4. Nonlinear Compounding

Ultrasound propagation in tissue media is inherently nonlinear. RF echo signals obtained using modern scanners with wideband transducers carry harmonic components that are

generated by the medium nonlinearity, i.e., they are not part of the originally transmitted imaging pulses. Since the tissue nonlinearity parameter exhibits higher contrast between various tissue compared to tissue reflectivity, imaging this parameter can lead to higher contrast images of soft tissue. For a variety of physical reasons, it is well known that thermal lesions generate higher harmonics at levels higher than normal tissues. By careful design of the transmit/receive beamforming and the post beamforming reconstructions filters, high contrast images of lesions can be formed from ultrasound images formed at the fundamental and some of its higher harmonics. In general, an optimal compounding rule must be derived based on statistical model of the imaged region and the expected lesion size/location. Furthermore, the quality of the beamforming at different harmonics or scales will be spatially heterogeneous. For example, since the array sampling function (in wavelengths) is coarser at the higher harmonics, images formed at these frequency will have high contrast along the axis of the transmit beam, but the contrast deteriorates away from the main axis. Furthermore, since the harmonics are orders of magnitudes smaller than the fundamental, compounding is performed with log-compressed images after appropriate scaling. Therefore, with reference to Figure 1, the compounding is performed in two stages:

1. The outputs of the filterbank are envelope detected, scaled, and log compressed.
2. A spatially-weighted sum of the harmonic components is performed. The weighting function is derived from the spatial contrast function (SCF) of the imaging array at the different harmonics.

Assuming that the envelope-detected, normalized and log-compressed images obtained from the filterbank are given by I_1, I_2, \dots, I_N , then the compounded image is given by:

$$I(x, y) = \sum_{i=1}^N W_i S_i(x, y) I_i(x, y) \quad (3)$$

where W_i is a weighting function reflecting the relative energy at the harmonic with respect to the fundamental at the (expected) lesion location and $S_i(x, y)$ is the SCF associated with the i th harmonic. The SCFs at the different harmonic components are computed from the inverse of the beam patterns when the transmit beam is focused at the center of the (expected) lesion.

3. RESULTS

Images shown in Figure 3 and Figure 4 demonstrate the basic ideas behind the proposed image compounding algorithm. The figures show images obtained before and after

lesion formation in an *ex-vivo* liver tissue samples. The expected lesions are cigar-shaped with length of 10 mm and width of 2 - 3 mm. All images are shown at 25 dB dynamic range and have the same axial and lateral extent. In both experiments, the lesion was formed at the geometric center of the array and was expected between 90 and 100 mm in the axial direction. All images show the front surface of the sample at 80 mm and the sponge backing phantom at 120 mm. For each experiment, two pairs of images are shown, one before and one after the lesion formation. Images shown on the left hand side of each figure show the target before lesion formation while images on the right hand side show the target after lesion formation. The images on top of each figure are formed at the fundamental (1 MHz 50% bandwidth) while those at the bottom of each figure are formed at the 2nd harmonic (2MHz 40% bandwidth). Each pair of images is displayed on a log scale and normalized such that the 0 dB corresponds to the maximum of the image on the RHS, i.e., the image of the target after lesion formation. The first experiment represent a fairly homo-

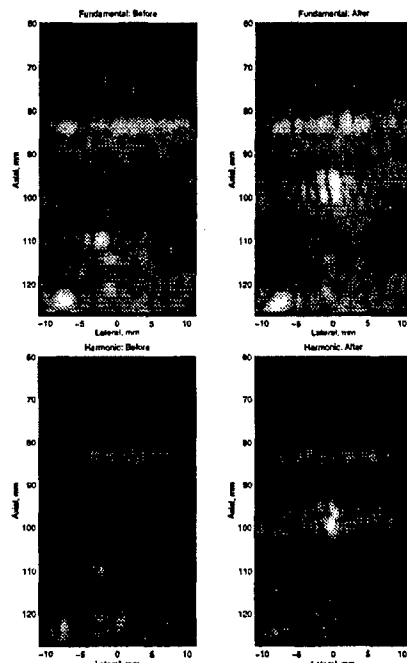


Fig. 3. Images before and after formation of Lesion 1.

geneous target tissue while the second has a pair of blood vessels at the target location as can be seen from the images taken before lesion formation. While both the fundamental and harmonic images show enhanced lesion contrast in both cases, the harmonic images show a net increase in contrast by 22 dB in the second case. On the other hand, the

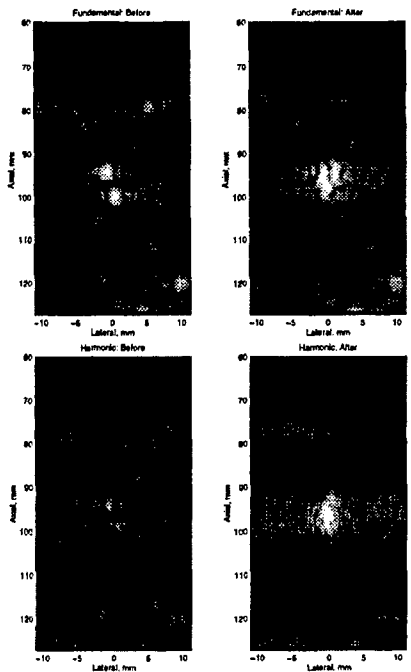


Fig. 4. Images before and after lesion 2.

net increase in contrast at the fundamental is about 7 dB. In addition, the spatial definition of the lesion in the harmonic images is superior to the fundamental. The two cases shown also illustrate the need for nonlinear compounding with a spatial weighting function as implied by (3). While the harmonic images are superior both in terms of definition and contrast near the main axis of the transmit beam, the fundamental images better represent the tissue state off-axis.

4. CONCLUSIONS

We have shown that post beamforming filterbank reconstruction of ultrasound images at selected frequencies sensitive to harmonic generation in nonlinear media produces images appropriate for compounding. The main features (thermal lesions) are sufficiently correlated while the speckle noise is largely uncorrelated. The enhanced nonlinear tissue response at the lesion location is most probably due to formation of microbubbles that resonate nonlinearly producing 2nd and higher harmonic frequencies in the echo data. Experimental work for validation of this hypothesis is currently underway.

5. REFERENCES

- [1] B. Fallone, P. Moran, and E. Podgorsak, "Noninvasive thermometry with a clinical X-ray scanner," *Med. Phys.*, vol. 9, no. 5, pp. 715-721, 1982.
- [2] D. Parker, "Applications of NMR imaging in hyperthermia: An evaluation of the potential for localized tissue heating and noninvasive temperature monitoring," *IEEE Trans. Biomed. Eng.*, vol. 31, no. 1, pp. 161-167, 1984.
- [3] J. Poorter, C. Wagter, Y. Deene, C. Thomsen, F. Stahlberg, and E. Achten, "Noninvasive MRI thermometry with the proton resonance frequency (PRF) method: In vivo results in human muscle," *Magn. Reson. Med.*, vol. 33, pp. 74-81, 1995.
- [4] N. Sanghvi *et al.*, "Noninvasive surgery of prostate tissue by high-intensity focused ultrasound," *IEEE Trans. UFFC*, vol. 43, no. 6, pp. 1099-1110, Nov. 1996.
- [5] J. Jenne, M. Bahner, J. Spoo, P. Huber, R. Rastert, I. Simiantonakis, W. Lorenz, and J. Debus, "CT on-line monitoring of HIFU therapy," *IEEE Ultrason. Symp.*, 1997.
- [6] K. Paulsen, M. Moskowitz, T. Ryan, S. Mitchell, and P. Hoopes, "Initial *in vivo* experience with EIT as a thermal estimator during hyperthermia," *Int. J. Hyperthermia*, vol. 12, no. 5, pp. 573-591, Sept. 1996.
- [7] P. Meaney, K. Paulsen, A. Hartov, and R. Crane, "Microwave imaging for tissue assessment: Initial evaluation in multitarget tissue-equivalent phantoms," *IEEE Trans. Biomed. Eng.*, vol. 43, no. 9, pp. 878-890, Sept. 1996.
- [8] E. Ebbini, P. VanBaren, and C. Simon, "Image-guided noninvasive surgery with ultrasound phased arrays," *SPIE Bios: Surgical Applications of Energy*, 1998.
- [9] C. Simon, J. Shen, T. Hall, and E. Ebbini, "Combined ultrasound image guidance and therapy using a therapeutic phased array," *SPIE: Medical Imaging 1998*, vol. 3341, pp. San Diego, Feb. 1998.
- [10] K. Thomenius, "Evolution of ultrasound beamformers," *IEEE Ultrason. Symp.*, pp. 1615-1622, Nov. 1996.
- [11] J. Shen and E. S. Ebbini, "Filter-based coded-excitation system for high speed ultrasonic". *IEEE Trans. Medical Imaging*, 45(6), December 1998.

DUAL-MODE ULTRASOUND PHASED ARRAYS FOR NONINVASIVE SURGERY: POST-BEAMFORMING IMAGE COMPOUNDING ALGORITHMS FOR ENHANCED VISUALIZATION OF THERMAL LESIONS

Charles Steidl, Hui Yao, Pornchai Phukpattaranont and Emad S. Ebbini

Department of Electrical and Computer Engineering
University of Minnesota
Minneapolis, MN 55455

Abstract- A post-beamforming nonlinear compounding algorithm for ultrasonic imaging is presented. Fundamental and harmonic image components from beamformed radio frequency (RF) data are extracted, envelope detected and compounded using a spatial compounding functions (SCFs) derived from the transmit/receive beamforming topology used in obtaining the RF data. This is specially useful for applications where single-transmit focus (STF) imaging is used. In this paper, we present results from STF imaging experiments using a novel dual-mode phased array system for image-guided surgery. In particular, we address the enhancement of the echogenicity of thermal lesions formed in *ex vivo* tissue. It is shown that new nonlinear image compounding algorithm produces 25 - 30 dB enhancement in lesion echogenicity without loss in spatial resolution. This is to be compared with a typical enhancement of 5 dB achieved by standard echographic imaging and 20 dB achieved by second harmonic imaging alone. In addition, images resulting from the new algorithm are virtually free of beamforming artifacts that can severely degrade the performance of 2nd harmonic imaging.

1. INTRODUCTION

Image guidance has long been recognized as the "enabling technology" for noninvasive thermal surgery. Highly refined energy application devices have been developed and for years. However, without reliable imaging techniques for visualization of thermal lesions, noninvasive thermal surgery has failed to find widespread acceptance in the clinic. Recently, image guidance methods based on well established imaging modalities like MRI[3], CT[5], or ultrasound [4, 8] have been proposed. Other imaging modalities are also being developed and may become available in the foreseeable future[6, 7].

An area unique to ultrasound that could revolutionize the field of image-guided surgery is the development of a new generation of dual-mode high-power phased array sys-

tems capable of both imaging and therapy [8, 9]. These piezocomposite transducers can produce focal intensity levels needed for ablative and coagulative thermal surgery with high precision. Furthermore, the operating bandwidth of such transducers allows for imaging the treatment region with adequate image quality to delineate important landmarks within and around the target volume. With these capabilities, it is possible to operate these arrays in a "self-registration" mode whereby the imaging capabilities of the array are utilized in characterization of the tissue response precisely at the expected lesion location. This is due to the fact that the beamforming is common to both the imaging and therapy modes. The main challenge to this approach is the low-contrast nature of speckle-ridden ultrasound images. This paper addresses a new post beamforming filter bank image reconstruction algorithm with nonlinear spatially weighted compounding algorithm to mitigate this problem. The design of this algorithm is motivated by the nonlinear nature of ultrasound propagation in tissue and the fact that thermal lesions are known to have increased level of harmonic generation. Experimental results demonstrate the potential of the new algorithm in both enhancing the lesion contrast and size/shape analysis.

2. IMAGE FORMATION MODEL

Figure 1 summarizes the image acquisition and image formation model. A 64-element array optimized for maximum energy delivery at 1 MHz operating frequency is used for lesion formation in sample tissue. Lesions are formed by focusing the array at a point within the target and maintaining high-power output for time intervals on the order of seconds (1 - 5 seconds typical). The power is interrupted for short intervals (milliseconds) to acquire image data by transmitting short (μ s) pulses from all 64-elements and receiving on selected elements using a matrix switch. Once the image data set is collected, RF beamforming is performed to form standard echographic images of the target region.

Funded by Grant DAMD 17-01-1-330 from the US Army Medical Research and Materiel Command.

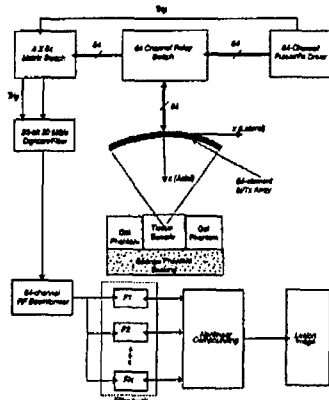


Fig. 1. Image Acquisition and Image Reconstruction Algorithm

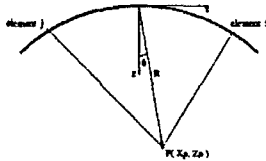


Fig. 2. Coordinate system used in the synthetic aperture imaging system.

2.1. Synthetic aperture imaging

Images are obtained using a full synthetic aperture technique [10]. The image pixel at coordinates (x_p, z_p) is therefore computed by (Fig. 2):

$$I(x_p, z_p) = \sum_{i=1}^{64} \sum_{j=1}^{64} A_i \cdot B_j \cdot s_{i,j} [(R_{ip} + R_{jp}) / c], \quad (1)$$

where i is the transmit element index, j is the receive element index, A_i is the transmit apodization weight at element i , B_j is the receive apodization weight at element j , R_{ip} and R_{jp} are the distances from the transmit and receive elements, respectively, from the image pixel, c is the speed of sound in the medium being imaged, and $s_{i,j}(t)$ is the echo acquired when transmitting with element i and receiving with element j .

2.2. Single-Transmit Focus (STF) Imaging

The synthetic aperture imaging algorithm described above can be used to produce the highest quality conventional images that can be expected from a given array. However, due to the fact that transmit beams are synthesized by superposition of single-element transmit patterns, the nonlinear interactions of the real-time transmit beams cannot be accounted for using this imaging algorithm. Therefore, we

have modified our 64-channel phased array driver to allow for pulsed transmission on all 64 channels simultaneously. This allowed us to use the full power of the transmit beams and, therefore, observe their nonlinear interactions with the tissue media. The image formation process due to a STF beam is a modified version of Equation (1) as follows:

$$I(x_p, z_p) = \sum_{j=1}^{64} B_j \cdot s_j [(R_0 + R_{jp}) / c], \quad (2)$$

where $s_j(t)$ is the received waveform at element j due to the transmitted beam and R_0 is a fixed distance determined by the focal depth of the transmit beam. All other quantities in Equation (2) are the same as their counterparts in Equation (1). It should be noted that beamforming is performed in the RF domain using true delays, i.e., no baseband conversion is done. This retains all the frequency components in the beamformed data for postbeamforming filtering operations described below.

2.3. Post Beamforming Filtering

Since beamforming is performed in the RF domain, all the frequency components in the received echo signals are retained. This is important since the echo signals can be expected to contain a mix of harmonics (and possibly subharmonics) depending on the nonlinearity of the tissue medium being imaged. This is especially true for the STF imaging mode where the transmit power is sufficiently high to produce harmonic components in nonlinear tissue media. Post-beamforming filtering can be used to isolate specific harmonic components and/or enhance axial resolution if the SNR of the system is sufficiently high. Algorithms for post-beamforming filterbank image reconstruction for pulse-echo ultrasound can be found in [11]. For the purposes of this paper, the filter bank is formed of bandpass filters with center frequencies at a set of preselected harmonics (or subharmonics).

2.4. Nonlinear Compounding

Ultrasound propagation in tissue media is inherently nonlinear. RF echo signals obtained using modern scanners with wideband transducers carry harmonic components that are generated by the medium nonlinearity, i.e., they are not part of the originally transmitted imaging pulses. Since the tissue nonlinearity parameter exhibits higher contrast between various tissue compared to tissue reflectivity, imaging this parameter can lead to higher contrast images of soft tissue. For a variety of physical reasons, it is well known that thermal lesions generate higher harmonics at levels higher than normal tissues. By careful design of the transmit/receive beamforming and the post beamforming reconstructions filters, high contrast images of lesions can be formed from ultrasound images formed at the fundamental and some of

its higher harmonics. In general, an optimal compounding rule must be derived based on statistical model of the imaged region and the expected lesion size/location. Furthermore, the quality of the beamforming at different harmonics or scales will be spatially heterogeneous. For example, since the array sampling function (in wavelengths) is coarser at the higher harmonics, images formed at these frequency will have high contrast along the axis of the transmit beam, but the contrast deteriorates quickly away from the main axis. Furthermore, since the harmonics are orders of magnitudes smaller than the fundamental, compounding is performed with log-compressed images after appropriate scaling. Therefore, with reference to Figure 1, the compounding is performed in two stages:

1. The outputs of the filterbank are envelope detected, scaled, and log compressed. The scaling of the individual harmonics can be derived from, for example, the specificity or contrast-to-tissue ratio (CTR):

$$CTR = 10 \log_{10} \left(\frac{\|y_{C_i}\|_2^2}{\|y_{T_i}\|_2^2} \right) \quad (3)$$

where $\|y_{C_i}\|_2$ and $\|y_{T_i}\|_2$ are the l_2 norms of the i th harmonic components from the contrast and normal tissue regions, respectively. These regions are easily identified under various imaging conditions. For instance, for the application described in this paper, the contrast region is the expected location of the thermal lesion (often visible on the standard echographic image).

2. A spatially-weighted sum of the harmonic components is performed. The weighting function is derived from the spatial contrast function (SCF) of the imaging array at the different harmonics.

Assuming that the envelope-detected, normalized and log-compressed images obtained from the filterbank are given by I_1, I_2, \dots, I_N , then the compounded image is given by:

$$I(x, y) = \sum_{i=1}^N W_i S_i(x, y) I_i(x, y) \quad (4)$$

where W_i is a weighting function reflecting the relative energy at the harmonic with respect to the fundamental at the (expected) lesion location and $S_i(x, y)$ is the SCF associated with the i th harmonic. This can be obtained based on simulations of pulsed or CW calculations of the following ratio:

$$S_i(x, y) = \frac{\int_{ML} B_{r_i}(x, y; x') B_t(x, y_0; x') dx'}{\int_{SL} B_{r_i}(x, y; x') B_t(x, y_0; x') dx'}, \quad (5)$$

where the subscripts SL and ML refer to sidelobe and mainlobe, respectively, and $B_{r_i}(x, y; x')$ is the i th harmonic (dynamic) receive focus at (x, y) and $B_t(x, y_0; x')$ is the transmit focus pattern (at the fundamental). Note that the SCF

is a measure of the quality of the transmit/receive pattern at the i th harmonic. The higher the SCF the more confidence we have in the received data at the i th harmonic.

3. RESULTS

Figure 3 gives a typical result of a visualization experiment using the dual-mode array and the image compounding algorithm described above. The figure shows images obtained before and after lesion formation in an *ex-vivo* liver tissue samples. The expected lesions are cigar-shaped with length of 10 mm and width of 2 - 3 mm. All images are shown at 40 dB dynamic range and have the same axial and lateral extent. The lesion was formed at the geometric center of the array and was expected between 90 and 100 mm in the axial direction. All images show the front surface of the sample at 80 mm and the sponge backing phantom at 120 mm. Three pairs of images are shown, one before (left) and one after the lesion formation. The images on top of each figure are formed at the fundamental (1 MHz) while those at the center of each figure are formed at the 2nd harmonic (2 MHz). The pair at the bottom shows the compound image using Equation 4 and the SCFs shown in Figure 4. Each pair of images is displayed on a log scale and normalized such that the 0 dB corresponds to the maximum of the image on the RHS, i.e., the image of the target after lesion formation. While both the fundamental and harmonic images show enhanced lesion contrast, the harmonic images show a net increase in contrast by 22 dB along the direction of the transmit beam. On the other hand, the net increase in contrast at the fundamental is about 7 dB. In addition, the spatial definition of the lesion in the harmonic images is superior to the fundamental. However, while the harmonic images are superior both in terms of definition and contrast near the main axis of the transmit beam, the fundamental images better represent the tissue state off-axis. The compound images show a net increase in the lesion contrast on the order of 35 dB both axially and laterally. This result can be understood in light of a close examination of the SCRs shown in Figure 4. It is also interesting to note, however, that the compound image still shows major off-axis objects, e.g., blood vessel at axial distance of 110 mm and lateral distance of 5 mm. That is, the compounding algorithm removes the beamforming side-lobe artifacts, but not major scatterers in the vicinity of the transmit beam. This is one of the main objectives of STF imaging described in this paper.

4. CONCLUSIONS

We have shown that post beamforming filterbank reconstruction of ultrasound images at selected frequencies sensitive to harmonic generation in nonlinear media produces images appropriate for compounding. The results of applying the nonlinear compounding algorithm also demonstrate a significant increase in lesion contrast over enhancement

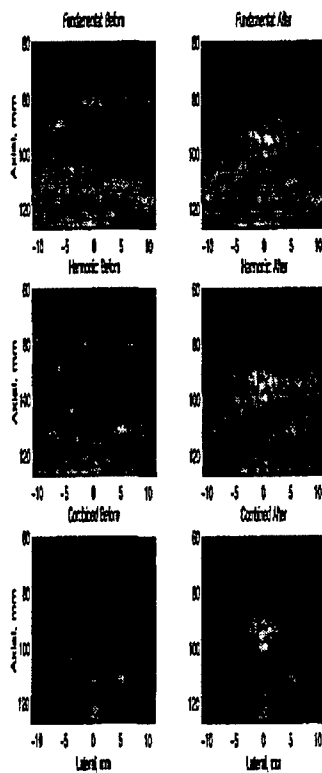


Fig. 3. Images before (left) and after lesion formation. All images are shown at 40 dB dynamic range.

achieved at either the fundamental or second harmonic. It is important to state that this contrast enhancement is achieved without loss in spatial resolution. This due to the fact that the bandpass filters used in separating the fundamental and harmonic components have wider bandwidth than the data bandwidth at these harmonics. The results shown in this paper suggest that dual-mode arrays with high contrast imaging capability suitable for real-time thermal lesion visualization are feasible. This leads to a most powerful paradigm for image guided surgery where the therapeutic and image-guidance coordinate systems are inherently registered.

5. REFERENCES

- [1] B. Fallone, P. Moran, and E. Podgorsak, 'Noninvasive thermometry with a clinical X-ray scanner,' *Med. Phys.*, vol. 9, no. 5, pp. 715-721, 1982.
- [2] D. Parker, 'Applications of NMR imaging in hyperthermia: An evaluation of the potential for localized tissue heating and noninvasive temperature monitoring,' *IEEE Trans. Biomed. Eng.*, vol. 31, no. 1, pp. 161-167, 1984.
- [3] J. Poorter, C. Wagter, Y. Deene, C. Thomsen, F. Stahlberg, and E. Achter, 'Noninvasive MRI thermometry with the proton resonance frequency (PRF) method: In vivo results in human muscle,' *Magn. Reson. Med.*, vol. 33, pp. 74-81, 1995.
- [4] N. Sanghvi *et al.*, 'Noninvasive surgery of prostate tissue by high-intensity focused ultrasound,' *IEEE Trans. UFFC*, vol. 43, no. 6, pp. 1099-1110, Nov. 1996.
- [5] J. Jenne, M. Bahner, J. Spoo, P. Huber, R. Rastert, I. Simiantonakis, W. Lorenz, and J. Debus, 'CT on-line monitoring of HIFU therapy,' *IEEE Ultrason. Symp.*, 1997.
- [6] K. Paulsen, M. Moskowitz, T. Ryan, S. Mitchell, and P. Hoopes, 'Initial *in vivo* experience with EIT as a thermal estimator during hyperthermia,' *Int. J. Hyperthermia*, vol. 12, no. 5, pp. 573-591, Sept. 1996.
- [7] P. Meaney, K. Paulsen, A. Hartov, and R. Crane, 'Microwave imaging for tissue assessment: Initial evaluation in multitar get tissue-equivalent phantoms,' *IEEE Trans. Biomed. Eng.*, vol. 43, no. 9, pp. 878-890, Sept. 1996.
- [8] E. Ebbini, P. VanBaren, and C. Simon, 'Image-guided noninvasive surgery with ultrasound phased arrays,' *SPIE Bios: Surgical Applications of Energy*, 1998.
- [9] C. Simon, J. Shen, T. Hall, and E. Ebbini, 'Combined ultrasound image guidance and therapy using a therapeutic phased array,' *SPIE: Medical Imaging 1998*, vol. 3341, pp. San Diego, Feb. 1998.
- [10] K. Thomenius, 'Evolution of ultrasound beamformers,' *IEEE Ultrason. Symp.*, pp. 1615-1622, Nov. 1996.
- [11] J. Shen and E. S. Ebbini, 'Filter-based coded-excitation system for high speed ultrasonic,' *IEEE Trans. Medical Imaging*, 45(6), December 1998.

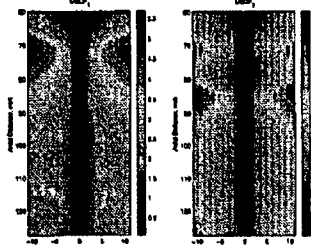


Fig. 4. Inverse of the SCRs for the fundamental (left) and the second harmonic. Transmit focus at 100 mm axial and 0 lateral.

REFOCUSING DUAL-MODE ULTRASOUND ARRAYS IN THE PRESENCE OF STRONGLY SCATTERING OBSTACLES

Hui Yao and Emad S. Ebbini

Department of Electrical and Computer Engineering
University of Minnesota, Minneapolis, MN 55455

Abstract — This paper provides a first experimental verification of what is arguably the most significant benefit of dual-mode ultrasound array (DMUA) systems for noninvasive surgery. Specifically, the use of image-based feedback for refocusing the therapeutic beam in the presence of strongly scattering objects. This capability may be critical in the use of DMUA systems for noninvasive targeting of liver tumors and noninvasive cardiac ablation. In both cases, the target is partially obstructed by the rib cage, which limits the access and distorts the geometrically-focused high-intensity focused ultrasound (HIFU) therapeutic beam. The imaging capabilities of the applicator are used in the optimization of the targeting process. The optimization procedure is based on the use of single-transmit focus (STF) imaging, in which a single transmit imaging beam employing delays derived from phasing for the therapeutic beam is used. Full dynamic receive focusing is used to form images of the target region. Taking advantage of the inherent registration between the imaging and therapeutic coordinate systems, STF images can be used in refocusing the DMUA at the target(s) while minimizing the power deposition at the rib(s) within the HIFU beam. We present experimental results of a DMUA refocusing algorithm that selects the control points from the target(s) and the ribs visible in the STF image. The new phases and amplitudes (for HIFU beam) or focusing delays (for adaptive focusing) are obtained by solving a constrained optimization problem that minimizes the direct incidence of acoustic power at the ribs as it optimizes the power delivered to the target. A 64-element 1 MHz DMUA prototype was used to refocus on a fine needle thermocouple within a tissue-mimicking phantom near the geometric focus. Four Plexiglas 1.2 cm diameter ribs were placed in front of the target (as seen from the DMUA prototype). Thermocouples were positioned on the ribs on the DMUA side in the imaging/therapy plane. The temperature at the target and the ribs were recorded before, during and after 3 s HIFU exposure for the following cases: 1) geometric focusing, 2) refocusing without considering the presence of the ribs, and 3) refocusing with accounting for the ribs. The input electrical power to the system was kept practically the same and the ratios of temperature at the target and the ribs per watt of input power were recorded. The results of these experiments show that the power delivered at the target can be increased by several fold (due to refocusing) without a corresponding increase at the rib locations. This conclusion is supported by direct thermocouple measurement at the target and rib locations. In addition, STF images before and after refocusing provide similar feedback by consistently showing increased echogenicity of the target region while the echogenicity of the ribs is not increased (often reduced)

I. INTRODUCTION

Ultrasound phased array systems are especially suitable for the generation of HIFU beams in the presence of tissue inhomogeneities and/or strong obstacles such as bones and skull. Recent results from Fink and co-workers [1] and Hynynen and co-workers [2] have shown, for example, the feasibility of generating HIFU beams through the skull with proper phase feedback. Both groups proposed refocusing based on time reversal (phase conjugation) by means of a receiving hydrophone at the focus location. They have also proposed a computational approach based on an acoustic model derived from 3D CT or MRI image of the target volume. We have also investigated the optimal synthesis of HIFU beams through the rib cage using a two-step approach to minimize the incident power on the ribs while maximizing the power delivered to the target (e.g. tumor) [3].

The introduction of piezocomposite transducer technology in the fabrication of therapeutic ultrasound phased arrays has created a new opportunity to investigate a new generation of dual-mode ultrasound array (DMUA) systems for imaging and therapy [4]. We have recently demonstrated both the therapeutic and imaging capabilities of a 64-element 1 MHz array prototype. HIFU-induced lesions in *ex vivo* tissue demonstrated a high degree of exposure control within a therapeutic operating field (*ThxOF*) extending by ± 1.5 cm around the geometric center of the array. With a 37% fractional bandwidth, it was shown that the array has an imaging field of view (*IxFov*) extending well beyond the *ThxOF* [5]. Experimental results in the visualization of HIFU-induced lesions in *ex vivo* tissue have shown that DMUA images allow for mapping of the lesion boundaries based on changes in echogenicity [6]. Have shown a far greater level of consistency than those obtained with standard diagnostic equipment, which was somewhat surprising. However, this may be attributed to two important reasons: 1) imaging with the same array allows the interrogation of the exact treatment site due to the fact that the imaging and therapeutic beams are aligned, and 2) imaging with the same frequency of the therapeutic beam is more sensitive to any resonant bubble activity that may have been generated by rectified diffusion.

In addition to the above advantage of DMUA with regards to lesion visualization, the imaging capabilities of these arrays offer another unique advantage with regards to guidance of HIFU beams. In particular, DMUA images can pro-

vide feedback for refocusing the HIFU beam taking into account any obstacles or critical structures that may be interacting with the beam. One application of this capability is refocusing in the presence of the ribs when targeting liver tumors or in noninvasive cardiac ablation. We have formulated this as an optimal synthesis of phased array beam patterns with control points at the target and the critical structures (in this case the ribs). The optimization procedure is based on the use of single-transmit focus (STF) imaging, in which a single transmit imaging beam employing the same delays as the intended therapeutic focus is used. Full dynamic receive focusing is used to form images of the target region. The resulting image is sensitive to the STF beam intensity and the strength of the scattering structure along the beam path. It is expected that the ribs will produce strong echoes as long as they are within the main beam or significant sidelobes. Therefore, they are easily identified in the STF images allowing for the estimation of the DMUA element directivity at these locations. The target point(s), on the other hand, can be located on the STF image at desired refocus location(s), i.e. no need for strong scatterer at target location. With DMUA element directivity at both target and obstacles defined from beamforming delays used to form the STF image, a constrained optimization problem maximizing the power deposition at the target while minimizing the power deposition at the ribs can be formulated. In what follows, we give a description for DMUAs image formation, constrained optimization refocusing algorithm, and experimental verification of this algorithm.

II. THEORY AND METHODS

A. Synthetic Aperture Imaging

Images were obtained using a full synthetic aperture technique [7]. This was also described in our previous publications [5]. This gives the highest quality image possible with the DMUA and allows for most accurate visualization of the treatment region.

B. Single-Transmit Imaging

We have proposed the use of this imaging mode for visualization of discrete lesion formation in previous reports [5]. However, one very important application of this mode is in surveying the target region for any critical structures interacting with the therapeutic beam. By using beamforming delays for the imaging transmit beams corresponding to the phases of the therapeutic beams, a dynamic receive image is a result of the relative strength of the beam and any scatterers within the main beam and significant sidelobes. For example, strongly scattering obstacles such as the ribs within the beam are always visible on the STF image of the DMUA. Since the beamforming (delays) for any point on the image are known, the locations of these obstacles can be used as control points in synthesizing refocused therapeutic beams

that minimize the energy at the ribs while maximizing the energy at the target.

C. Refocusing in the Presence of Obstacles

1) Refocusing Algorithm: Assume we have an N -element array with arbitrary, but known, geometry radiating into a homogeneous half space. The objective is to maximize the array intensity gain at a target point \vec{r}_T while minimize the incident power at a set of critical points, $\vec{r}_C(i), i = 1, 2, \dots, M_C$. This is an optimization problem that can be solved using Lagrange multipliers or a regularized minimum-norm least squares solution as follows [8]:

- Let the row vector $\mathbf{h}_T = [h_1(\vec{r}_T), h_2(\vec{r}_T), \dots, h_N(\vec{r}_T)]$ be the array directivity vector at \vec{r}_T (note that $h_k(\vec{r}_T)$ is the directivity of the k th element at \vec{r}_T).
- Form the matrix \mathbf{H}_C from the row vectors $\mathbf{h} = [h_1(\vec{r}_C(i)), h_2(\vec{r}_C(i)), \dots, h_N(\vec{r}_C(i))]$.
- Form the weighting matrix, $\mathbf{W}_C = [\mathbf{H}_C \mathbf{H}_C^{*t} + \gamma \mathbf{I}]^{-1}$ where \mathbf{I} is the identify matrix and γ is an appropriately chosen regularization parameter.
- The optimal complex array driving vector is given by the $\mathbf{u} = \mathbf{W}_C \mathbf{h}_T^{*t} (\mathbf{h}_T \mathbf{W}_C \mathbf{h}_T^{*t})^{-1}$.

Both the target and the critical points can be derived from images formed by the DMUA in synthetic aperture or in single-transmit focus modes. This is probably the most powerful feature of the use of the DMUA in image-guided applications.

2) Refocusing Procedure: Based on the above algorithm, the refocusing procedure is as follows:

- SA and/or STF images are formed to survey the target and any strongly scattering objects in the therapeutic beam path (or significant sidelobes).
- The elements of \mathbf{h}_T and \mathbf{H}_C are determined from the images and the optimal refocused vector is evaluated.
- The optimal steering vector is used to obtain an STF image for assessment of the refocusing result. If the refocusing is successful, then the target region should appear brighter while the critical structures should appear less bright compared to the image before refocusing.
- If STF image feedback indicates successful refocusing, the optimal steering vector is used therapeutically and the direct effects of heating are measured at the target and critical structures, e.g. temperature measurements.

III. EXPERIMENT SETUP

Figure 1 shows the image acquisition model. A 64-element concave linear phased array (100 mm radius of curvature) is used for the image acquisition. For synthetic aperture images, a single-cycle 1 MHz pulse is transmitted by each individual element and received by each of the elements to generate the RF data. Once the RF data set is

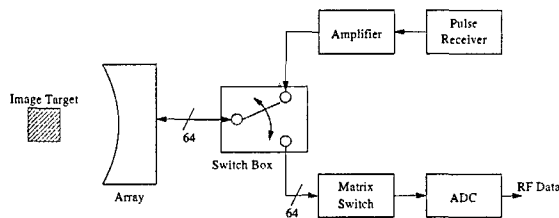


Figure 1: image experiment setup

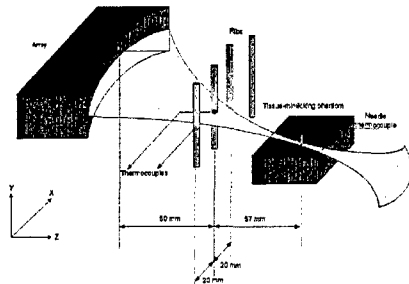


Figure 2: schematic diagram of the phantom

collected, RF beamforming is performed to form standard echographic images of the target region. For STF images, a single transmit beam for all elements is used and the echo data is received on individual elements, i.e. 64 transmissions are needed to obtain a complete STF data set.

A. Tissue-Mimicking phantom with obstacles

In order to demonstrate the feasibility of optimization of power deposition at the target(s) while minimizing the power deposition at strongly scattering obstacles, we designed the experiment setup shown in Figure 2. Four 8-mm diameter plexiglas ribs with spacing of 20 mm are used to simulate the ribcage. They are positioned about 50 mm away from the dual-mode array. A tissue-mimicking phantom [9][10] (75mm×60 mm×37mm) is positioned near the geometric focus of the DMUA (behind the ribs). A Needle thermocouple ($D=0.2$ mm) is placed near the geometric focus (not necessarily at the geometric focus). Another two wire thermocouples are fixed on the two middle ribs in the ribs cage. The three thermocouples are measured every 0.1 second by the HP 34970A data acquisition unit.

IV. RESULTS

A. Imaging: Survey, Refocusing, and Assessment

Figure 3 shows a grayscale image (50 dB) of the phantom. The image was obtained using the full synthetic aperture technique described in [5]. The result is consistent with the schematic with good spatial resolution as well as contrast. In addition to the target and the ribs, the front and back of the tissue-mimicking phantom can be easily discerned.

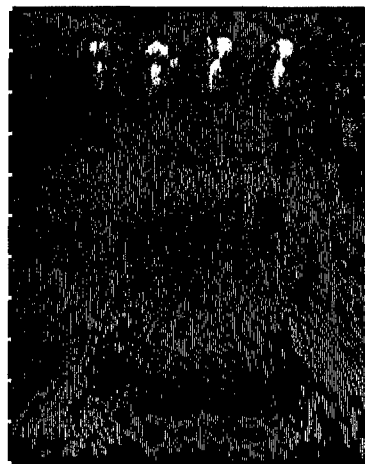


Figure 3: Grayscale image of the tissue-mimicking phantom with ribs shown in Figure 2 acquired using the DMA in synthetic aperture mode (50 dB). The white marks to left are 1 cm apart.

Even though the ribs may be outside the 50 dB I_xFOV of the DMUA, they are sufficiently strong to standout giving strong specular reflections. Furthermore, the ribs are all spatially registered correctly without distortion. The image shown in Figure 3 was used to identify the coordinates of the visible ribs as well as a target point for refocusing within the tissue-mimicking phantom. The 40 dB grayscale images shown in Figure 4 show the results of refocusing before (left) and after (right) taking the rib location into consideration. Both of these images were obtained with a transmit beam focused at the defined target location at -4 mm lateral and 103 mm axial. One can clearly see the increased visibility of the target compared to the visibility of the ribs. As shown in Figure 5, after refocusing, the echo from the target area is enhanced by 10 dB while at the rib area, the echo is reduced by 7 dB. This is due to the reduction of incident power at the ribs as predicted by the weighting algorithm described in II-C.1.

B. Direct Temperature Measurement

Figure 6 shows the temperature changes at the target and two rib locations during a 3-second exposure using therapeutic beams corresponding to the imaging beams used for generating the STF images in Figure 4, i.e. before and after refocusing. The temperature is normalized by the DC power delivered to the DMUA. Clearly, the incident power to the target is increased by a factor of 5 to 6, while the power at the rib locations is increased by a factor of two or less.

V. CONCLUSIONS

This paper presented the first experimental verification of the feasibility of using image-based feedback for refo-

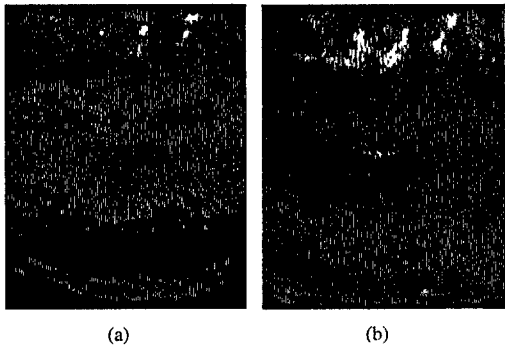


Figure 4: STF images (40 dB) using refocusing before (a) and after (b) taking the critical points and the ribs into consideration.

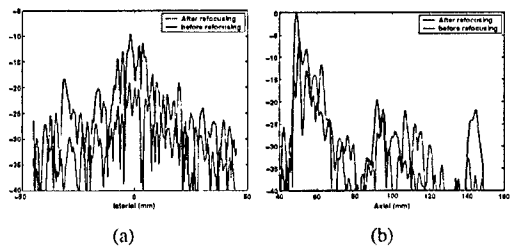


Figure 5: The magnitude change in dB in (a) lateral direction passing by the target;(b) axial direction passing by the rib.

cusing for targeting tissue structures while avoiding critical obstacles such as the ribs. This may be important if HIFU arrays are to be used for targeting, for example, liver tumors that may be partially obstructed by rib cages. This result may not be understood as a form of aberration correction since the refocusing algorithm assumes knowledge of the array directivity at the refocusing target and the critical points. Nonetheless, since these same assumptions are used in beamforming the image in the first place, the algorithm is quite robust against distortion due to inaccuracies in the speed of sound and other tissue properties. The only requirement is that at the SA or the STF image used in refo-

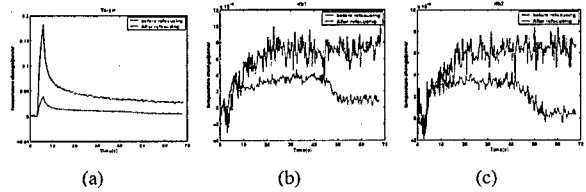


Figure 6: Temperature changes at the ribs and target location without and with the refocusing algorithm from: (a) target; (b) rib 1; (c) rib 2.

cusing provides a recognizable map of the treatment region.

ACKNOWLEDGMENTS

This work was funded by Grant DAMD17-01-1-0330 US Army Medical Research and Material Command.

VI. REFERENCES

- [1] J.-L. Thomas and M.A. Fink, "Ultrasonic beam focusing through tissue inhomogeneities with a time reversal mirror: application to transskull therapy," *Ultrasonics, Ferroelectrics and Frequency Control, IEEE transaction*, vol. 43, pp. 1122–1129, Nov. 1996.
- [2] J. Sun and K. Hynynen, "Trans-skull ultrasound therapy: the feasibility of using image-derived skull thickness information to correct the phase distortion," *Ultrasonics, Ferroelectrics and Frequency Control, IEEE transaction*, vol. 46, pp. 752–755, May 1999.
- [3] Y. Botros, E.S. Ebbini, and J.L. Volakis, "Two-step hybrid virtual array ray (var) technique for focusing through the rib cage," *Ultrasonics, Ferroelectrics and Frequency Control, IEEE transaction*, vol. 43, pp. 1122–1129, Nov. 1996.
- [4] C. Simon, P. VanBaren, and E. S. Ebbini, "two-dimensional temperature estimation using diagnostic ultrasound," *Ultrasonics, Ferroelectrics and Frequency Control, IEEE transaction*, vol. 45, pp. 989–1000, July 1998.
- [5] H. Yao and E.S.Ebbini, "Imaging with large-aperture arrays with heterogeneous directive elements," in *2003 IEEE ultrasonics symposium, 2003*, vol. 2, pp. 1243–1246.
- [6] H. Yao, P. Phukpattaranont, and E. S. Ebbini, "Enhanced lesion visualization in image-guided non-invasive surgery with ultrasound phased arrays," in *Engineering in Medicine and Biology Society,2001.Proceedings of the 23rd Annual International Conference of the IEEE, 2001*, vol. 3, pp. 2492–2495.
- [7] K. Thomenius, "Evolution of ultrasound beamformers," in *1996 IEEE ultrasonics symposium, 1996*, pp. 1615–1622.
- [8] Y. Y. Botros, E. S. Ebbini, and J. L. Volakis, "Two-step hybrid virtual array-ray (var) technique for focusing through the rib cage," *IEEE transactions on UFFC*, vol. 45, pp. 989–1000, 1998.
- [9] T. J. hall, M. Bilgen, M. F. insana, and T. A. Krouskop, "Phantom materials for elastography," *IEEE transactions on UFFC*, vol. 44, pp. 1355–1365, 1997.
- [10] K. R. Nightingale, M. L. Palmeri, R. W. Nightingale, and G. E. Trahey, "On the feasibility of remote palpation using acoustic radiation force," *J. Acoust.Soc.Am*, vol. 110, pp. 625–634, July 2001.

NONINVASIVE LOCALIZED ULTRASONIC MEASUREMENT OF TISSUE PROPERTIES

Hui Yao, Robert Griffin, and Emad S. Ebbini

Department of Electrical and Computer Engineering
University of Minnesota, Minneapolis, MN 55455

Abstract— We present *in vitro* and *in vivo* results for validation of a new localized noninvasive ultrasonic measurement of both tissue absorption and perfusion. The method employs sub-second low-intensity focused ultrasonic beams for generating brief temperature rise on the order of 1°C. The RF data from an imaging transducer is processed to produce noninvasive temperature estimate in the localized heated volume using speckle tracking or frequency-domain algorithms previously published [1] [2]. Absorption can be obtained from the initial heating rate while perfusion can be estimated from the initial decay. Due to the small size of the heated spot, the noninvasive temperature estimation can produce results that are virtually free of thermal lensing effects. Furthermore, since the measurements are based on heating and decay rates, only the parameters of the transient bioheat equation (density and heat capacity) are needed for the estimate. Both *ex-vivo* and *in vivo* results have shown two-fold to three-fold increase in tissue absorption. For the *ex vivo* results, the change in absorption was estimated using direct fine wire thermocouple measurements at the treatment site in addition to the noninvasive temperature estimation. The decay rate of the *in vivo* estimated temperature was observed to increase by two-fold indicating increased perfusion in the tumor surrounding the small lesion. While the opposite effect can be expected in volumetric lesion formation, this is very likely in this single-shot lesion formation experiment. In any event, the *in vivo* results show very clearly the feasibility of estimating perfusion based on decay rate.

I. INTRODUCTION

High intensity focused ultrasound (HIFU) is a promising modality for image-guided noninvasive surgery. MRI is currently the leading modality for guidance of HIFU due to its excellent quality and temperature sensitivity. Ultrasound guidance of HIFU is limited by the non-quantitative nature of conventional ultrasonic imaging. Several groups have recently investigated the use of elastography and viscoelastic remote palpation techniques for characterization of the state of ablated tissue (both HIFU and RF ablation) [3]. Initial reports on remote palpation are promising but true localization of the shear waves to allow a simple esti-

mation of the shear elastic modulus is yet to be demonstrated in tissue.

Two quantities believed to reflect the state of the tissue after HIFU lesion formation are tissue absorption and blood perfusion. The former has been shown to increase upon lesion formation while the latter is hypothesized to exhibit dynamics depending on the temperature rise, position within the heated volume, and degree of damage to the vasculature. The proposed new tissue property measurement is based on noninvasive tissue temperature estimation due to a short exposure (on the order of 10^{-1} s) from a focused beam to create temperature rise on the order of 1°C. This exposure is therapeutically insignificant and may fall well within the range of allowable thermal indices of standard imaging equipment. A variety of geometries for the heating source and the imaging probe can be considered. However, in this paper, we present results from a setup where the imaging plane is orthogonal to the axis of the heating transducer. The temperature estimation method used in this paper is based on the thermal dependence of the ultrasound echo that account for two different physical phenomena: local changes of sound speed due to temperature variation and thermal expansion of the propagating medium. The former generates an apparent shift in scattered location, and the latter leads to a physical shift. Along an A-line, however, the two effects lead to echo time-shift that can be estimated and have been shown to be related local change in temperature in the propagating medium. This temperature estimation approach is based on a method originally described in [1] and a later development given in [2].

II. LOCALIZED TISSUE PROPERTY ESTIMATION

The 2D temperature estimation follows the algorithm given in [2] and is summarized here to illustrate its use for the purposes of the parameter estimation algorithm (see [2] for full detail). The cumulative echo time-shift $\delta t(z, x, T_i)$ at each location and time T_i , are estimated by a correlation-based speckle tracking algo-

rithm. Axial differentiation on these estimates (along the z direction) is performed in conjunction with 2D spatial filtering along both axial (z) and the lateral (x) direction. The symbol T_i corresponds to the wall clock time, at which the i -th frame was acquired and it should be distinguished from echo time-delays t . The algorithm can be described by the following steps:

Step1 $i = 0$. Acquire 2-D RF-data $r(z, x, T_0)$, prior to any heating (baseline temperature θ_0).

Step2 $i = i + 1$. Acquire 2-D RF-data $r(z, x, T_i)$ every $\Delta T = 0.1$.

If $T_{init} \leq T_i \leq T_{end}$, Heating Beam is ON.

Step3 Estimate the incremental time-shift map

$$\delta\hat{t}_{incr}(z, x, T_i) = \hat{t}(z, x, T_i) - \hat{t}(z, x, T_{i-1})$$

at time T_i using the current and previous frames $r(z, x, T_i)$ and $r(z, x, T_{i-1})$.

Step4 Compute the cumulative time-shift map

$$\delta\hat{t}_{incr}(z, x, T_i) = \sum_{k=1}^i \delta\hat{t}_{incr}(z, x, T_k).$$

Step5 Differentiate the cumulative time-shift map $\delta\hat{\theta}(z, x, T_i)$ at time T_i (including lowpass filtering in spatial and temporal directions).

Step6 If $T_i < T_{max}$, Go to Step2.

In this algorithm, $T_{init}, T_{end}, T_{max}$, and ΔT denote start heating time, stop heating time, end of acquisition time, and frame period, respectively. Parameter estimation is performed using the transient temperature profile at the maximum spatial peak in the 2D temperature rise. The absorption is proportional to the initial heating rate while perfusion is related to the initial decay rate upon turning off the heating beam. These parameters are obtained assuming the transient bioheat equation (TBHTE) model, which is widely accepted in the hyperthermia community [4].

III. EXPERIMENT SETUP

All imaging was performed using a modified Technos MPX system from ESAOTE S.p.A., Genoa, Italy. The Technos is equipped with an RF grabber for capturing high quality beamformed RF data, which allowed the capture of up to 60 seconds of full frame data with a specified frame rate. A linear array probe (LA 522, 1-cycle transmit pulse centered at 8.5 MHz) was

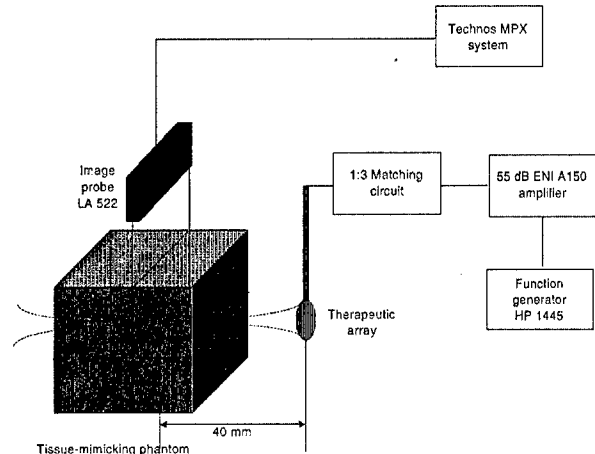


Figure 1: Experiment setup used for HIFU-induced lesion formation using a single element transducer and observation using an LA 522 linear probe monitoring along the axial direction of the lesion

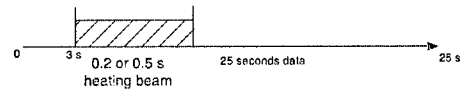


Figure 2: Experiment time schedule

used in acquiring the RF data during the heating experiments. A 4MHz transducer with 40 mm focus was used for *in vivo* for low-temperature short-duration heating experiments (Focus Surgery, Inc.). A 1.5 MHz spherical shell transducer with 63.5 mm radius of curvature was used for *ex vivo* and phantom experiments.

Each data set was 25 seconds of frame data (at 4 frame/s) from the Technos acquired as described in Section II. The first 3 seconds consisted of frames before heating with the focused transducer, i.e. $T_{max} = 25$ s and $T_{init} = 3$ s. Then the HIFU beam was turned on for 0.2 second or 0.5 second as shown in Figure 2. Note that the actual measurement time is on the order of 1 s and not the total 25 s used to collect the data.

A. Experiment Materials

Experiments were performed on tissue mimicking phantom material as described in [5][3], degassed *ex vivo* porcine liver, and one nu/nu immunodeficient mouse *in vivo*. The mouse had an MA148 human ovarian carcinoma grown in the hindleg. The elastography phantoms were fabricated from gelatin, graphite, alcohol, water and glutaraldehyde as described in the cita-

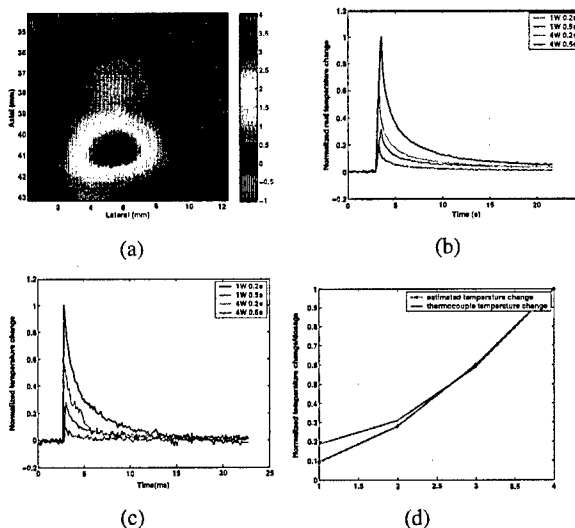


Figure 3: (a) 2-D estimated temperature change immediately after turning off the focused transducer; Normalized temperature changes of tissue-mimicking phantom under different exposure conditions from thermocouple (b) and temperature estimation algorithm (c). (d) Comparison of initial heating rate from noninvasive temperature estimation with thermocouple measurements. The maximum temperature change is 4.2 °C and the minimum temperature change is 0.75 °C.

tions.

IV. RESULTS

A. Tissue-mimicking Phantom

Figure 3 shows the measured temperature changes collected from a needle thermocouple ($D=0.2$ mm) near the transducer focus location and the noninvasive temperature estimation results at the focus location from the ultrasound echoes. The estimated temperature profiles have similar transients as the thermocouple measurements. The results clearly show excellent agreement between the estimated and measured results in terms of the initial heating rate and decay rate. Figure 3 (d) shows that 1°C change for less than 0.5 s can be tracked very well using the noninvasive temperature estimation technique.

To further quantify the agreement between the estimated and measured temperatures, we estimate the initial decay rate immediately after powering off the heating transducer (within 1 s of power off). Table I shows

TABLE I
INITIAL DECAY RATE

Exposure	Noninv. Est.	Thermocouple
1W 0.2s	-0.169	-0.116
1W 0.5s	-0.111	-0.115
4W 0.2s	-0.099	-0.105
4W 0.5s	-0.084	-0.103

the initial decay rate for the various curves shown in Figure 3 (b) and (c). The results from the two sets of curves are consistent, except for the lowest exposure level resulting in 0.75° temperature rise. This is also consistent with Figure 3(d), which allows the same conclusion.

B. In-vitro Experiment Result

Figure 4 shows the measured temperature changes collected from a needle thermocouple near the transducer focus location and the temperature estimation results at the focus location from the ultrasound echoes gotten from a degassed *ex vivo* porcine liver. Initial heating rates from the estimated and direct measurements are in good agreement before and after lesion formation. An increase in the initial heating rate at the lesion location by a factor of 2.5 is observed here.

C. In-vivo Experiment Result

Figure 5 shows the estimated transient temperature profiles at the focus location before and after HIFU lesion formation in MA148 human ovarian carcinoma in the hindleg of the nu/nu immunodeficient mouse. Comparison between the profiles before and after lesion formation indicates that a factor of 2.5 increase in the initial heating rate has been achieved in this case too. In addition, it appears that the decay rate after lesion formation has increased. While this is the result of only one experiment, it may be due to an increase in perfusion in the vasculature surrounding the small single-shot lesion that was formed in this case. This is the subject of an ongoing research in our laboratory.

V. CONCLUSIONS

The experimental results shown in this paper demonstrate the feasibility of reliable estimation of the initial heating rate at a localized heating spot for short-duration small temperature changes on the order of 1° in tissue media, including *in vivo*. Furthermore, the initial decay rates can be reliably measured in phantoms

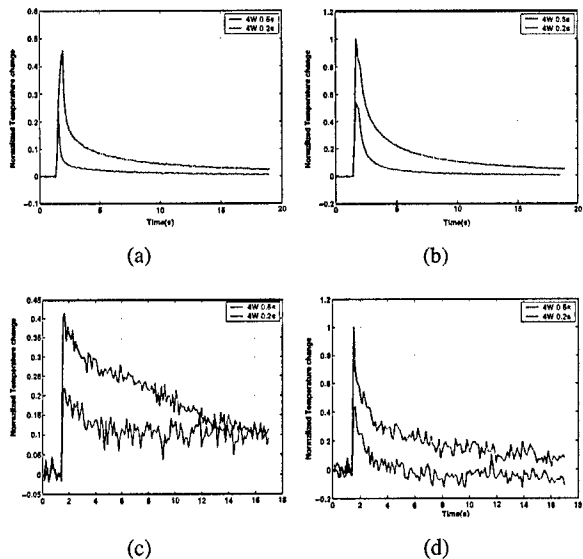


Figure 4: Normalized temperature changes of pig liver under different conditions from: (a) thermocouple before lesion formation; (b) thermocouple after lesion formation; (c) estimated results before lesion formation; (d) estimated results after lesion formation. The maximum temperature change is 1.2°C and the minimum temperature change is 0.2°C .

as well as tissue media for the same type of low exposure heating. Ongoing research at our laboratory investigates the feasibility of measuring local tissue perfusion from the initial decay rate of the localized tissue heating. The 2D temperature estimation results indicate that the spatial resolution of such measurements is determined by the heating source and the imaging system. For the configuration used for this paper, 2 mm axial resolution is possible (see Figure 3(a)).

ACKNOWLEDGMENTS

This work was funded by Grant DAMD17-01-1-0330 US Army Medical Research and Materiel Command. We also would like to thank Focus Surgery, Inc for providing the 4 MHz therapeutic transducer used in low-power heating experiments.

VI. REFERENCES

- [1] R. Seip, *Feedback for Ultrasound Thermotherapy*, Ph.D. thesis, University of Michigan, 1996.
- [2] C. Simon, P. VanBaren, and E. S. Ebbini, "Two-dimensional temperature estimation using diagnos-

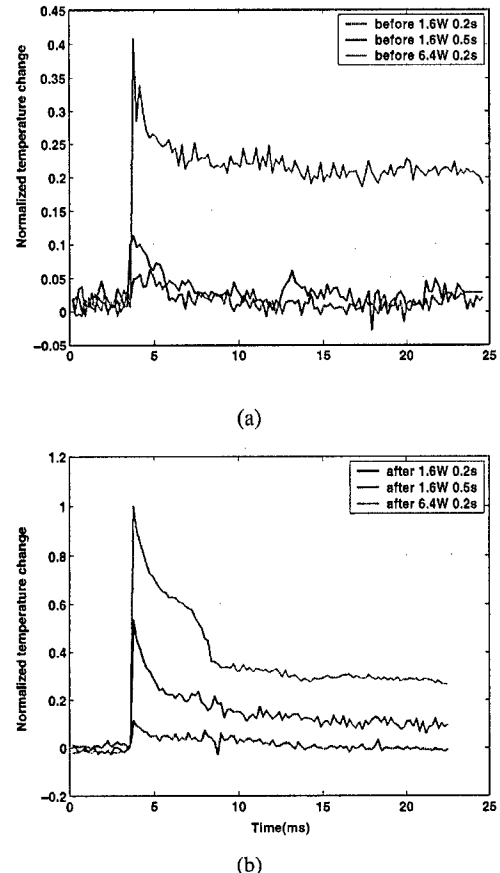


Figure 5: Normalized temperature changes of MA148 human ovarian carcinoma area of the nu/nu immunodeficient mouse under different conditions from: (a) before lesion formation; (b) after lesion formation.

tic ultrasound," *Ultrasonics, Ferroelectrics and Frequency Control, IEEE transaction*, vol. 45, pp. 989–1000, July 1998.

- [3] K. R. Nightingale, M. L. Palmeri, R. W. Nightingale, and G. E. Trahey, "On the feasibility of remote palpation using acoustic radiation force," *J. Acoust.Soc.Am*, vol. 110, pp. 625–634, July 2001.
- [4] E. Ebbini, *Deep Localized Hyperthermia with Ultrasound Phased Arrays Using the Pseudoinverse Pattern*, Ph.D. thesis, University of Illinois, 1990.
- [5] T. J. Hall, M. Bilgen, M. F. Insana, and T. A. Krouskop, "Phantom materials for elastography," *IEEE transactions on UFFC*, vol. 44, pp. 1355–1365, 1997.

REAL-TIME MONITORING OF THE TRANSIENTS OF HIFU-INDUCED LESIONS

Hui Yao and Emad S. Ebbini

Department of Electrical and Computer Engineering
University of Minnesota, Minneapolis, MN 55455

Abstract — RF data from standard B-mode and pulse inversion (PI) imaging of HIFU lesion formation of freshly excised tissue was collected before, during, and after lesion formation experiments in *ex vivo* tissue. Exposures at intensity levels of 1100 W/cm^2 to 2500 W/cm^2 for durations of 2, 3, and 5 seconds in a single shot were used. Also continuous raster scan of longer duration (10 - 20 seconds) to form slice or volumetric lesions were monitored. Monitoring was done with a diagnostic scanner and RF data was acquired at 1 frame/second for 60 seconds starting 5 seconds before each shot. Lesion maps from grayscale B-mode and PI images were obtained using level-set methods for each frame and compared with the actual lesion found by inspection. Lesion maps from PI imaging were consistently smaller in size and more in line with the actual lesion size. Transient analysis of harmonic content of lesion echoes show sustained harmonic activity for 10 - 15 seconds after the therapy pulse is turned off (in *ex vivo* liver tissue). A gradual drop in this activity follows with steady state reached within 50 - 60 seconds. It was also shown that the use of short microsecond pulses from the therapy transducer to expose the lesion location during real-time imaging significantly increased the scattering from lesion location.

I. INTRODUCTION

Ultrasound is currently a leading imaging modalities for guidance of numerous interventional procedures. This is due to advantages in cost, portability, ease of integration, and real-time implementation. However, its compromised contrast resolution and poorly understood HIFU lesion dynamics present major obstacles to the goal of mapping these lesions with conventional ultrasound. Over the last few years, several research groups suggested the use of more quantitative techniques such as elastography and remote palpation for mapping HIFU lesions. The successful implementation of these methods relies on better understanding of the transients of the echoes from the HIFU lesion location.

Motivated by P. P. Lele in [1], we hypothesized that this change in echogenicity is due to stable microbubbles that can occur even at low insonation levels. Lele found that subharmonic emission due to microbubbles showed a monotonic increase with intensity from 150 mW/cm^2 to 1500 W/cm^2 without a distinct threshold for emission (measurement done *in vitro* and *in vivo* at 2.7 and 1.8 MHz). The

consistency of the increase in echogenicity at the lesion may be explained by the fact that the microbubbles may already be resonant at the imaging frequency (same as the therapeutic HIFU beam).

II. THEORY AND MATHEMATICAL MODELS

A. Level set theory

Reference [2] gives a multi phase level set framework for image segmentation using the Mumford and Shah model for piecewise constant and piecewise smooth optimal approximation. This level set method is especially suitable for HIFU-induced lesion size estimation due to their irregular shape.

Given an observed image u_0 , to find a decomposition Ω_i of Ω and an optimal piecewise smooth approximation u of u_0 such that u varies smoothly inside Ω_i and discontinuously across the boundaries of Ω_i is called the segmentation problem in computer vision [3].

Given u_0 , find (u, C) to minimize

$$\inf_{u,C} \{E^{MS}(u, C)\} \quad (1)$$

where,

$$E^{MS}(u, C) = \int_{\Omega} (u - u_0)^2 dx dy + \mu \int_{\Omega \setminus C} |\nabla u|^2 dx dy + \nu |C| \quad (2)$$

where $\mu, \nu > 0$ are fixed parameters.

A reduced case of the above model is called *minimal partition problem*:

$$E^{MS}(u, C) = \sum_i \int_{\Omega_i} (u - u_0)^2 dx dy + \nu |C| \quad (3)$$

In the piecewise-constant case, two level set functions produce four phases (classes) as shown in Figure 1.

III. EXPERIMENT SETUP

Figure 2 shows a basic experiment setup for the formation of HIFU-induced lesions in freshly excised and degassed porcine livers samples. Experiments were performed with a modified Technos MPX system (ESAOTE SPA, Genoa, Italy) and a therapy transducer (Piezo Technologies, Etalon, Indianapolis, IN). The Technos system was modified to allow imaging in pulse inversion mode in addition to normal

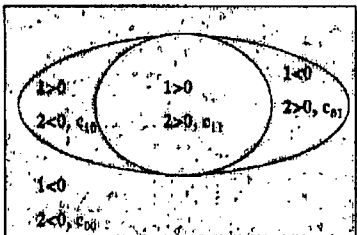


Figure 1: Illustration of two level set functions.

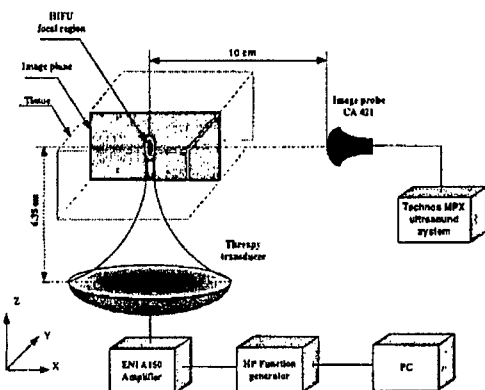


Figure 2: Experiment setup used for HIFU-induced lesion formation using a single element transducer and observation using CA 421 imaging probe monitoring along the axial direction of the lesion.

B-mode imaging. In addition, a hardware module for capturing high quality beamformed RF data allows us to capture and upload up to 60 seconds of full frame data with a specified frame rate. Frame and line trigger signals from the Technos system are also available for synchronizing external events with image acquisition. For this paper, image data were acquired from a CA 421 convex probe in PI mode with a 2-cycle transmit pulse centered at 1.85 MHz. The therapy transducer is a 1.5 MHz single-element spherical-shell transducer with $f_{\#} = 1$ (and focal distance of 63.5 mm.) A HP function generator 33120 A (Hewlett Packard) is connected to the therapy transducer through an ENI Model A150 RF power Amplifier as the HIFU source.

A. Single shot lesion formation

A variety of exposures conditions, before, during, and after lesion formation were tested. RF data from standard B-mode and PI imaging of HIFU lesion formation of freshly excised tissue was obtained. Exposures at intensity levels of 1100 W/cm² to 2500 W/cm² for durations of 2, 3, and 5 seconds in a single shot were used.

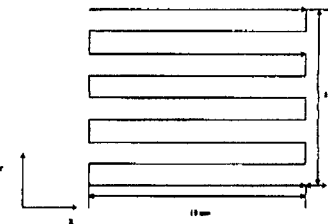


Figure 3: One programmed movement of the phantom holder to form a volumetric lesion.

B. Volumetric lesion formation

Volumetric lesions are formed by moving the tissue holder at a constant speed while the therapeutic beam is on with an intensity suitable for lesion formation. Figure 3 gives one example of a raster scan used in forming a 10 x 8 x 10 mm³ lesion. The translation speed has to be carefully set to produce the desired lesion shape (without over exposure) for a given therapeutic intensity.

C. Imaging with the therapeutic beam

Our previous work on imaging with dual-mode arrays (DMAs) *ex vivo* has shown that the echogenicity of HIFU-induced lesions is consistently higher, even minutes after the lesion has formed [4]. However, the same is not true when monitoring lesions with standard diagnostic imaging transducers. In order to gain a better understanding of this issue, we have designed a synchronized imaging mode with the modified Technos MPX scanner that can be described as follows:

1. The setup of Figure 2 is used.
2. A line trigger signal is obtained from the Technos scanner, which is running at an extremely low mechanical index (MI) in PI mode.
3. On each line trigger, the HP function generator sends a 2 cycle 1.5 MHz sinusoidal pulse with 24 μ s delay through the therapeutic transducer. The pulse from the therapeutic transducer has an extremely low MI as well (0.038 as measured by a calibrated hydrophone). The delay is computed so that scattering from the lesion location registers correctly on the Technos image.
4. The RF data is uploaded and PI images are formed. Since the imaging pulses are so small, almost perfect cancellation of the backscattering is achieved throughout the image. However, since the pulses from the therapeutic transducer have the same polarity for both the positive and negative PI pulses, they add up upon formation of the PI image. Thus, the image contains the angular scattering components from the therapeutic beam.
5. Thirty frames (1 fps) are acquired before lesion

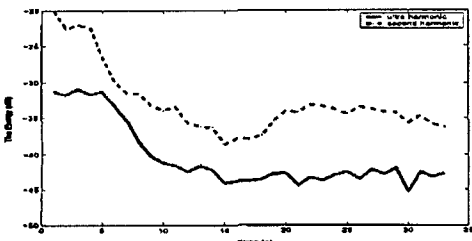


Figure 4: Second harmonic and ultra-harmonic energy as a function of time starting immediately after the therapeutic beam is turned off.

formation, 15 without and 15 with the pulse from the therapeutic beam.

6. Fifty frames (1 fps) are acquired immediately after lesion formation, 28 without and 22 with the pulse from the therapeutic beam.

This experiment is intended as an approximation of our DMA system. Here we are using the Technos to image scattering from the therapeutic beam at very low intensity and microsecond pulse duration. In the DMA approach, the same thing is done to obtain the backscatter from the therapeutic beam.

IV. RESULTS

A. Transient harmonic content of lesion

Figure 4 illustrate a typical transient analysis result of harmonic content of lesion echoes after the therapy pulse was turned off. The data is typical of an over exposure single-shot lesion (2500 W/cm² for 5 seconds.) Strong harmonic activity appears to persist for 10 - 15 s at the second harmonic ($2 f_0$) and the ultra harmonic ($1.5 f_0$) before decaying to steady state values as can be seen.

B. Lesion mapping

Lesion maps from grayscale B-mode and PI images were obtained using level-set methods for each frame and compared with the actual lesion found by inspection. Figure 5 illustrates volumetric lesion maps from grayscale B-mode and PI images obtained using level-set method. The volumetric lesion was formed by moving the phantom holder at 2 mm/s while maintaining the intensity levels at 2500 W/cm². The lesion size in B-mode images is 172.81 mm², in PI images is 111.19 mm² while the real lesion size is 83.08 mm². Lesion maps from PI imaging were consistently smaller in size and more in line with the actual lesion size. Furthermore, the transient behavior of the lesion maps was easier to observe when the contours were evaluated using the PI images. Please note that the lesion maps given here are meant to define the boundaries of the actual lesion. We simply want to identify the tissue region, as seen on an ultrasound image,

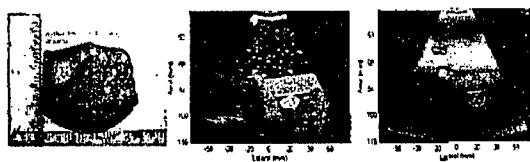


Figure 5: Cross section of a volumetric lesion in *ex vivo* porcine liver: (a) Picture; (b) Lesion map from grayscale B-mode obtained by the level-set method; (c) Lesion map from grayscale PI mode obtained by the level-set method.

that showed a change in echogenicity due to the formation of a lesion by a HIFU beam. Quantitative assessment of irreversible change of tissue due to lesion formation is not an objective of this paper.

C. Imaging with therapeutic beams

Figure 6 demonstrates the value of synchronized imaging with microsecond low MI pulses from the therapeutic transducer as described in Section III-C. The spectrograms (SPGs) show the frequency content of the received RF signal along an A-line through the lesion location. The top SPGs are computed using data in normal B-mode imaging. Figure 6(a), (b), and (c) are SPGs from frames acquired before, 1 s after, and 28 s after lesion formation. One can see a significant increase in harmonic activity after lesion formation, including sub-harmonic activity 1 s after lesion formation. The sub-harmonic component is not visible 28 second after lesion formation. Furthermore, the extent of the region where the harmonic activity occurs is also diminished 28 s after lesion formation. This is consistent with the results from Section IV-A. Figure 6 (d), (e), and (f) are SPGs obtained before, 29 s after, and 51 s after lesion formation, all synchronized with the 2 cycle 1.5 MHz pulses from the therapeutic transducer as described in Section III-C. One can see that the presence of the pulse from the therapeutic transducer before lesion formation only shows as a 1.5 MHz component at the lesion location, but no other nonlinearity is observed. On the other hand, the SPGs 29 and 51 s after lesion formation are very similar in terms of the significant harmonic activity, including sub-harmonic generation. A possible explanation of this result is that even very low MI pulses at the frequency of the therapeutic beam are capable of generating significant harmonic activity at the lesion location. It is possible that microbubbles generated by the HIFU beam still exist well after the transients have died and that even microsecond pulses at their resonance frequency are capable of producing significant increase in both linear and nonlinear scattering from the lesion location.

Figure 7 shows the energy from the lesion location before (bottom) and after (top) lesion formation. The energy is computed from received RF data as described in Section III-

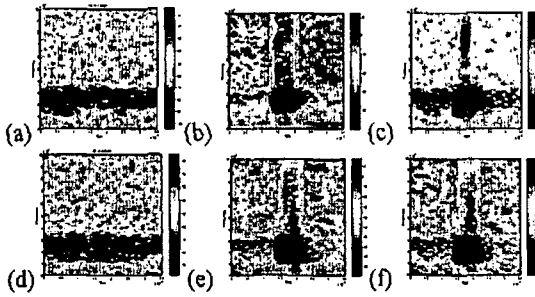


Figure 6: Spectrograms (SPGs) of the RF signal from the center line passing through the lesion. Top: w/o (a) before, (b) 1 s, and (c) 28 s after. Bottom: w/ (d) before, (e) 29 s, and (f) 51 s after.

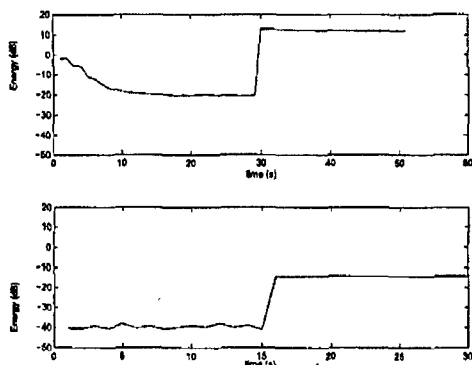


Figure 7: Total energy from the lesion location (a) after lesion formation; (b) before lesion formation. Before the lesion was formed, the therapy beam caused about 25 dB energy increase. The break in the curve corresponds to the introduction of the 2 cycle 1.5 MHz pulse from the therapeutic transducer as described in Section III-C.

C first without and later with the synchronized 2 cycle 1.5 MHz pulses from the therapeutic transducer. Without the insonation using the therapeutic transducer, the energy appears to decay after lesion formation in a similar manner to what we described in Section IV-A. However, once the insonation using the therapeutic transducer begins, a sustained increase in the energy is achieved, 33 dB above the base line in this case. Examining the behavior of the energy before lesion formation, the increase due to the therapeutic beam is only 25 dB. This indicates that the scattering from the lesion location is significantly higher after lesion formation. This is more in line with our previously reported results with the DMA and illustrates the inherent advantage of imaging HIFU induced lesions at the same frequency as the therapeutic beams.

V. CONCLUSIONS

The results presented in this paper show that the increase in echogenicity at the HIFU lesion location can be transient in nature when imaged using standard diagnostic scanners. In addition, the size of the hyperechoic region in B-mode images can vary greatly and may not be well correlated with the actual lesion size in some cases. Quantitative measurements of tissue property that may indicate irreversible tissue damage immediately upon lesion formation is not very likely based on these standard images.

On the other hand, nonlinear (e.g. pulse inversion) imaging techniques consistently provide tighter maps of lesion location on the ultrasound that is typically better correlated with tissue damage. This mode of imaging, in addition to probing the lesion site with the same therapeutic beam (at low MI) may very well provide the tools for addressing this important problem in ultrasound monitoring of HIFU-induced lesions. The results shown herein further support our working hypothesis that imaging HIFU-induced lesions with the therapeutic beam using dual-mode arrays may be a key component in the future of image-guided HIFU systems for noninvasive surgery.

ACKNOWLEDGMENTS

This work was funded by Grant DAMD17-01-1-0330 US Army Medical Research and Materiel Command.

VI. REFERENCES

- [1] M. H. Repacholi, M. Grandolfo, and A. Rindi, Eds., *Effects of ultrasound on solid mammalian tissue and tumors in vivo*, London: Plenum, 1987.
- [2] L. A. Vese and T. F. Chan, "A multiphase level set framework for image segmentation using the mumford and shah model," *International Journal of computer Vision*, vol. 50, pp. 271–293, 2002.
- [3] D. Mumford and J. Shah, "Optimal approximation by piecewise smooth functions and associated variational problems," *Comm. Pure Appl. Math.*, vol. 42, pp. 577–685, 1989.
- [4] H. Yao, P. Phukpattaranont, and E. Ebbini, "Enhanced lesion visualization in image-guided noninvasive surgery with ultrasound phased arrays," in *2001 IEEE ultrasonics symposium*, 2001, vol. 3, pp. 2492 – 2495.